Interpretation of Cometary Images and the Modeling of Cometary Dust Comae

vorgelegt von
Tra Mi Ho
von Hanoi,Vietnam

Abstract

The aim of this work was to analyze the dust coma of comet 19P/Borrelly on the basis of two data sets. In September 21, 2001 NASA's Deep Space 1 (DS1) spacecraft encountered Borrelly at a closest distance of about 2200 km away from the comet's nucleus revealing an inner dust coma dominated by dust jets and fans. In particularly a persistent dominant collimated dust stream, emanating to the sunward side was observed. The principle task was to examine these anisotropic dust emissions, whereby special attention was given to the understanding of the dynamics of the dust outflow. The release of cometary dust particles from the nucleus surface is a complex process resulting from gas sublimation dragging the grains into the circumnuclear environment. Processes such as acceleration, fragmentation and collisions play a dominant part in the first km above the nucleus. To support the data analysis and to obtain a better understanding of this scenario, a new approach has been developed to assist in the modeling of the observed dust emission.

To support the investigation of Borrelly's dust coma, images of 1P/Halley taken using the HMC (Halley Multicolour Camera) onboard Giotto have been compared with those of Borrelly.

The analysis of Borrelly's coma has been put into a broader context with ground-based observations of the comet performed at the same time of the DS1 encounter. Images of the dust coma have been acquired which give information about the dust production rate, anisotropic dust outflow and the grain size distribution. On the Earth based images, Borrelly's dust coma appears elongated with a narrow fan pointing towards the Sun. There is evidence that this peculiar shape has a direct connection with the main jet seen on MICAS. To support this conclusion, a dust coma model seen from the Earth has been developed.

Für meine Großmutter väterlicherseits
und
für meine Großeltern mütterlicherseits

Contents

Chapter 1

Introduction

For several thousand years comets have fascinated human eyes by their spectacular bright appearance. The name *comet* comes from the Greek word *kometes*, meaning *the hairy one* and in ancient history they were often regarded as heavenly omens of good or bad fortune.

Only since 1600 have they begun to lose their mystery. In the 17th century, comets began to be thought of as a natural appearance in space following orbit calculations of several people, e.g. the amateur Sir William Lower (1610) and Isaac Newton in his Principia (1687).

In 1705 Edmund Halley used Newton's new theory of gravitation to determine the orbits of a dozen well-observed comets from their recorded positions in the sky. He found that the bright comets of 1531, 1607, and 1682 had almost the same orbit, and when he accounted for the gravitational perturbation on the cometary orbits from Jupiter and Saturn, he concluded that these were different appearances of the same comet. He then used his gravitational calculations to predict the return of this comet in 1758. This comet bears since then Halley's name. Tracing back the historical record of bright comets and their positions in the sky, it was concluded that 1P/Halley had been observed periodically as far back as 240 B.C and has returned every 74 - 79 years since (Yeomans, 1991).

The era of modern cometary studies started in the middle of the 20th century with the formulation of three fundamental ideas which led to significant changes in our understanding of these objects. In 1950 Fred Whipple (Whipple 1949 & 1950) formulated his "dirty snowball" model whereby the cometary nucleus is considered to be a conglomerate of ices (e.g. H_2O, NH_3, CH_4 etc.) and meteoric materials with a single solid nucleus. In the same year a distant reservoir of comets called the Oort cloud was postulated by Jan Hendrik Oort (1950). Only one year later Ludwig Biermann (1951) explained the motions in cometary plasma tails as resulting from the interaction of a comet with the solar wind.

Comets can be generally characterized as comprising five major parts (Festou *et al.*, 1993).

The **cometary nucleus(1)** is a kilometer-sized, irregularly-shaped, solid body consisting of ices (frozen gases; mostly H_2O) with imbedded dust particles. This body moves in an elliptical, sometimes nearly parabolic or hyperbolic orbit in the Solar System. When the comet approaches the Sun, the surface is heated up causing sublimation of the ices and ejection of gas and dust.

These emissions form a cloud around the nucleus which is called the **coma(2)**. The coma is visible to an observer because of the scattered sunlight from the dust particles, atomic and molecular emissions (mainly dominated by fluorescing under excitation from solar radiation), and the thermal emission at IR wavelengths. The nucleus and the coma together are called the comet's head.

The neutral gas species in the coma can be ionized by solar UV photons and interact with the solar wind. The solar wind penetrates the envelope of hydrogen atoms and the coma. The resulting magnetic fields in the coma sweep the ions out of the coma into a long distinctive **ion tail(3)**. Because one of the most common ions, CO^+, emits strongly at blue wavelengths, the ion tail often appears blue to human eyes.

The dust particles in the coma, which are affected by solar radiation pressure, are pushed out of the coma and form a curved **dust tail(4)**. Compared to the ion tail, the dust tail is morphologically diffuse, and appears white or slightly pink (because dust grains scatter sunlight slightly better at longer wavelengths).

A third **neutral gas tail (5)** composed of sodium was discovered in 1997 (Cremonese *et al.*, 1997). This tail is also formed by radiation pressure due to resonance fluorescence of sodium atoms. Still its extent, and in particular its source, has not been clearly identified. Based on observations showing that the sodium tail is mainly superimposed on the dust tail, a strong relation between sodium and the dust emitted by the nucleus is suggested. Similar gas tails for other species (e.g. potassium) might be expected.

The size of an active nucleus is estimated to range between 1 - 10 km (Groussin, 2002). For a typical, bright, short-period comet the mass loss per apparition is estimated to be around 10^{10} to 10^{11} kg. Because of this rather high mass loss it can be concluded that the observed comets have not been in orbits so close to the Sun since the formation of the Solar System. Additionally the ice-dust composition of the nucleus points to an origin cold enough to allow existence of frozen water. Therefore the comets must originate from a reservoir at a larger distance from the Sun.

Based on van Woerkom's (1948) theory of the orbital diffusion caused by plan-

etary perturbations, J. Oort (1950) made a statistical analysis of the orbits of long period comets. He deduced the existence of a vast cloud of comets orbiting the Sun at distances of 20 000 - 100 000 AU. This cloud is thought to contain ≈ 200 million comets and bears a total mass of 1/10 - 1/100 of the Earth's mass. Through the close passage of neighboring stars, fresh comets are continually being transported from this cloud into the inner Solar System. It has still not been directly observed, but a large amount of indirect evidence seems to point to the cloud's existence.

However, in the late 1980's, it became apparent that a problem existed with the Oort cloud model. Numerical simulations of the evolution of the Oort cloud under the action of planetary perturbations were unable to reproduce the main observed characteristics of the orbit of short period comets. By trying to reproduce the observed near coplanar distribution of orbits found in the short-period comet population from an initial isotropic distribution of Oort cloud comets, problems were encountered (see Stagg and Bailey, 1989). In order to produce the observed low inclination population of short period comets, an initial population also lying close to the plane of the ecliptic is required.

Edgeworth (1943 & 1949) and Kuiper (1951) independently produced theories of the origin of the Solar System in which the material in the disk or nebula out of which the planets formed did not suddenly cease at around the distance of Neptune. However, since accumulation into planets at such distances can proceed only slowly, a swarm of smaller bodies might form but fail to reach larger sizes. In the late 1980's ground-based observing techniques reached a level to facilitate the search for bodies lying within the Edgeworth-Kuiper belt. Finally Jewitt and Luu (1992) detected for the first time, a member of this belt: 1992 QB. Since this initial discovery several hundreds of such objects have been found and the theory of a separate source of short period comets has been supported.

Our understanding of comets has been advanced by several space missions and extensive Earth-based observation campaigns. The first comet encounter was on September 11, 1985 by the International Cometary Explorer (ICE), which passed through the tail of comet 21P/Giacobini-Zinner at a distance of $\approx 8\ 000$ km from the nucleus. Several months later the biggest cometary *in situ* observation campaign took place with five spacecraft encountering 1P/Halley in March 1986. One by one the spacecraft Vega 1, Suisei, Vega 2, Sakigake and Giotto approached the comet. For the first time in history, images of the nucleus and its immediate vicinity were obtained by cameras onboard the spacecraft Giotto of the European Space Agency (ESA) and the two Russian Vega spacecrafts. The HMC (Halley Multicolour Camera) onboard the Giotto spacecraft could deliver images, showing a dark ellipsoidal nucleus and the inner dust coma (Keller *et al.*, 1986). After this successful fly-by, Giotto headed to the next cometary rendezvous. On July 10, 1992 the spacecraft flew within 200 km of Comet 26P/Grigg-Skjellerup. Un-

fortunately the camera was blind (as a result of impacts at comet Halley). Thus no images of the nucleus were obtained.

The second successful cometary encounter which could reveal the innermost of a comet was on September 22nd 2001 when NASA's spacecraft Deep Space 1 (DS1) approached the nucleus of 19P/Borrelly at a closest distance of 2174 km yielding several pictures of the nucleus and other scientific data, e.g. energy spectra taken from the PEPE (Plasma Experiment for Plasma Exploration) mass spectrometer.

The cometary close up data base was further enriched on January 2, 2004 when Stardust flew within 236 kilometers of Comet 81P/Wild 2 and captured dust particles in its aerogel collector for return on Earth in January 2006. Next to the dust sample collected, the navigation camera was also able to take images of the nucleus during a high-speed flyby.

The next close encounter of a spacecraft with a comet is scheduled in early July 2005, when the NASA Deep Impact mission will deliver a 360-kg Impactor space-craft to collide with comet 9P/Tempel 1. Finally, ESA launched its Rosetta spacecraft on March 2, 2004, on a long journey to reach Comet 67P/Churyumov-Gerasimenko in 2014. The spacecraft will drop a surface science package (Philae) on the surface and escort the comet for 18 months through perihelion.

Although many questions about comets have been answered in the past years with the support of ground-based observations, *in situ* measurements, and models, a number of open questions still exist. The atomic composition of cometary dust and gas has been determined, but not all parent molecules are known and the composition of dust materials is still not clear. The dust and gas outflow close to the surface and into its vicinity is very complex and not all models can explain the actual observational data. Cometary data sets are divided in two main parts: The Earth observation data (including the Hubble Space Telescope, HST), which have a resolution of few hundreds to $1 \cdot 10^3$ km per resolution element and the few *insitu* data sets, which reveal the dust coma up to only 100 km away from the nucleus but at resolutions of ≈ 100 m per resolution element. The dominant physical and chemical processes are strongly distance dependent.

This work deals with the comparative analysis of the Visual CCD (VISCCD) images of comet Borrelly taken with the MICAS instrument onboard Deep Space 1 and images taken with the 2m-Zeiss-Telescope at Pik Terskol (Russia) at the time of the spacecraft's encounter with the comet. The experiment and the mission will be introduced in the following chapter including a summary of the discovery history of 19P/Borrelly. As the properties of the innermost coma of comet Borrelly will be compared with those of comet Halley as observed by the Halley Multicolour Camera onboard Giotto, a short discussion of 1P/Halley is also included.

The analysis of the cometary data sets comprises the examination of the cometary dust outflow behavior, possible deviations from force-free radial outflow, and the emission characteristics. Also quantitative parameters such as the dust production rate and the optical thickness have been determined.

Chapter 5 and 6 describe models to simulate the observational data. The first model is employed to fit the MICAS data sets and thus will give a closer insight into the inner dust environment of Borrelly (the first 20 km). The second model will simulate the outer dust coma and tail. Both models allow us to derive parameters, such as the dust size distribution and the outflow velocity.
In the last section the results of the in situ measurements and the earth observation are summarized and compared with each other. This will render a more consistent and broader understanding of phenomena in the comet's dust coma.

Chapter 2

Background

This thesis deals particularly with observations of comet 19P/Borrelly in 2001 and comparison with comet 1P/Halley in 1986. The Borrelly data were obtained by the Deep Space 1 mission which encountered the comet on September 21, 2001. Simultanously a ground based observational campaign was mounted to survey the comet simultanously at Pik Terskol (Caucasus/Russia).

This chapter should give the reader a deeper insight into the background of this work. First comet 1P/Halley and its basic properties are introduced. A summary of the 1986 mission of Giotto to comet Halley is included. Afterwards follows an introduction to 19P/Borrelly and general information about the flyby of the DS1 spacecraft. An overview of Borrelly's observation campaign in the Caucasus is given. In addition the appropriate data reduction applied to the images from all data sets are described.

2.1   1P/Halley and Giotto

1P/Halley's most recent return to the inner Solar System was in 1986. Two years before, this comet was recovered by Jewitt and Danielson (1984) at a distance of 11.2 AU. Theirs and later observations suggested that the nucleus has an approximate radius $R_N = 3$ km and a corresponding geometric albedo of $p_v = 0.06$. The mass was estimated to be $\sim 10^{14}$ kg by assuming a density of 1000 kg m^{-3}.

The best images of the nucleus was finally gained on March 14, 1986 by the Halley Multicolour Camera (HMC) onboard ESA's spacecraft, Giotto. Giotto, a European Space Agency (ESA) mission, was launched on July 2, 1985 from the Centre Spatial Guyanais (CSG) in Kourou, French Guyana and reached the nucleus at a closest distance of 596 km in the night of March 13/14, 1986. The high dynamic range of HMC could reveal the full outline of the nucleus. This was not possible on the images of the Russian Vega 1 and Vega 2 spacecrafts, which flew-by some days before. The encounter parameters of Giotto with comet

Halley are listed together with Borrelly's data in Table 2.2.

The images taken by HMC revealed a rather elongated and irregular shaped nucleus with a size of 14 km × 7.5 km in projection on the sky, a very dark surface with an albedo of 4 % and highly concentrated and anisotropic activity (Keller *et al.*, 1987). The coma was found to be highly structured with jet-like structures. These features had their origin in "active" regions distributed on the nucleus. There are many papers dealing with the outflow and interaction of dust and gas on the nucleus' surface and in its vicinity (e.g. Probstein, 1969; Gombosi *et al.*, 1985; Kitamura, 1986 & 1987, or Crifo *et al.*, 1995) although a complete explanation of the observed brightness distribution has not yet been made. Additionally, Giotto provided a better understanding of the chemical composition of the dust particles from the spectrometers onboard Giotto, the Vega1 and Vega2 (Jessberger *et al.*, 1988). The results of these instruments will be introduced in the next chapter.
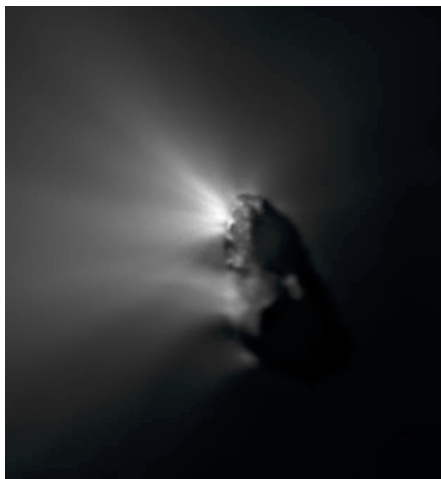
Figure 2.1: This is a composite image of the nucleus of comet Halley composed of 68 images at a resolution varying from 500 m px^{-1} to 50 m px^{-1} near the active region, taken by the HMC camera onboard Giotto in March 1986.

HMC

HMC was a high resolution Ritchey-Chretian telescope with a focal length of 1 m mounted behind the front shield of the spacecraft. Giotto rotated with a period of 4 sec. The rotation of the probe was used to raster the field of view. The maximum field of view of the camera was about 0.5° x 0.4°. The CCD detectors were split into four detector sections of 390 x 292 pixels, each one 22.4 μm square. These detectors were covered with different filters allowing HMC to provide color

information (Keller *et al.*, 1994). Images were acquired from around 700,000 km through to a distance of 2000 km from the nucleus before the experiment ceased operation as a result of impacts on the spacecraft.

These data have been fully calibrated into physical units and are available through the Planetary Data System (Keller *et al.*, 1996) and the ESA Planetary Science Archive (PSA). The images comprise a FOV ranging from $124 \cdot 10^3$ km to 600 km.

2.2   19P/Borrelly and Deep Space 1

Comet 19P/Borrelly is a Jupiter family comet discovered on December 28 1904 by Alphonse L. N. Borrelly during a routine search for comets. During January 1905 the comet was widely observed with a maximum magnitude of about 9 early in the month. The coma diameter was typically 2 arcmin, while the tail reached a length of 10 arcmin. R. G. Aitken (1905) computed an elliptical orbit later the same year which indicated an orbital period of 7.30 years. By the time observations ceased astronomers had determined that the comet passed perihelion on 1905 January 17. The perihelion distance was determined as 1.395 AU, and the orbital period was 6.91 years. Borrelly has been observed on subsequent returns into the inner Solar System with a maximum magnitude mostly ranging between 8 and 11 and a tail length around 10 arc minutes. The apparition in December 1911 was an exception when a maximum magnitude of 8.4 and a tail length of 30 arcmin were reported. The low magnitude value was the result of a relatively close approach to Earth (0.53 AU).

Orbital investigations have indicated that the comet was placed into its discovery orbit by a series of moderately close approaches to Jupiter during the 19th century (in 1817, 1853, and 1889). The comet's orbital period at discovery (6.9 years) caused it to arrive at perihelion roughly one month earlier at each succeeding apparition. This caused the discovery apparition, as well as those of 1911 and 1918 to be very favorable for Earth-based observations, while those that followed became progressively worse. The six orbital elements of comet Borrelly and Halley are summarized in Table 2.1.

Another moderately close approach to Jupiter during 1936 nudged the orbital period up to 7.0 years, which virtually locked it into a pattern of very unfavorable returns during the next few returns. Subsequently, the comet was not detected during its 1939 and 1946 apparitions. Conditions were still poor for the 1953 return, but Elizabeth Roemer (Jeffers *et al.*, 1954) managed to photograph the comet nearly 7 months after perihelion. It was then estimated to have a magnitude of 18.5. The comet experienced another moderately close approach to Jupiter during 1972 which reduced the orbital period to 6.8 years.

Parameters	19P/Borrelly	1P/Halley
Perihelion distance [AU]	1.358	0.587
Orbital eccentricity	0.624	0.967
Orbital inclination [deg]	30.325	162.24
Argument of perihelion [deg]	353.375	111.33
Long ascending node [deg]	75.425	58.42
Orbital period [a]	6.86	76.0

Table 2.1: A list of the six orbital elements for comet Borrelly (2001 epoch) and Halley (1994 epoch).

The orientation of the spin axis could be determined by Sekanina (1979) from position angles of the dust fan reported by the observers Van Biesbroek, Chofardet and Jeffers in 1911-1932 (Sekanina, 1979). These observations have been mentioned to be indicative for a "fan shape" coma, produced by a bright jet in the coma of the rotating nucleus.

The water production rate of $Q[H_2O] = (2.5 - 4.0) \cdot 10^{28}$ s^{-1} was measured at perihelion for the 1981, 1987, 1994 and 2001 apparitions (Bockelée-Morvan et $al.$ (2004); Weaver et $al.$ (2003); Schleicher et $al.$ (2003)).

A'Hearn et $al.$ (1995) published a catalogue with the ensemble properties of 85 comets which have been observed over a period of 17 years. This catalogue includes Borrelly. They gave a dust production rate in $Af\rho$ [1] value of ≈ 650 cm with a peak OH production rate of $\approx 2 \cdot 10^{28}$ molecules/s and a dust to gas ratio of $\chi = 1.16$. The dust production rates derived by Cochran and Barker (1999) and Lamy et $al.$ (1998) range between $Af\rho \sim$ (300-600) cm whereby Schleicher et $al.$ (2003) derived, for the time span of few days prior to the Deep Space 1 encounter, an $Af\rho$ value between 400-500 cm.

The comet was also scrutinized by the Hubble Space Telescope (HST) during the 1994 apparition. Lamy et $al.$ (1998) could extract from high resolution HST images light curves of the nucleus. They determined the size of Borrelly's nucleus. Assuming the nucleus to have a geometric albedo of 0.04 and its shape to be a prolate spheroid with a rotational axis pointing in the direction determined by Sekanina (1979), they derived its semi-axes to be 4.4 x 1.8 km. In addition the time coverage of the observations (about 12h) allowed a determination of the spin period (25h) assuming that only half the double-peaked lightcurve was observed.

The comet's return in 2001 was another favorable one with the prediction that the comet would attain a maximum magnitude of 10 during September. The

---

[1]The dust activity of a comet can be measured in terms of a quantity called $Af\rho$, which is albedo $\times$ filling factor x aperture radius. The definition of these values are given in Chapter 3.

comet came under widespread observation by amateur astronomers during July 2001, when the magnitude was near 13 and by the beginning of August it steadily brightened to magnitude 11. During this same period of time, the comet's coma increased from a diameter of about 1 arc minute to just over 2 arc minutes. By mid-September, observers indicated a magnitude between 9.5 and 10.5.

Figure 2.2: The nucleus of Borrelly taken by MICAS (Miniature Integrated Camera and Imaging Spectrometer) onboard DS1.

The 2001 apparition became even more noteworthy as it was only the second comet to be photographed in situ by a space probe when Deep Space 1 flew about ≈ 2200 km from the nucleus on September 22. Pictures of the nucleus revealed its dimension to be about 8 km long and about 4 km wide, in good agreement with the observations of Lamy *et al.* (1998). As the probe approached the comet, a sharply defined jet about 60 km long was detected extending toward the sun. As the probe moved closer this jet was resolved into three columns or jets, and at its closest, the probe revealed the jets were emitted from bright, smooth patches on the surface. The primary jet appears to emanate from one of the rotation poles (Boice *et al.* 2002; Soderblom *et al.* 2002). There were also indications that the jets were eroding the surface and creating basins. It was suggested that since the erosion is occurring at the pole, this might eventually cause the comet to split. Chapter 3 contains further discussion about the observed dust emission features close to the nucleus.

2.2.1 Deep Space 1

Deep Space 1 (DS1) was part of NASA's New Millennium Program. It was launched from Cape Canaveral on 24 October, 1998. Its main objective was to test its payload of twelve advanced, high-risk technologies for future missions.

Some of the advanced technologies included were *Solar Electric Propulsion, Solar Concentrator Arrays, Autonomous Navigation, Miniature Integrated Camera and Imaging Spectrometer (MICAS), and a highly integrated Ion and Electron Spectrometer (PEPE).* The MICAS experiment is of special note for this work.

After initial in-flight testing, Deep Space 1 conducted a "bonus" encounter with an asteroid. On July 28, 1999, the spacecraft flew by 9969 Braille. The closest approach distance was 26 kilometers. During the close flyby, the spacecraft took images, measured such basic physical properties of the asteroid as its mineral composition, size, shape, and brightness, and searched for changes in the solar wind as it interacted with the asteroid. But the spacecraft tracking system failed to lock onto the target and hence, the best images of the asteroid were rather poor and of low resolution. Oberst *et al.* (2001) used these data together with ground-based observations to analyze the rotation of Braille.

After Deep Space 1 completed this fly-by, the spacecraft was re-directed to Borrelly. On September 22, 2001 at 22:30 UT it approached the nucleus to a closest distance of 2174 km on the sunward side. The encounter parameters for this mission are listed in Table 2.2. During the initial phase of the encounter the viewing direction of DS1 and that of ground-based observers were roughly orthogonal to each other. This provides a powerful tool for the study of the inner coma of Borrelly. As the spacecraft range to the comet decreased within half an hour of the closest approach, the spacecraft began to turn to keep tracking the nucleus and the viewing direction changed. This manoeuvre delivered additional information about the 3D dust distribution of the coma.

Parameters	Giotto	Deep Space 1
Date	14 March 1986	22 September 2001
Time [UTC]	00:03:01.84	22:30
Distance of closest approach [km]	596	2174
Phase angle during approach [$^\circ$]	107.2	88
Relative velocity [km/s]	68.373	16.58
r [AU]	0.9023	1.36
Δ	0.960	1.47

Table 2.2: The Giotto and DS1 encounter parameters. r is the heliocentric distance and Δ is the geocentric distance of the nucleus at the given time.

2.2.2   MICAS

MICAS was a Miniature Integrated Camera and Spectrometer, conceived and developed by a team from the United States Geological Survey, the University of

Arizona, Boston University, Rockwell, SSG Inc., and the Jet Propulsion Laboratory. The 12 kg package carried two cameras, an ultraviolet imaging spectrometer, and an infrared imaging spectrometer plus all the thermal and electronic control. Traditional spacecraft have used three separate instruments to accomplish all these functions. The technological challenge was to investigate mass savings and performance from such an integrated system.
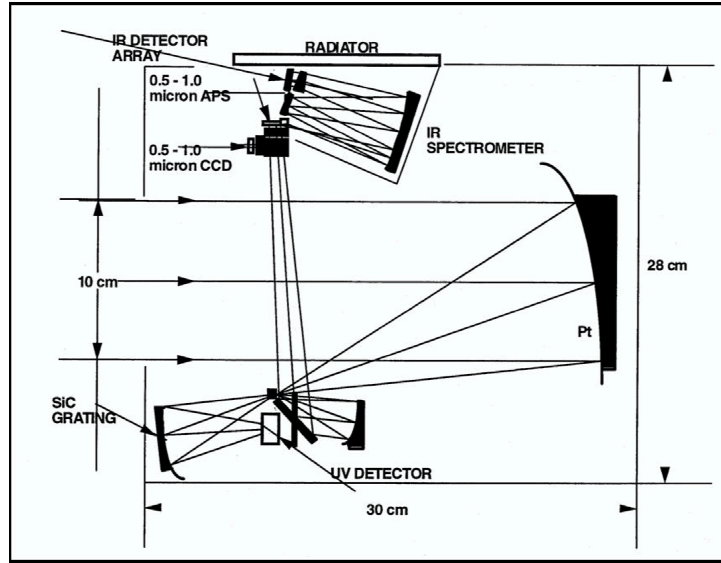
Figure 2.3: This is the schematic optical ray-trace of an off-axis Gregorian multi-wavelength telescope used in the MICAS instrument. The locations of the instruments are labeled.

Parameter	Channel			
	UV	APS	CCD	IR
Wavelength Range [nm]	80-185	500-1000	500-1000	1200-2400
Aperture Diameter	100	100	100	100
Effective Focal Length [mm]	171	677	677	752
F/number	1.7	6.8	6.8	7.5
Detector Array Size	35x164	256x256	1024x1024	245x256

Table 2.3: Parameters of the detectors of MICAS.

All the sensors of MICAS shared a single 10-cm-diameter telescope; a common off-axis Gregorian fore-optic. An optical ray-trace of the instrument is shown in Figure 2.3. With a structure and mirror of highly stable SiC, no moving parts were required; the detectors were electronically shuttered. The characteristics are summarized in Table 2.3.

	UV	APS	CCD	IR
Pixel Size [microns]	54	12	9	40
FOV [deg]	0.63x0.03	0.26x0.26	0.69x0.78	0.70x0.003
IFOV [microrad/pixel]	316	18	13	53

Table 2.4: This table contains MICAS first order optical parameters. FOV denotes the field of view of the instruments.

The first order optical parameters are shown in Table 2.4. The MICAS VISCCD (Visible-light Charge Coupled Device) camera used a 1024 x 1024 CCD with 9 μm pixels operating in a continuous frame-transfer mode. The detector array was continuously clocked at ~ 6 μsec/line, so that the transfer of the whole active imaging array required ~ 6 ms into the masked area (see Soderblom et $al.$, 2004).
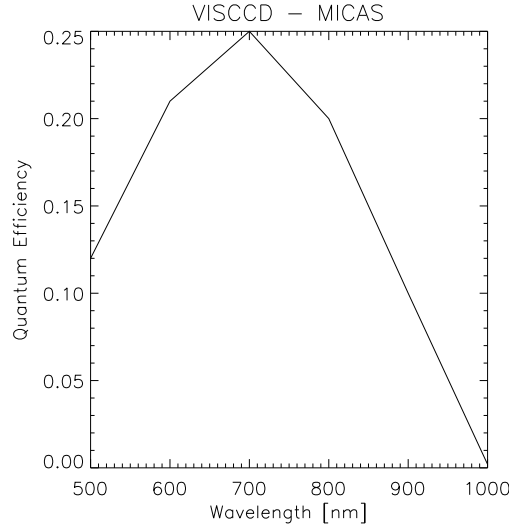
Figure 2.4: The quantum efficiency of the VISCCD.

The quantum efficiency of the VISCCD is plotted versus wavelength in Figure 2.4. The quantum efficiency of the detector reaches a maximum at 700 nm.

2.2.3   Available Data Sets

This work used the near encounter images of the Standard Level 1 data set from the United States Geological Survey taken by the MICAS VISCCD camera. The data have been absolute calibrated in reflectivity (I/F) with an accuracy of $\approx 20\%$. This value is the so called reflectivity and is defined as the ratio of the received intensity $\times \pi$ to the solar flux. For a 100 % reflecting Lambertian target viewed and illuminated normal to its surface the value of I/F is equal to 1. For this absolute radiometric calibration, the VISCCD images of Mars and Jupiter

acquired from DS1 during November 1999 were used. The full equation used to convert raw DN to I/F was:

$$
\begin{aligned}
\frac{I}{F} &= \left[0.95 \times (DN_{raw} - DC_{bias}) + 122.0 - \frac{4.63 \times 10^{-20}}{DN_{raw} - DC_{bias} + 300.0} \right] \\
&\times \ \frac{r_h^2}{2.9 \cdot 10^6 \times EXP}
\end{aligned}
\tag{2.1}
$$

where DN_{raw} is raw data number, DC_{bias} is the constant dark offset bias, r_h is the heliocentric range to the target in AU and EXP is the VISCCD exposure time in milliseconds (Soderblom *et al.* (2004)). Table B.1 in the Appendix summarizes the set of images which were relevant for the following data analysis.

Strong background noise has been observed on the "far"-images of MICAS, which could not be removed without degrading the image quality. Therefore the analysis in this work will exclude these images.

2.3   Earth-based Observations on Pik Terskol

At the encounter time of DS1 with Borrelly, the comet was observed from the observatory at Pik Terskol (Caucasus, Russia). The complete observing run was from September 19 to 27, 2001. The observations were performed with a two channel focal reducer mounted on a 2-m Zeiss Telescope. The principle of this experiment has been described first by Courtes (1960).

A focal reducer adapts the imaging elements of the detector to the characteristic size of the object or of the seeing disk. Fig. 2.5 shows the optical arrangement of the two channel focal reducer of the MPAe (Jockers *et al.*, 2000) used for the observations of Borrelly. Behind the RC (Cassegrain) focus the telescope beam is recollimated by a lens collimator. A color dividing (dichroic) mirror reflects the blue part of the spectrum and transmits the red part. Each "channel" has a camera lens forming reduced images of the Cassegrain focal plane which are then recorded by two CCD systems. Further dispersing or polarizing optical elements can be put in the parallel beam either before or after the color divider.

In this campaign the Fabry-Perot etalon was placed in front and the filters behind the color divider. The images recorded were continuum images of the dust coma with narrow (IF 444, IF 526, IF 631 and IF 642) and broad band filters (RX); interferometric images and polarization images. The chosen wavelength filters provide images of the coma which are free of cometary molecular emissions. The basic parameters of the filters and information of the optical layout are listed in
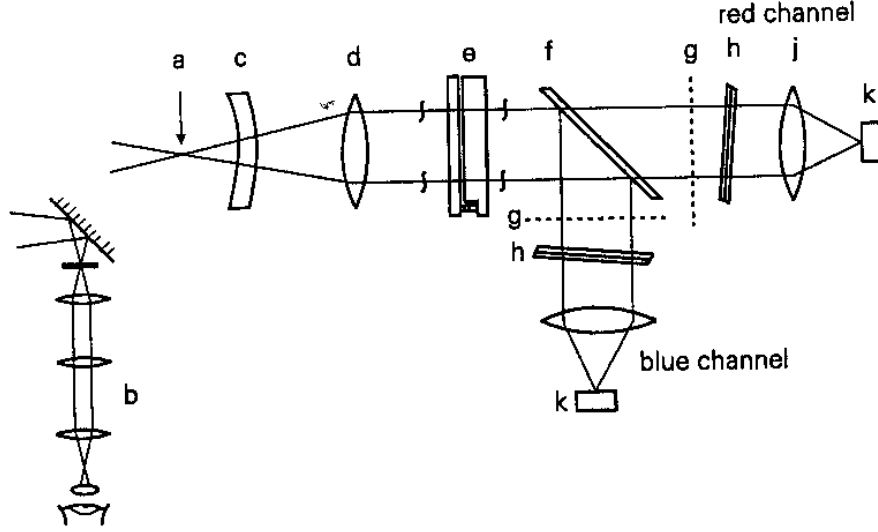
Figure 2.5: This is the optical scheme of the Two-Channel Focal reducer used for the ground observations. The single elements are labeled. (a) Cassegrain focal plane, (b) offset guider, (c) field lens, (d) collimater, (e) Fabry-Perot etalon or four-beam Wollaston prism, (f) color divider, (g) Lyot stop, (h) filter, (j) camera lens, (k) CCD detector. If position (e) is empty, the right part of the instrument can be moved to the left toward the Cassegrain focal plane in order to reduce vignetting (Jockers, 2000).

Table 2.5.

2.3.1   Data Reduction

All continuum images obtained from the Pik Terskol observation campaign have been reduced with the software library *frisoft*[2] and IDL's *astrolib*. The image reduction process included bias substraction, flat-fielding, and removal of cosmic rays and star trails which were situated closed to the dust coma on the images and hence could influence the analysis of the dust coma. Afterwards the images were corrected for extinction and then absolutely calibrated (using the Hamuy catalogue (1992 & 1994), see Table 2.6 for the standard stars used). They were then normalized to the mean intensity of the solar disk at the corresponding wavelengths. The calibration is based on the following equation:

$$m_{inst} = m_{AB} + \Delta_m + k \cdot A \tag{2.2}$$

m_{AB} is the absolute brightness of a Hamuy standard at a specific wavelength,

---

[2]Provided by Professor K. Jockers, Max-Planck-Institut fuer Sonnensystemforschung, Katlenburg-Lindau, Germany

Parameter	
Filters	
IF444+BB	443.5 nm/4.2 nm
IF526	525.5 nm/4.3 nm
IF631	630.8 nm/3.1 nm
IF642	641.6 nm/2.6 nm
Other parameters	
Camera lenses	f=140 mm, 420< λ <700 nm
FOV	7.8' x 5.2'
CCD	512 x 512 pixel
Pixel size	27 μm
Scale	0.81" px^{-1}

Table 2.5: This table gives the basic parameters for the instrumentation. The two values describing the filters are the central wavelength and the full width at half maximum. The second part of the table contains the optical layout.

Δ_m is the constant correction factor, k the extinction coefficient, and A is the airmass. m_{inst} is the so called instrumental brightness and connected with the image $B1$ (in Eq. 2.3) taken in ADU/s by the relation:

$$m_{inst} = -2.5 \cdot \log(B1) + 20 \tag{2.3}$$

To get Δ_m and k, the $m_{inst} - m_{AB}$ relation has to be extracted from standard stars images and the Hamuy catalogue and then plotted against the airmass at the time of observation. k is derived by the slope of the curve and Δ_m by the intersection of the curve with the y-axis. Afterwards these parameters are used to get the absolute brightness of the cometary images following Equation 2.2 and 2.3. To convert the brightness, m_{AB}, into flux one has to use the equation (Hamuy, 1992 & 1994)

$$m_\nu = -2.5 \cdot \log(F_\nu) - 48.59 \tag{2.4}$$

m_ν and F_ν are the magnitude and flux at a specific frequency, respectively. The resulting fluxes are in [erg/cm^2/s/Hz]. Multiplying the fluxes with c/λ^2, where c is the speed of light, results in [erg/cm^2/s/Å]. By dividing the fluxes over the solid angle of 1 pixel one obtains the images in intensity units.

HR	Star	MK Type	(U-B)	(B-V)	V
718	ξ^2 Cet	B9 III	-0.107	-0.056	4.279
1544	π^2 Ori	A1 V		0.01	4.355

Table 2.6: This table lists the secondary standard stars used to calibrate the cometary images.

Chapter 3

Scattering Properties of Dust Grains

The spectacular appearance of a bright comet is because of a cloud of micrometer sized dust particles entrained in the gas stream which leaves the nucleus. As the sun light is scattered by these very small grains, the physical and optical properties of cometary dust grains are of interest. By analyzing the scattering of light by particles information about the physical and chemical properties of the scatterers and the grain size distribution can be derived. To receive the surface brightness of the dust coma of a comet, the scattering properties of the dust grains, like the scattering, absorption and extinction efficiencies and the phase function, are needed. This chapter explains the methods which are used in this thesis to obtain the required optical quantities.

3.1 Optical Properties

Interpretation of cometary observational data of radiation scattered and emitted by cometary dust requires variables such as the efficiencies for scattering (Q_{sca}), absorption (Q_{abs}), extinction ($Q_{ext} = Q_{ext} + Q_{abs}$) and radiation pressure (Q_{pr}). As defined in detail by Hansen and Travis (1974) and others, these four quantities represent the dimensionless ratios of the effective cross-sections for the four processes to the geometric cross-section of an individual particle, i.e.,

$$Q_{ext} = \frac{\sigma_{ext}}{\pi r^2}, \quad Q_{sca} = \frac{\sigma_{sca}}{\pi r^2}, \quad Q_{abs} = \frac{\sigma_{abs}}{\pi r^2}, \quad Q_{pr} = \frac{\sigma_{pr}}{\pi r^2} \tag{3.1}$$

These values may depend on wavelength and on the size, shape, orientation and material properties (e.g., refractive index) of the particle. Light diffracted by a particle is included in both, the scattering and extinction efficiencies, and in the scattering function Φ_s, which also depends on the scattering angle $\theta_s = (\pi - \alpha)$,

where the phase angle α is formed by the vertex Sun-dust-observer.

The scattering function Φ_s of a dust particle can be described as the differential scattering behavior of the grain with angle. For the brightness calculations, the normalization

$$\int_{4\pi} \Phi_s d\Omega = 2\pi \int_0^\pi \sin\theta_s \Phi_s d\theta_s = 1 \qquad (3.2)$$

is adopted.

Other parameters which play an important role in the evaluation of scattered light by dust particles are the albedos, whereby one has to distinguish between different definitions. The single scattering albedo ω of a single particle is defined as the ratio of the energy scattered in all directions to the total energy removed from an unidirectional incident beam at a given wavelength (Hanner *et al.*, 1981), in the form

$$\omega = \frac{Q_{sca}}{Q_{ext}} \qquad (3.3)$$

In contrast, the geometric albedo p is defined as the ratio of energy scattered by the particle at $\theta = 180°$ (backscattering) to that scattered from a white Lambert disc of the same geometric cross section. This definition can be expressed as

$$p = \pi\omega Q_{ext}\Phi_\pi \qquad (3.4)$$

the subscript π implies evaluation at $\theta_s = 180° = \pi$ radian.

To calculate the necessary optical parameters for the interpretation of the observational data of cometary dust coma, the grains are considered to be nonspherical. The scattering behavior of dust particles differ with their sizes and wavelengths. Generally it is known that dust particles scatters strongly at wavelengths comparable to their sizes. Scattered sunlight between 400 to 600 nm can roughly be attributed to sizes between 1 to 10 μm because of the higher scattering efficiencies of these particles in this wavelength range and because the number density decreases strongly with increasing particle size. Larger grains up to several 100 μm, are observed only occasionally in "antitails" (Ney, 1985; Grün and Jessberger, 1990). However the similarity of comet and meteor stream orbits indicates the release of centimeter-sized grains from comets.

For small dust grains with sizes comparable to the wavelength, the semi-empirical model of Pollack and Cuzzi (1979) is adopted to determine the optical properties of nonspherical particles at wavelengths comparable to the grain size. The

scattering quantities for particles bigger than a few microns has been calculated by a geometrical optics approximation, applying the ray tracing code (RTC) of Macke (1993).

3.2   Scattering by Nonspherical Particles

Pollack and Cuzzi (1979) proposed a semi-empirical approach to calculate the scattering properties of particle ensembles based on laboratory experiments. Their treatment of light scattering by randomly-oriented, irregularly-shaped particles of size comparable to a wavelength is a combination of Mie theory (Hulst van de, 1981), physical optics, geometrical optics and parametrization. To get the optical properties of the cometary dust grains it is assumed that the grains are randomly oriented, nonspherical particles. The dimension of the particles is described by the particle size parameter, x,

$$x = \frac{2\pi a}{\lambda} \qquad (3.5)$$

where a is the particle radius and λ is the wavelength. When x is less than some upper bound x_0, see section 3.2.1, Mie theory is used to calculate the cross-section and phase function. For larger particles, appropriately scaled Mie theory results are used to define the cross-section, and the phase function is constructed from the sum of three components (those due to diffraction, external reflection and internal transmission).

3.2.1   Small-size regime

The small particle regime is defined by the criterion that $x \leq x_0$ where the particle radius used to obtain x is found from the equivalent sphere's dimensions and x_0 is a parameter to be obtained from experimental results. Typically $x_0 \approx 5$. Within this size regime Mie scattering theory is applied to the equivalent spheres to determine the phase function and the efficiencies for absorption, scattering and extinction.

3.2.2   Large-size regime

To construct the phase function of large particles, the three components have to be calculated separately.

Diffraction component   The diffracted component is assumed to be that of an opaque circular disk having an area equal to the irregular particle's projected area. Since irregular particles always have greater surface areas than that of an equal volume sphere, the radius of the disk, $\tilde{a}$, will be larger than that of the

equivalent sphere a. In particular, $\tilde{a} = \sqrt{ra}$ where r is the ratio of the surface area of the irregular particle to that of its equivalent volume sphere. Following Hodkinson and Greenleaves (1963) the approximated diffraction component due to a particle of size $\tilde{x}$ is

$$
\begin{aligned}
d(\tilde{x}) &= C_D \frac{(\tilde{x})^2}{4\pi} \left[\frac{2J_1(z)}{z} \right]^2 k \\
&\approx \frac{2C_D \sin^2(\tilde{x} \sin\theta - \pi/4)k}{\pi^2 \tilde{x} \sin^3 \theta}
\end{aligned}
\tag{3.6}
$$

where

$$
z = \tilde{x} \sin\theta = \frac{2\pi\tilde{a}}{\lambda} \sin\theta
\tag{3.7}
$$

$$
k = \frac{1}{2} \left(1 + \cos^2 \theta \right)
\tag{3.8}
$$

The phase function for diffraction is then given by

$$
I_D = \int_{x_0}^{\infty} d(\tilde{x}) \pi \tilde{x}^2 n(\tilde{x}) d\tilde{x}
\tag{3.9}
$$

where $n(\tilde{x})$ is the size distribution of interest and C_D is obtained from the usual normalization condition

$$
\int I_D \frac{d\Omega}{4\pi} = 1
\tag{3.10}
$$

The left-hand side of Equation 3.10 involves an integration over solid angle. θ is the scattering angle. The right side of the first equation of Eq. 3.6 represents the exact physical optics solution for an opaque disk The second part of the same equation is found by approximating the first-order Bessel function J_1.

It is assumed that particles in the large size regime diffract an amount of energy equal to that falling on its physical cross-section according to Babinet's principle (Hulst van de, 1981). Thus the diffraction contribution to the extinction efficiency Q_D equals 1.

External reflection component For sizes large enough for geometrical optics to be valid ($x \geq 100$), a randomly oriented ensemble of convex, irregular shaped particles reflects light incident on their surfaces in precisely the same manner as an ensemble of equal area spheres with the same refractive indices (Hansen and Travis, 1974). It is assumed that the geometrical optics expressions for external reflection can be applied to all particle sizes in the large size regime, i.e., $x > x_0$.

Therefore, the phase function for external reflection, I_R, by irregular particles is proportional to the Fresnel reflection coefficients (Hodkinson and Greenleaves, 1963):

$$
\begin{aligned}
I_R &= 1/2 C_R \left\{ \frac{\sin(\theta/2) - [|\tilde{x}|^2 - 1 + \sin^2(\theta/2)]^{1/2}}{\sin(\theta/2) + [|\tilde{x}|^2 - 1 + \sin^2(\theta/2)]^{1/2}} \right\}^{1/2} \\
&+ 1/2 C_R \left\{ \frac{|\tilde{m}|^2 \sin(\theta/2) - [|\tilde{x}|^2 - 1 + \sin^2(\theta/2)]^{1/2}}{|\tilde{m}|^2 \sin(\theta/2) + [|\tilde{x}|^2 - 1 + \sin^2(\theta/2)]^{1/2}} \right\}^{1/2}
\end{aligned}
\tag{3.11}
$$

where

$$
|m|^2 = m_r^2 + m_i^2
\tag{3.12}
$$

and C_R is found using the normalization

$$
\int I_R \frac{d\Omega}{4\pi} = 1
\tag{3.13}
$$

m_r and m_i refer to the real and imaginary indices of refraction. The efficiency factor for external reflection Q_R is related to C_R by

$$
Q_R = \frac{1}{C_R}
\tag{3.14}
$$

Note that both I_R and Q_R are independent of particle size for all $x > x_0$.

Transmitted component The transmitted component is primarily responsible for the deviation in the scattering behavior of irregular particles from that of their spherical counterparts. This component is parameterized by Pollack and Cuzzi in accord with the observed scattering behavior of a wide range of particle shapes and sizes. They assumed that the logarithm of the transmitted component's phase function, I_T, varies in a linear manner with scattering angle, i.e.,

$$
I_T = C_T \exp(1 + b\theta)
\tag{3.15}
$$

where C_T is again derived from the normalization

$$
\int I_T \frac{d\Omega}{4\pi} = 1
\tag{3.16}
$$

The empirical constant b is specified in terms of a second and more physically meaningful empirical constant G by

$$G \equiv \int_0^{\pi/2} I_T d\theta \Big/ \int_{\pi/2}^{\pi} I_T d\theta \qquad (3.17)$$

which can be straightforwardly evaluated to provide an analytical relation between b and G. b is the slope of the $\log I_T$ and θ relationship. G is explained to be equivalent to the ratio of energy scattered into the two hemispheres.

The scattering efficiency for the transmitted component Q_T is found by subtracting the total Mie scattering efficiency for the large-size regime Q_s^L by the sum of the diffraction and externally reflected efficiencies:

$$Q_T = Q_s^L - Q_D - Q_R \qquad (3.18)$$

where

$$Q_s^L = \int_{x_0}^{\infty} Q_s(x) n(x) \pi x^2 dx \Big/ \int_{x_0}^{\infty} n(x) \pi x^2 dx \qquad (3.19)$$

Here Q_s is the Mie scattering efficiency for a particle with size parameter x and $n(x)$ is the size distribution function for equal volume spheres.

Composite phase function and efficiencies   The Mie scattering and absorption efficiencies, Q_s^L and Q_a^L, for particles in the large size regime and for those in the small size regime, Q_s^S and Q_a^S are obtained in a similar way. The composite scattering, absorption and extinction efficiencies, Q_s^*, Q_a^* and Q_e^* for the entire ensemble of irregular particles are given by

$$Q_s^* = Q_s^L \cdot F \cdot r + Q_s^S \cdot (1 - F) \qquad (3.20)$$
$$Q_a^* = Q_a^L \cdot F + Q_a^S \cdot (1 - F) \qquad (3.21)$$
$$Q_e^* = Q_s^* + Q_a^* \qquad (3.22)$$

where

$$F = \int_{x_0}^{\infty} n(x) \pi x^2 dx \Big/ \int_0^{\infty} n(x) \pi x^2 dx \qquad (3.23)$$

In cases where the particles are so highly absorbing that $2m_i x > 1$ in the large-size regime, the first term on the right-hand side of Eq. 3.21 should be multiplied by r.

The composite phase function Φ_s is obtained from the phase functions for scattering in the small-size regime, I_S, and for diffraction, external reflection and transmission in the large-size regime, I_D, I_R and I_T. Each of these component

phase functions has been normalized to unity over the solid angle. The composite phase function is obtained by summing the four individual components, with each one being weighted by its contribution to the total scattering:

$$\Phi_s = I_s \cdot (1 - F) \cdot \frac{Q_s^S}{Q_s^*} + r \cdot F \cdot \frac{Q_s^L}{Q_s^*} \times \left(I_D \cdot \frac{Q_D}{Q_s^L} + I_R \frac{Q_R}{Q_s^L} + I_T \frac{Q_T}{Q_s^L} \right) \qquad (3.24)$$

3.3   Cometary Dust Particles

Before the Halley encounter, the dust size distribution of comets was determined from optical observations of dust tails following the approach of Finson and Probstein (1968). An overview of the "pre-Halley encounter" knowledge of the dust and gas is given by Divine *et al.* (1986). The encounter finally brought, qualitatively and quantitatively an increased knowledge of the composition of cometary dust. Onboard the three spacecraft Giotto, Vega 1 and Vega 2, impact ionization time-of-flight mass spectrometers (PIA , PUMA 1 and 2 respectively) facilitated for the first time *in situ* analysis of the solids in a cometary coma (e.g. Kissel *et al.*, 1986a, 1986b; Langevin *et al.*, 1987) The three important results of the data analysis were:

- The dust was, in greatly varying proportions, composed of a silicate component and a refractory organic component, termed "silicates" and "CHON", respectively.

- The average abundances of the rock forming elements were, within a factor of two, the same as their abundances in carbonaceous chondrites and in the Sun.

- The abundances of the CHON elements were much higher than in any meteorite; especially those of C and N approach solar abundances.

A further understanding of cometary dust resulted from the infrared emission observations of various comets provided by Greenberg and Li (1999) and Greenberg and Hage (1990). They demonstrated, by comparing results of Halley (a periodic comet), Borrelly (a Jupiter family short period comet), Hale-Bopp (a long period comet), and extra-solar "comets" in the β Pictoris disk, that distinctly different types of comets bear a general resemblance to each other. While Greenberg and Li acknowledged that distinctions from comet to comet in the details of the emission exist, one can still adopt a uniform approach by describing cometary dust as aggregates of submicron size interstellar dust which are themselves composed of silicate core-organic refractory mantle particles (Li and Greenberg, 1997).

3.3.1   Halley's Dust Composition

Immediately after the Halley encounters in March 1986, the first data showed that some spectra are dominated by ions from the elements H, C, N, and O, while in

other spectra these ions were virtually absent and instead the rock-forming elements Mg, Si, and Fe were the most abundant ions (Kissel *et al.*, 1986). This led to the designation "CHON" and "silicate" particles respectively. The given abundances of these two compositions in the comet vary from author to author (e.g. Langevin *et al.*, 1987; Jessberger *et al.*, 1988). But this situation also arose because of the different definitions of CHON, mixed and silicate particles.

Langevin *et al.* (1987) found the abundances of CHON, silicate and mixed (silicate and CHON) particles to be one third each, by analyzing 2204 mass spectra of cometary grains obtained by PUMA 1. In the same paper they found 20% silicate, 40% CHON, and 40% mixed particles from 2784 spectra from PIA. A detailed study of 79 spectra involving cluster analysis by Jessberger *et al.* (1988) revealed that 72% of the particles are CHON-dominated and 28 % of the particles are dominated by Mg, Si, and Fe. Common to all studies is the clear evidence that the cometary dust is a mixture of CHON-rich and silicate-rich material present in highly variable proportions. Another significant observation made is the compositional variation with time (which in this case is equivalent to distance from the nucleus because of the motion of the spacecraft). Langevin *et al.* found that the proportion of CHON decreased towards closest approach to the nucleus.

A further analysis of Halley's dust particles has been performed by Greenberg and Hage (1990) based on simultaneous observations of three properties of cometary dust: The chemical composition (1) and the size (mass) distribution (2) of the dust, which has been obtained from the *in situ* measurements and summarized before, and the infrared emission (3) observation of Halley's dust in the same time period (March 1986) by Hanner *et al.* (1987). Greenberg and Hage attempted to fit a model which satisfies simultaneously such independent characteristics. They concluded that Halley's dust was explained best by very fluffy aggregates of submicron interstellar dust with silicate core and organic refractory mantle. This model is supported by the *in situ* mass spectra of Halley, showing that its dust is an intimate mixture of silicate and carbonaceous materials rather than separate silicate and carbon components.

The results Greenberg and Li (1999) summarized for the dust of Halley are: (1) comet dust consists of aggregates of 0.1 μm silicate core-organic refractory mantel particles; (2) the average porosity of the comet dust is $0.93 < P < 0.975$. The inferred comet dust density is $0.08 \leq \rho_{CD} \leq 0.16$ g cm^{-3}; whereby $\rho_{CD} \approx$ 0.1 g cm^{-3} is a reasonably canonical value.

3.3.2 Borrelly's Dust Composition

It has become accepted that silicates are a major component of cometary dust particles since the 10 μm Si-O stretching emission feature was first detected in comet Bennett (Maas *et al.*, 1970). As discussed above, mass spectroscopic evi-

dence of the Giotto/Vega space probes showed that refractory material in comet dust consisted of both: organic elements (O, C, N) as well as the rocky elements (Mg, Si, Fe).

However, all previous detections of silicate emissions were restricted to long period comets until Hanner *et al.* (1996) discovered the 10 μm silicate feature in two short period comets, comet P/Borrelly and comet P/Faye. They modeled the thermal emission spectrum of comet Borrelly in terms of either a mixture or a simple combination of two separate components of compact amorphous silicate (bronzite or olivine) and glassy carbon grains. Their models, using the Hanner size distribution form (Hanner *et al.*, 1985)

$$n(a) = \left(1 - \frac{a_0}{a}\right)^M \left(\frac{a_0}{a}\right)^N \qquad (3.25)$$

fit the observations reasonably well. Here a_0 denotes the minimum grain radius, N defines the slope of the size distribution for large radii and M is related to the peak radius through

$$a_p = a_0 \frac{(M + N)}{N} \qquad (3.26)$$

Li and Greenberg (1998) calculated the thermal emission spectrum of the dust of comet P/Borrelly from 3 μm to 14 μm and the 10 μm silicate feature, taking into account that the comet's dust is a fluffy aggregates of core-mantle interstellar particles. They used the optical constants, i.e. the complex indices of refraction ($m(\lambda) = m(\lambda) - im''(\lambda)$) for interstellar grains, which is based on the determination of the composition of interstellar core-mantle grains found by fitting both the interstellar extinction curve and interstellar polarization (Li and Greenberg, 1997).

For the 10 μm silicate emission feature, they employed amorphous olivine for the silicate core, using the $m''(\lambda)$ for amorphous olivine $MgFeSiO_4$ for wavelengths longward to 2 μm. For 0.3 μm $\leq \lambda \leq 2\mu$m, they adopted the $m''(\lambda)$ of Draine (1984). For wavelengths shorter than 0.3 μm, they adopted the $m''(\lambda)$ of crystalline olivine. The real part of the optical constants $m'(\lambda)$ was calculated from $m''(\lambda)$ by using the Kramers-Kronig relation[1].

For the grain mantle, they employed the optical constants of H, C, O, N-rich organic refractory residues (Li and Greenberg, 1997) and of amorphous carbon by Rouleau and Martin (1991).

---

[1]The Kramers-Kronig relations (e.g. Landau and Lifshitz, 1960) imply that the real and imaginary parts of the complex dielectric function $\epsilon(\omega) = \epsilon_1 + i\epsilon_2$ are not independent.

The dust size (mass) distribution was taken from the Halley observations of the spacecrafts Giotto, Vega 1 and Vega 2, see Figure 3.1 (Greenberg and Hage, 1990). By taking the nucleus density of 0.3 g cm^{-3} and a porosity P = 0.975, Li and Greenberg deduced a grain mass density of 0.07 g cm^{-3} for the silicate core - organic refractory mantle particles. For the mass ratio of the organic refractory mantle to the silicate core, they adopted m_{or}/m_{si} =1, according to the mass spectrometer onboard Vega 1.
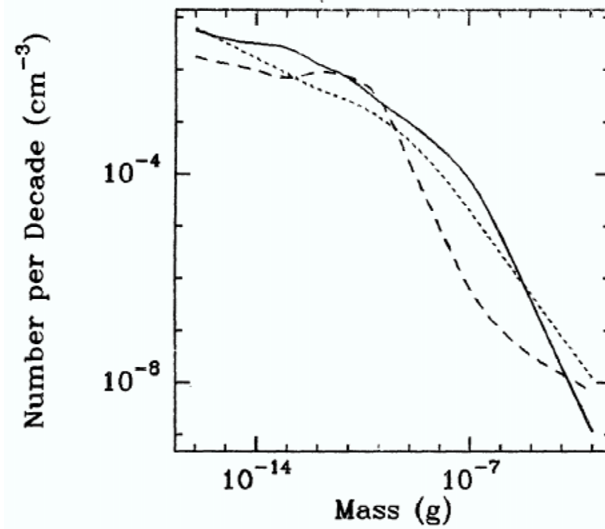
Figure 3.1: This are the number of particles per mass decade in the coma of comet Halley as measure in situ by the various space probes. Vega 1: continous line; Vega 2: short-dashed line; Giotto: long dashed line: (Greenberg and Hage, 1990).

With these inputs they could obtain a reasonable fit to the observed NIR spectra of Borrelly. But a better fit was obtained with the model of silicate core - amorphous carbon mantle grains (highly processed organic which are depleted in H, O, N) with a porosity of 0.85. Their analysis showed that compared to Halley's dust, the dust grains of Borrelly appear to be more processed (more carbonized), less fluffy, and richer in smaller particles. They explained that since P/Borrelly has passed through the inner Solar System many more times than Halley and therefore been subjected much more to solar irradiation, the dust grains within the surface layer of the nucleus could have been significantly modified. In particular, the organic refractory materials could have undergone further carbonization; namely, the organic materials, would partially lose their H, O, N atoms and thus become carbon-rich (Jenniskens et al., 1993).

A'Hearn et al. (1995) (also Cochran and Barker (1999)) assigned Borrelly to the

group of comets which are depleted in carbon-chained molecules[2](C_2 and C_3). However they found CN to be approximately constant. For all comets observed they concluded that most of the CN comes from grains, the fraction of C_2 which comes from grains is smaller than for CN. This conclusion is partly consistent with Li and Greenberg's idea of carbonization. But they further derived a depletion of H, O, and N of the organic materials which does not explain well the constant amount of CN.

3.4 Deriving Optical Properties

Summarizing the above discussion on the chemical composition of Borrelly and Halley, it is recognized that an unambiguous choice for the dust grains components cannot be made. Because of that it has been decided to investigate the presence of all three mentioned components, silicate, organic refractory and amorphous carbon with various dust types. Following compositions have been studied:

- Dust grains containing only silicate or organic refractory.

- Core-mantle dust grains with a silicate core and a organic refractory or amorphous carbon mantle. Figure 3.2 (left) gives a schematic example of a core-mantle particle.

- Dust grains containing a mixture of two components, which can be described by Figure 3.2 (right).
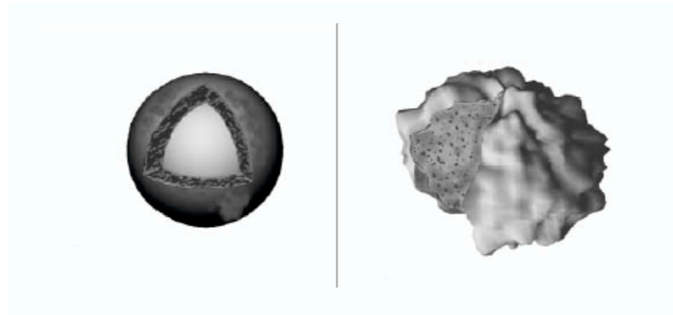
Figure 3.2: Schematic drawing of a core mantle (left) and a mixed component particle (right) (Davidsson and Skorov, 2002).

---

[2]A'Hearn et al. summarized the properties of 85 comets which have been observed photometrically between 1976 - 1992. From their observations they could set up a comet taxonomy, separating these bodies into two groups, based on the correlation between the productions ratios of $Q(C_2)/Q(OH)$ and $Q(CN)/Q(OH)$. The group showing a strong correlation they called *typical* and the others they named *depleted*.

3.4.1   Refractive Indices

To derive the phase function and the scattering efficiency according to the scattering theory of Pollack and Cuzzi (1979), the complex refractive indices for "astronomical silicates" of Draine and Lee (1984) at the required wavelengths have been used for the silicate component. The derivation of the indices has been based on lab measurements of crystalline olivine.

Weingartner and Draine (2001) published corrected values for the above mentioned complex refractive indices of astronomical silicates calculated Draine and Lee. Their motive to revise the refractive indices was a feature at 6.5 μm^{-1} found in the dielectric function derived by Draine and Lee (1984). This characteristic is not present in the observed interstellar extinction or polarization. Weingartner and Draine obtained the new dielectric function by removing the absorption feature at 6.5 μm^{-1} from the imaginary part of the dielectric function.

For abbreviation the astronomical silicates of Draine and Lee are denoted as Type I and the corrected one Type II. As this procedure has been applied to fit interstellar dust, which do not implicitly must have the same composition like cometary dust, both silicates has been investigated.

For the organic refractory, the optical constants of Jenniskens (1993) have been employed. He used a frozen gas mixture, consisting of H_2O, CO, CH_4 and NH_3 in a ratio that is thought to represent interstellar ice mantles. As the organic refractory is the matter that remains on interstellar dust grains after the sublimation of photoprocessed dirty ice mantles, they irradiated the sample to let it sublime.

The optical properties for amorphous carbon (AC data sample) have been taken from the work of Rouleau and Martin (1991). The AC data were based on the experiment which produced soot by striking an arc between two amorphous carbon electrodes in a controlled argon atmosphere.

For dust grains of only one component, the efficiencies and phasefunction are calculated by a conventional Mie scattering code. The optical parameters for core-mantle particles were computed using the DMILAY code written by O.B. Toon, T.P. Ackerman, and W. Wiscombe (Toon and Ackerman, 1981). The mass ratio of the organic to the silicate component was chosen to be 1 resulting in a core-to-shell radius ratio of q = 0.679.

For the external reflection component of the large size regime of Pollack and Cuzzi, see Equation 3.12, two refractive indices are possible. First by assuming the mantle component to be only responsible for the external reflection, second by considering the influence of the core material as well. The combined refractive

index for core-mantle particle is given by Greenberg and Hage (1990) as

$$m_{eff} = ms\sqrt{1 + 3q^3\left(\frac{m_c^2 - m_s^2}{m_c^2 + 2m_s^2}\right)\left(1 - q^3\left(\frac{m_c^2 - m_s^2}{m_c^2 + 2m_s^2}\right)\right)^{-1}} \qquad (3.27)$$

For the particles containing a mixture of silicate and organic refractory or silicate and carbon the effective refractive index can be calculated following Maxwell-Garnett theory:

$$m_{eff}^2 = \frac{(1 - \sum \varphi_i)m_m^2 + \sum \varphi_i \left[\frac{3m_m^2}{m_i^2 + 2m_m^2}\right]m_i^2}{1 - \sum \varphi_i + \sum \varphi_i \left[\frac{3m_m^2}{m_i^2 + 2m_m^2}\right]} \qquad (3.28)$$

where m_m is the refractive index of the matrix material and m_i is the index of the inclusions. φ_i stands for the filling factor of the single i-species inclusion, which can be interpret as the volume fraction of the inclusion. For the silicate component an averaged density of $\rho = 3500$ kg m^{-3} for two crystalline olivines (crystalline forsterite, Mg_2SiO_4, $\rho = 3210$ kg m^{-3} and crystalline fayalite, Fe_2SiO_4, $\rho = 4390$ kg m^{-3}) has been applied. The density of $\rho = 1600$ kg m^{-3} provided by Jenniskens (1993) has been employed for the organic refractory contribution and the density of the amorphous carbon is $\rho = 1850$ kg m^{-3} (Rouleau and Martin, 1991).

All refractive indices of the specific components in the wavelength ranges of the MICAS and Pik Terskol detectors are given in Table C.1 and C.3 in the Appendix. Also the resulting refractive indices calculated by Equation 3.28 for different mixtures are listed there, Table C.2 and C.4.

3.4.2   Dust Grain Sizes

For Borrelly, it was decided to use the dust size distribution of Hanner *et al.* (1985), see Equation 3.25. The peak grain radius, which is described in Equation 3.26, has been chosen to be $a_p = 5.4$ μm according to Borrelly's heliocentric distance of 1.47 AU in September 2001. This value has been derived from Fig. 3.3 assuming Borrelly's particle size distribution to be similar to the one of comet Churyumov-Gerasimenko.

Divine *et al.* (1986) summarized the peak grain radius obtained from model fits of thermal infrared data performed by Hanner (1983) and Hanner *et al.* (1985) for several comets. They obtained a_p by adopting $a_0 = 0.1\mu$m and $N = 3.7$ (which has been derived from dynamical considerations).
Therefore $N = 3.7$ and $a_0 = 0.1$ μm. M is derived from Equation 3.26 for given a_p and a_0.
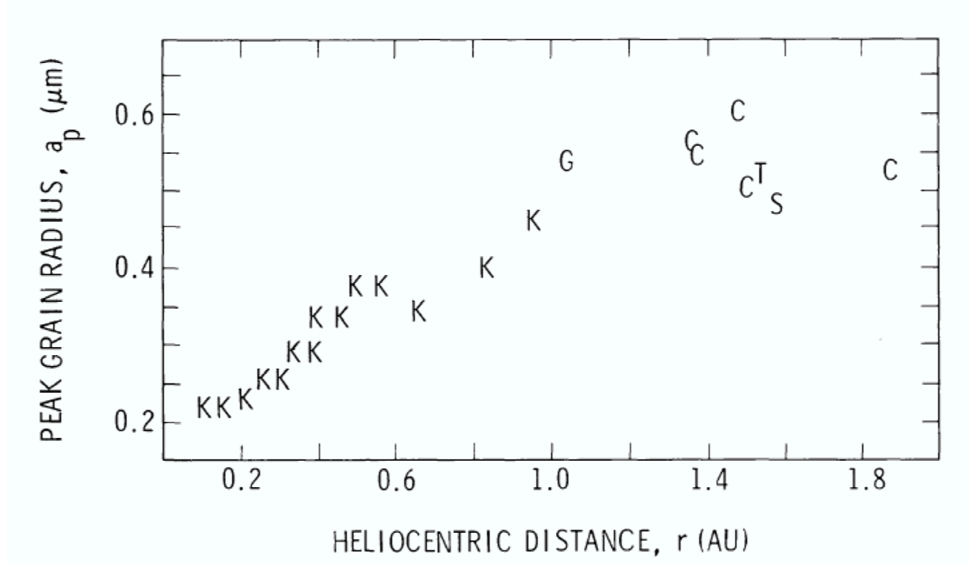
Figure 3.3:   Peak grain radius versus heliocentric distance for comets
75P/Kohoutek (K), 67P/Churyumov-Gerasimenko (C), 26P/Grigg-Skjellerup
(G), 9P/Tempel 1 (T), and 38P/Stephan-Oterma (S) (Divine *et al.*, 1986).

For Halley's dust, the particle size distribution reported from *in situ* measure-
ments of comet Halley by the highly sensitive mass spectrometer, PIA, and the
dust shield detector system, DIDSY, onboard Giotto has been applied (McDon-
nell *et al.*, 1991).

To constrain the particle sizes which will be employed, the radius of the maximum
liftable particle is derived. According to the theory of dust release from a nucleus
surface, a particle of radius a and density ρ will be dragged away by the subliming
gases if the drag force (F_D) overcomes the gravitational attraction (F_G) of the
nucleus,

$$F_D - F_G > 0 \tag{3.29}$$

Huebner (1970) gave, based on this consideration, an estimate for the maximum
particle size, a_{max}, that can leave the nucleus (ignoring centripetal force)

$$a_{max} = \frac{9}{16\pi} \frac{m_u M Z v_g}{G \rho_d \rho_N R_N} \tag{3.30}$$

where G is the gravitational constant ($6.674 \cdot 10^{-11}$ Nm^{2}kg^{-2}), m_u the unit atomic
mass ($1.66 \cdot 10^{-27}$ kg), and M the molecular weight. Z is the gas production rate
(molecules m^{-2}s^{-1}) from a subliming surface. The density and radius of the
cometary nucleus are described as ρ_N and R_N, respectively. v_g is the gas outflow
velocity near the nucleus and is assumed to be $v_g \simeq 100$m/s. ρ_d denotes the

density of the dust grains.

From several observational data, Borrelly's water production rate of $Q_{H_2O} = 3.0 \cdot 10^{28}$ molecules s^{-1} (Weaver *et al.*, 2003) is taken as an upper limit for the gas production rate. Assuming isotropic gas outflow, Z can be derived via

$$Z = \frac{Q_{H_2O}}{4\pi R_N^2} \qquad (3.31)$$

Further $R_n \approx 2.65$ km (equivalent to the effective radius of a nucleus of 8.4 x 4.2 x 4.2 km [3]), $\rho_n = 180$ kg m^{-3} (Davidsson and Gutiérrez, 2004). For dust particles of density $\rho = 2200$ kg m^{-3} (which is about the mean density of all considered particles), see also Table C.3, a value of $a_{max} \cong 0.0026$ m is obtained without considering porosity.
If a porosity of P = 0.64 is included, a_{max} will increase to 0.007 m. Therefore a mean value $a_{max} \simeq 0.005$ m is used. Consequently the particle sizes which are taken into account for the calculations range between $1 \cdot 10^{-7}$ to 0.005 m.

For the nonspherical particle scattering theory of Pollack and Cuzzi (1979), the free parameters x_0 (see section 3.2.1), G (see equation 3.17) and r (see section 3.2.2), which are dependent on the particles shape, has to be chosen. For this work the shape of the particles is assumed to be convex-concave. Thus the model parameters derived by Pollack and Cuzzi can be used. Table 3.1 gives the value for these parameters.

Free parameter	Value
x_0	10
G	3-4
r	1.3

Table 3.1: The free parameters of the scattering theory derived by Pollack and Cuzzi (1979) by matching the measurements of a sample of convex-concave particles. x_0 defines the upper bound size parameter, r is the ratio of the surface area of the irregular particle to the one of equivalent volume sphere and G denotes the empirical constant for the transmitted component of the scattering theory.

3.4.3 Optical Parameters for the VISCCD Data

The optical properties such as the scattering, absorption and extinction efficiencies and the phase function of particles of sizes comparable to the wavelength range 500 - 1000 nm, have been calculated for the mentioned particle compositions. The approach of Pollack and Cuzzi (1979) have been used for a size

---

[3]The shape of the nucleus is assumed to be an ellipsoid and Borrelly's dimension is taken as its semi major axis.

parameter range between $1 < x < 25$. The optical constants for the intermediate size regime $50 \leq x \leq 400$ has been calculated with the ray tracing method of Macke (1993). The efficiencies and the phase functions for sizes in between $25 \leq x \leq 50$ have been interpolated.

The results of the brightness calculations following in chapter 4, showed that the contribution of particles, which are much larger than the observed wavelengths do not have a major influence on the resulting intensities of the coma with the applied particle size distribution.

1-Component Particles

The efficiencies for the pure silicate and pure organic refractory particles are listed in Table 3.2. The efficiencies of the Type II astronomical silicates have been omitted here. Their values are very similar to those of Type I.

Optical	Wavelengths [nm]					
constants	500	600	700	800	900	1000
Astronomical silicates (Type I)						
Q_{scat}	1.77857	1.78609	1.79591	1.81488	1.83378	1.85532
Q_{abs}	0.896072	0.884213	0.875043	0.862659	0.854028	0.845759
Q_{ext}	2.67464	2.67030	2.67095	2.67754	2.68780	2.70108
Organic refractories						
Q_{scat}	1.54414	1.52431	1.50975	1.49580	1.48415	1.47751
Q_{abs}	1.08325	1.09945	1.11268	1.12684	1.14073	1.15185
Q_{ext}	2.62738	2.62376	2.62243	2.62263	2.62488	2.62936

Table 3.2: The optical constants of particles, which consist only of astronomical silicates (Type 1) and organic refractories at the VISCCD wavelengths. The particle size distribution of Hanner *et al.* (1985) has been applied with a peak radius of $a_p = 0.54$ μm.

As expected, silicate particles scatter more light than organic refractory particles. The organics are more absorbent. The scattering efficiency of the silicate grains increases from 500 nm to 1000 nm, whereby its absorption decreases. An opposite behavior is observed with the organic refractory particles, where their absorption efficiency increases with wavelength while their scattering efficiency decreases.

The phase function of the pure silicate grains shows the typical strong forward scattering peak and the increase in backscattering (Figure 3.4). In the same Figure, the phase function of the astronomical silicates Type II is plotted, which is slightly lower than for the astronomical silicate Type I. Nevertheless they have similar behavior. For organic refractory grains, no backscattering peak is observed

(Figure 3.4). The phase function flattens at scattering angles $> 100°$ and does not increases again.

Core-mantle particles

The resulting optical constants of the silicate core-organic refractory mantle particles are presented in Table 3.3. This table contains the results of the particles with refractive indices defined by Equation 3.27 for the external reflection component, i.e. both, core and mantle component contribute to the external reflection (Eq. 3.11 and 3.12). The results considering only the mantle component to be responsible for the reflection part are similar, therefore they have been omitted. The resulting optical constants of the particles which consist of astronomical silicates Type I and Type II are again similar. Thus it is decided for the upcoming analysis and discussion just to use the refractive index of Type I.

Optical	Wavelengths [nm]					
constants	500	600	700	800	900	1000
SiO_4 core-organic refractory mantle						
Q_{scat}	1.54453	1.52593	1.51504	1.50909	1.50849	1.51667
Q_{abs}	1.08172	1.09522	1.10357	1.10932	1.11305	1.11154
Q_{ext}	2.62625	2.62115	2.61861	2.61841	2.62153	2.62821

Table 3.3: These are the optical constants of silicate core-organic refractory mantle particles at the VISCCD wavelengths. For the silicate component, the refractive indices for astronomical silicates Type I is applied. The particle size distribution of Hanner *et al.* (1985) is taken with $a_p = 0.54$ μm.

The efficiencies of the silicate core-organic refractory mantle particles are closer to the efficiencies of the pure organic refractory particles than to the pure silicate particles. Also the absorption efficiency increases with wavelength which leads to a decrease of the scattering efficiency.

The phase function for core-mantle particles considering only the mantle component to be responsible for the external reflection component is similar to the phase function of particles which includes both component, core and mantle, in the external reflection calculation (Figure 3.4).

The silicate core-amorphous carbon mantle particles efficiencies are also lower than the efficiency of the pure silicate particles. Like the core-mantle particles with an organic refractory shell, the carbon mantle grains show the same dependency at visible wavelengths, indicating the higher influence of the shell component on the optical properties. However the silicate core-carbon mantle particles have stronger scattering and extinction efficiencies compared with the particles with an organic refractory mantle (Table 3.4). On the other hand they
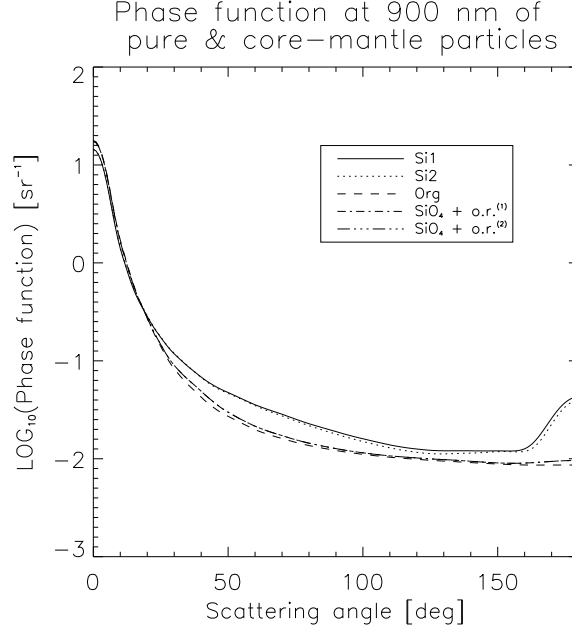
Figure 3.4: The phase functions for the pure silicate, pure organic and silicate core-organic refractory mantle particles. The label [1] and [2] of the core-mantle particles refer to the different refractive indices used to calculate the external reflection component. [1] designate the case using the refractive index of the organic refractory mantle. [2] refer to the case of applying a combined refractive index.

absorb less than the organic refractory mantle particles.

As expected the phase function of the silicate core-carbon mantle particles show similar behavior to that of the organic shell particles (Figure 3.5). As an example for the core-mantle particles, the phase function of the silicate core-carbon mantle particles are plotted between $\lambda = 500$ nm - 1000 nm in Figure 3.4. For scattering angles, $\theta_s > 90°$, the functions are flat and similar and increase with decreasing scattering angles. For 500 nm the strongest forward scattering, $\theta_s = 0°$, has been obtained. In comparison does the phase function at 1000 nm show

Optical constants	Wavelengths [nm]					
	500	600	700	800	900	1000
SiO_4 core-amorphous carbon mantle						
Q_{scat}	1.58786	1.56646	1.54588	1.52929	1.51800	1.51439
Q_{abs}	1.03649	1.04996	1.06474	1.07921	1.09318	1.10446
Q_{ext}	2.62435	2.61642	2.61062	2.60850	2.61118	2.61885

Table 3.4: Optical constants of silicate core-carbon mantle particles at 500 - 1000 nm.

a higher backscattering peak. The phase functions for the silicate core-organic refractory mantle particles show the same characteristics.
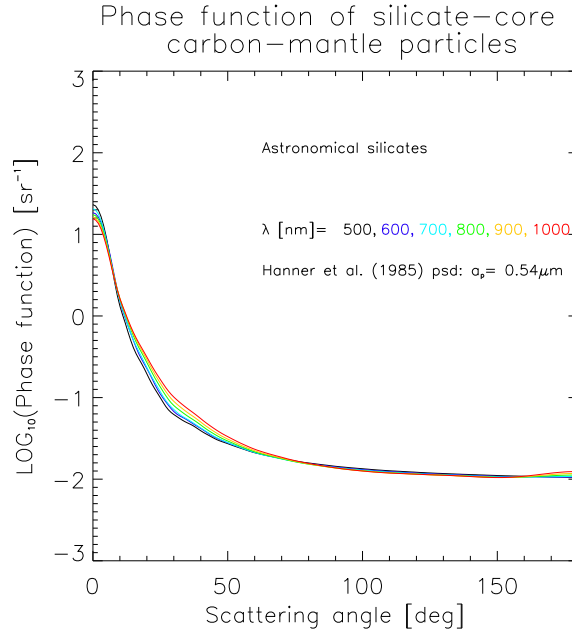
Figure 3.5: The phase functions of the silicate core-carbon mantle particles at 500 - 1000 nm.

Summarized it has been observed that the mantle component is more dominant in the scattering processes for core-mantle particles, which have a core to shell radius ratio of 0.68.

Mixed 2-component particles

The scattering properties of the grains which are made by a mixture of silicate and organic refractory components are presented in Table 3.5. The effective refractive indices for the mixtures were obtained using the Maxwell-Garnett function (Equation 3.28), and has been calculated for ratios of silicate to organic refractory of 1:1 and 2:1. The same calculations has been made for a mixture of silicate and carbon particles (see Appendix).

To calculate the resulting refractive index with the Maxwell-Garnett function, one component has to form the matrix element and the other component the inclusion. For an equivalent mass relation of (1:1), the component with the lower density will comprise a higher volume. This is taken as matrix element. Therefore the organic refractory or the amorphous carbon builds the matrix for the (1:1) mixture. The volume of the silicate and the organics/carbon are comparable for the (2:1) mixture. Thus both, silicate or the organics/carbon, can be considered

matrix element.

The scattering efficiencies decrease with wavelength whereas the absorption and extinction efficiencies increase, following the behavior of the organic contribution. This is similar to the core-mantle grains. The extinction efficiencies of the mixed two component particles do not differ much from the core-mantle particles. But the more pronounced differences lie in the scattering and absorption behaviors. The core-mantle particles scatter more and absorb less than the mixed component particles. The scattering efficiency increases with a higher amount of silicate, whereas the lower amount of organics or carbon results in a lower absorption efficiency. The scattering and extinction efficiencies of both mixtures of silicate and carbon, (1:1) and (2:1), are higher than the one with the organic component. But they show the same dependency on wavelength.

Optical	Wavelengths [nm]					
constants	500	600	700	800	900	1000
Astronomical silicates + organic refractories (1:1)						
Q_{scat}	1.51985	1.50232	1.48967	1.47991	1.47412	1.47494
Q_{abs}	1.10313	1.11873	1.13148	1.14333	1.15350	1.15951
Q_{ext}	2.62298	2.62106	2.62114	2.62324	2.62762	2.63444
Astronomical silicates + Organic refractories (2:1)						
Q_{scat}	1.52899	1.51064	1.49710	1.48528	1.47659	1.47376
Q_{abs}	1.09517	1.11104	1.12415	1.13731	1.14946	1.15809
Q_{ext}	2.62416	2.62168	2.62125	2.62259	2.62605	2.63185

Table 3.5: Optical constants for particles of a silicate and organic refractory mixture at the VISCCD wavelengths. Hanner *et al.*'s (1985) particle size distribution has been applied with a_p= 0.54 μm.

The phase functions for the mixed component particles for the silicate-organic refractory particles of a mixing ratio of (1:1) are presented in Figure 3.6 with silicate as the inclusion and organic refractory as the matrix. This phase functions show similar characteristics to the core-mantle particles. The phase functions of the (2:1) mixing ratio vary depending upon which composition is taken as the matrix. If silicate builds the matrix then the phase function shows a slightly higher backscattering, indicative of the higher silicate influence on the effective phase function. If the organic refractory is chosen to be the matrix element, then no backscattering peak is seen.

In summary the resulting efficiencies and phase functions of the two component particles, which consist of silicate and organic refractory/carbon, are dominated by the contribution of the latter components.
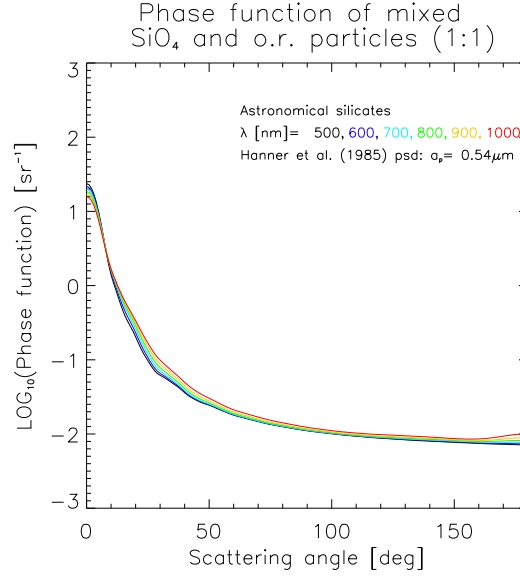
Figure 3.6: The phase functions for mixed silicate-organic refractory particles with a ratio of (1:1) at wavelength 500 nm (black), 600 nm (dark blue), 700 nm (light blue), 800 nm (green), 900 nm (yellow), 1000 nm (red) to the scattering angle.

Geometric Albedo

The geometric albedo, p, has been calculated according to Equation 3.4. Apart from the geometric albedo of the pure silicate grains, the values do not differ strongly from the widely assumed value of $p = 0.03$ for dust in a cometary coma (Divine *et al.*, 1985). The geometric albedo of grains which contain carbon is higher than those for organic refractory containing material. This is expected as the scattering efficiencies of the particles with amorphous carbon are higher.

Dust composition	Wavelengths [nm]					
	500	600	700	800	900	1000
Silicate	0.144	0.182	0.210	0.232	0.246	0.2560
Organic refractory	0.037	0.038	0.039	0.039	0.040	0.042
SiO_4-core & o.r.-mantle	0.038	0.038	0.040	0.042	0.045	0.051
SiO_4-core & C-mantle	0.049	0.049	0.049	0.051	0.053	0.055
SiO_4 and o.r. (1:1)	0.033	0.034	0.035	0.037	0.039	0.043
SiO_4 and o.r. (2:1)	0.034	0.035	0.036	0.037	0.039	0.042
SiO_4 and C (1:1)	0.043	0.042	0.043	0.044	0.045	0.046
SiO_4 and C (2:1)	0.045	0.044	0.044	0.044	0.044	0.045

Table 3.6: Geometric albedo p of different dust compositions at 500 - 1000 nm.

Thomas and Keller (1991) derived from the HMC observations of Halley an $A_p = 0.080$ for a scattering angle of $73°$ (as most of the images were taken at $\approx 103°$ phase angle). This quantity is defined as

$$A_p = \frac{p\Phi_s}{\Phi_\pi} \tag{3.32}$$

where p is the geometric albedo. Φ_s and Φ_π are the scattering functions evaluated when the dust is observed under the scattering angle, θ, and in the anti-solar direction, respectively.

In consideration of the HMC observation, an $A_p \simeq 0.133$ has been obtained for pure silicate grains, and for pure organic refractory grains $A_p \simeq 0.0675$. A_p ranges between 0.060 and 0.080 for core-mantle and mixed 2-component particles. It is noted that the above calculated values have been derived for a size distribution of Hanner *et al.* (1985). For Halley's size distribution determined by Vega and Giotto (Fig. 3.1), A_p is expected to change, but probably not significantly. However, it can be said that the value determined by Thomas and Keller indicates particles composed of organic refractory, silicate-organic or silicate-carbon.

3.4.4   Optical Parameters for the Pik Terskol Data

The optical constants for the Pik Terskol data set have been derived in the same way as those for the VISCCD observations. Because the wavelength range of the Pik Terskol data are comparable to that of the VISCCD, similar behavior and properties are expected for the efficiencies and phase functions. The optical constants of the particles composed of pure silicates and silicate core-amorphous carbon mantle are presented in Table 3.7.

Optical	Wavelengths [nm]			
constants	443.5	525.5	630.8	641.6
Astronomical silicates (Type I)				
Q_{scat}	1.77555	1.77982	1.78966	1.79102
Q_{abs}	0.90297	0.89320	0.88042	0.87910
Q_{ext}	2.67852	2.67302	2.67007	2.67012
SiO_4 core-C mantle				
Q_{scat}	1.61378	1.59449	1.57325	1.57100
Q_{abs}	1.02514	1.03798	1.05162	1.05319 5
Q_{ext}	2.63892	2.63247	2.62487	2.62420

Table 3.7: The optical constants of pure silicate and core-mantle particles at the wavelengths of the Pik Terskol filters. The particle size distribution of Hanner *et al.* (1985) has been applied with a peak radius of $a_p = 0.54$ μm.

The scattering and extinction efficiencies are necessary to obtain the solar radiation pressure acting on the dust grains in the outer dust coma (at distance > 1000 km) and for the analysis of the surface brightness of the dust coma.

Chapter 4

MICAS-Deep Space 1

Remote observations of a comet by spacecraft resolve the active nucleus and its activity. Only in these in situ images the size, volume, structure, shape, albedo and morphology of a cometary nucleus can be derived. Active regions distributed over the nucleus surface and jet-like dust emissions have been observed at comet 1P/Halley and 19P/Borrelly from HMC and MICAS, respectively.

This chapter presents the analysis of the data of comet 19P/Borrelly obtained by the MICAS experiment. The first section contains insight into the observed dust emission features. The dust outflow behavior has been investigated and compared with comet 1P/Halley. The comets show different outflow characteristics. How these differences can arise will be discussed by deducing the dust production rate, examining the radial outflow at different emission angles and analyzing the optical depth of both comets.

4.1 Borrelly's Inner Dust Coma Morphology

The MICAS images of comet Borrelly reveal a coma in the vicinity of its nucleus (20 - 30 km) dominated by jets and fans emanating from its surface. In particular a major collimated dust emission on the sunward side of the nucleus was observed. A first look at the brightness distribution around the nucleus can provide information about the positions, dimensions and shapes of these emission features.

4.1.1 Dust Emission Features

On all MICAS images, a strong non-isotropic emission on the sunward side of the nucleus is observed (Fig. 4.1). The characteristic emission asymmetry of Borrelly, which have been seen over $\sim$ 100 years of observations (see Chapter 2), is presumed to be responsible for the elongation of the coma towards the Sun (Sekanina, 1979; Fulle *et al.*, 1997). This appearance can be clearly recognized

in Figure 4.2 and is even more clear when one plots the azimuthal intensity distribution around Borrelly's nucleus (Figure 4.3).

Figure 4.1: This image is mid_3.2 acquired by MICAS seven minutes before closest approach. The distance of the spacecraft to the nucleus is 7150 km, 1 pixel is equivalent to $\approx$ 0.093 km in projection. The field of view is $\approx$ 50 x 50 km. The nucleus was deliberately saturated to enhance visually the dust emission. The black stripes indicate saturated data. The picture presented here has been processed to make the non-isotropic nature of the emission stand out.

Resolved, this asymmetry consists of a narrow dust jet emanating from the broad central basin on the nucleus. The high-resolution images show that the main features in Borrelly's near-nucleus coma are divided into collimated jets and fans. Especially the main jet on the sunward side is composed of two parts; the α jet, canted about $30°$ from the comet Sun line and the β jet, one of several roughly parallel smaller collimated jets containing in the main jet but offset in the images $\sim 15°$ from the direction of the α jet (Soderblom *et al.*, 2002).

To analyze the dust ejection close to the nucleus, a fit using three Gaussians (plus constant) has been made to the azimuthal brightness distribution following Reitsema *et al.* (1989). Because of the superposition of the α and β jets, one can not resolve them in this type of plot because they are merged to form the one "main jet". The full width half maximum (FWHM) of the observed emission features were determined by fitting. The resulting parameters of the fit are listed in Table 4.1.

The Gaussian representing the main jet on the dayside appears narrow and col-
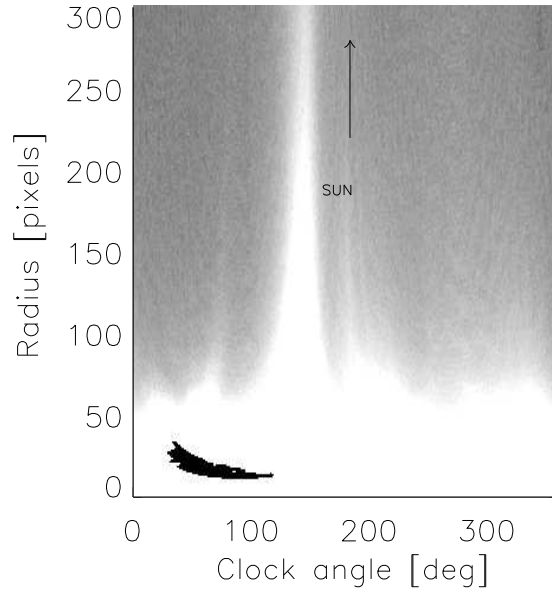
Figure 4.2: This image shows the polar projection about the nucleus center. The Sun direction is indicated by the arrow. Several linear features (jets) can be seen.

limated superimposed over a broader emission. Despite the fact that it is the most dominant feature seen on the images, its contribution to the total emission is relatively low (see Table 4.1). Because of the uncertainty of the background level in the analysis, we also present the relative strengths of the jets compared with the total emission of all jets. The ratio of the projected dayside to night-side emission is estimated to be 3.3 ± 1.0 : 1. The amount of dust over the nightside or anti sunward side is surprisingly high although the features on the dayside seem to be so dominant on the images. This does not, however, imply necessarily nightside activity. Hydrodynamical expansion of the gas which drags dust particles from the sunward-facing active regions across the projection of the terminator could explain these observations (Keller and Thomas, 1989 & Knollenberg, 1994). A dayside : nightside asymmetry ratio of 3.2 :1 was observed at Halley from a similar phase angle.

Emission	Clock angle on image [°]	FWHM [°]	Contribution to total emission (%)	Contribution to total jet emission (%)
Jet1	142	18	19	24
Jet2	177	72	31	40
Jet3	292	74	28	36
Constant	-	-	23	-

Table 4.1: This table summarizes the results of the azimuthal intensity distribution fit. The Sun's clock angle is approximately 177°

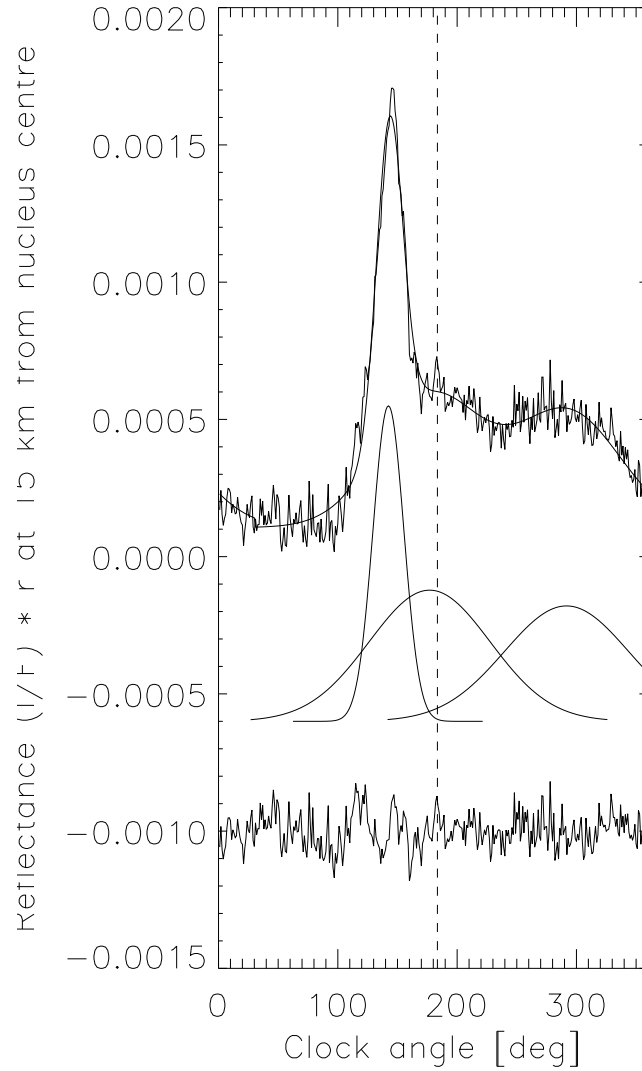Figure 4.3: This plot shows the azimuth brightness distribution at 15 km above the assumed nucleus center of Borrelly (mid_3.2) and the fitted Gaussians. The fit parameters are presented in Table 4.1. The lowest plot represents the residual. The fitted Gaussian and the residual have been offset by -6 x 10^{-4} and -1 x 10^{-3} respectively for clarity. The direction of the Sun is indicated by a dashed line.

4.1.2   Jet Dimension

Because of the elongated shape of the nucleus (roughly 4 km x 8 km in projection) the images have been transformed into a coordinate system based upon an ellipse centred on the nucleus. Figure 4.4 shows the intensity profile on a minimum size ellipse surrounding the nucleus but without intersecting it. This plot has been fitted with four Gaussians to obtain an objective measure of the width of the observed jets near their bases. The width for the main jet on the sunward side of the nucleus seen in MICAS images has a FWHM of about 3.07 km. The FWHM of the emission on the night side is 3.11 km. That of the weaker dust fans is around 0.51 and 0.93 km. These values probably comprise an upper limit to the actual width of the emitting region, because of the rapid lateral expansion immediately above the source. In this plot four emission features are identified while Figure 4.3 shows only three. The reason is that the fan 2 diverges at higher altitude and becomes too faint to fit.
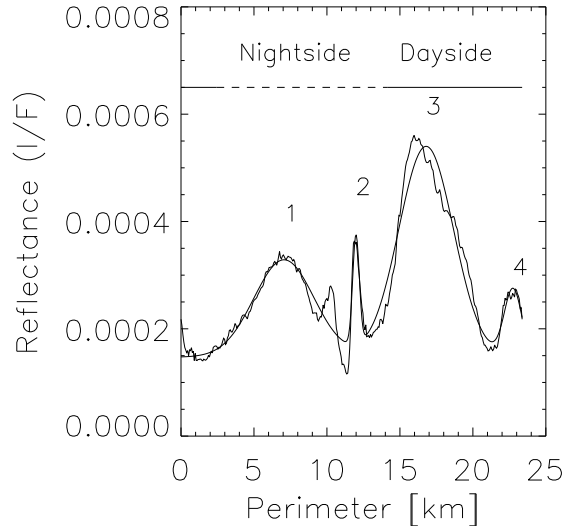
Figure 4.4: This plot shows the intensity along an ellipse surrounding the nucleus. The projected day- and nightside hemispheres are marked. A fit to the data has been superimposed. The emission features are numbered. The ellipse has a major axis of 4.9 km.

4.2   Dust Coma Structure

The simplest model for the structure of a dust coma around the nucleus is described by a point source with a gas production rate of Q_g, gas molecules per unit time, and dust production rate Q_d, dust particles per unit time. It can be assumed that the gas is emitted isotropically and hence its density decreases as $\sim R^{-2}$, where R is the radial distance from the nucleus. Since the motion of the

dust grains is coupled in the region closed to the nucleus surface (gas-dust interaction region), the dust density should therefore decreases in the same manner. The number density of dust particles, n_d, at the distance r from the nucleus is then given by

$$n_d(r) = \frac{Q_d}{4\pi r^2 v_d} \qquad (4.1)$$

where v_d denotes the dust velocity.

The above given assumption is only true in the case of force free outflow, i.e. without acceleration. These conditions are achieved at distances > 300 km away from the nucleus (Gombosi et $al.$, 1986). But this assumption is often still applied for the analysis of in $situ$ data because any deviation from it indicates other forces influencing this "ideal" outflow. The column density is then obtained by integrating along the line of sight, s, at distance ρ from the center,

$$N_d(\rho) = \int_{-\infty}^{\infty} \frac{Q_d}{4\pi r^2 v_d} ds = \frac{Q_d}{4\rho v_d} \qquad (4.2)$$

where $r^2 = \rho^2 + s^2$. ρ is often called the "impact parameter". Figure 4.5 describes the observation geometry between an observer (here: MICAS), the cometary nucleus and the observed dust column along the line of sight. The surface brightness distribution of a coma can be obtained (see Equation 4.10) with $N_d(\rho)$ and the scattering efficiency of the dust particles.

Thus if there are no further effects acting on the assumed outflow above and force free radial outflow is taking place in the coma, the observed column intensity should decrease with $1/\rho$ for increasing distance from the nucleus (this characteristic is often also called the $1/r$ behavior, whereby r is the impact parameter).

It is clear that for near-nucleus observations the nucleus can not be described by a point source with an isotropic dust outflow. The real case deals with a several km sized body with distributed active sources situated on its surface. Thus deviations from the "ideal" $(1/\rho)$ behavior are to be expected.

4.2.1   Dust Outflow

To examine the dust outflow of the comet the projection of the nucleus is approximated as an ellipse and it is assumed that the gas/dust sources are situated on the surface of this ellipse. Further a continuous constant emission of dust should be produced from these sources. If this outgassing expands radially without being
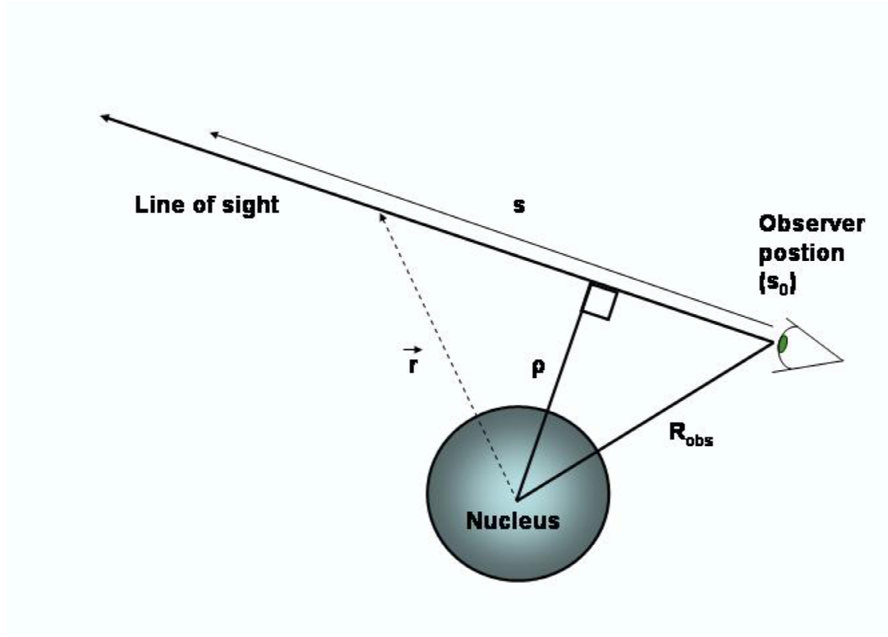
Figure 4.5: This scheme explains the observational geometry between an observer, the cometary nucleus and the dust column density along the line of sight seen from the observer. The line of sight is parameterized by the distance of the closest approach to the nucleus ρ, which is often also called impact parameter. The observer has distance R_{obs} from the nucleus center. The viewing direction is in direction of increasing s.

influenced by any forces, then the dust flux in concentric envelopes remains constant. If the intensity, I, is integrated along the surface of equidistant envelopes around the nucleus (see Figure 4.6), the quantity $\oint I ds$ (where s represents the distance around the perimeter of the envelope) should be constant with increasing radial distance to the nucleus surface for free radial dust outflow. It is hereby referred to Gauss' theorem (Jackson, 1998) of a flux through a closed surface

$$\int E \cdot ds = constant \tag{4.3}$$

where E denotes the dust flux and ds the surface element. This integral will provide information of the source strength. The azimuthal average of the intensity can be related to the flux if the flux is radial.

$$\int E \cdot ds = K \int_0^{2\pi} I \cdot z d\psi \tag{4.4}$$

By replacing ds with $z d\psi$, the polar coordinate form of Equation 4.3 is obtained with ψ denoting the polar angle. I is the intensity and K is a constant. Equation 4.4 is an integral over the circumference of a cylinder. z is the radius of the

cylinder and $d\psi$ the polar angle element. Thus a variation of this integral will indicate sources, sinks, or changes in the scattering or flow characteristics of the dust (Thomas and Keller, 1990).
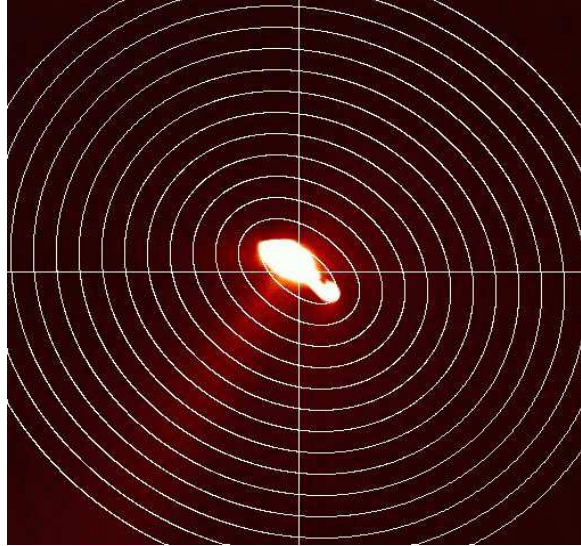

Figure 4.6: The innermost ellipse on this image represents the surface with the active areas on it. The equidistant envelopes are drawn around this ellipse.

This method has been applied to analyze and compare the dust outflow behavior of comets Borrelly and Halley. Borrelly's integral, $\oint I ds$, increased with decreasing distance to the nucleus surface, while Halley's decreased (see Figure 4.7). One can interpret this in terms of deviations from a $1/\rho$ dependence of intensity. Halley's intensity profile flattens close to the nucleus (Thomas *et al.*, 1988); Borrelly's steepens.

There are several possible explanations for this observation. A high optical depth above active regions can flatten $1/\rho$ profiles close to the nucleus and would be a plausible explanation for Halley. Also fragmentation into optically "large" particles can cause similar behavior of the intensity because of the change in the scattering area at visible wavelengths (Thomas *et al.*, 1988). Earlier observations of Halley have detected a high amount of large dust particles (Fulle *et al.*, 2000), thus this fragmentation process is possible. In Borrelly's case, particles fragmentating into submicron size would explain a decrease of the integral with distance. These particles would not contribute to the scattering process at large distances and the intensity will drop. Soderblom *et al.* (2002) also suggested that Borrelly's dust particles seem to be small. Another potential reason for Borrelly's behavior is dust acceleration which steepens the intensity profile near the nucleus, because of the increasing dust number density. Also the existence of distributed sources on the nucleus surface might influence the intensity profile.
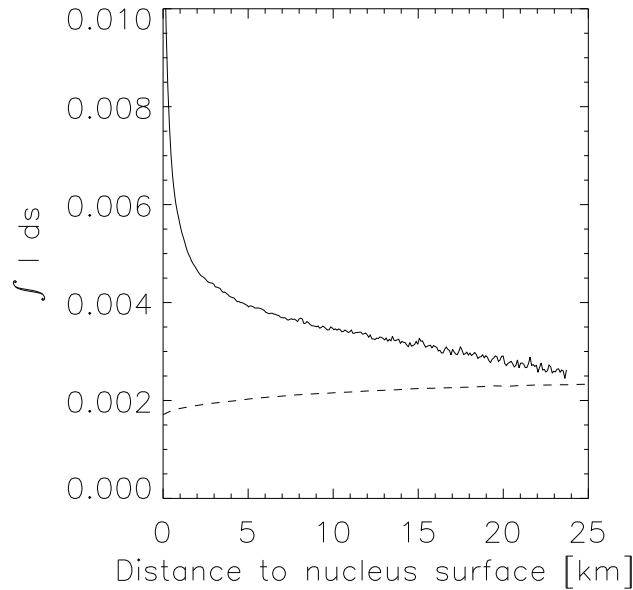
Figure 4.7: The integrated intensity along equidistant envelopes is plotted for Halley (- - -) and Borrelly (——). Halley's integral, $\oint Ids$, has been divided by 48 which also gives a 0th order estimate of the ratio of the dust production rates.

4.2.2 Dust to Gas Ratio

Comet Halley's integrated intensity $\oint Ids$ has been divided by 48 in Figure 4.7, which is approximately the ratio of the dust emission brightness at large cometocentric distances. Models by Gombosi *et al.* (1986) indicated dust velocities for Halley to be $v_{Halley} \approx 200$ m/s, and Borrelly to be $v_{Borrelly} \approx 120$ m/s for micron-sized particles. This means that Halley's dust velocities are approximately $\frac{5}{3}$ times higher than Borrelly's. Therefore the dust production rate ratio must be higher than the observed brightness ratio with values around 80:1 being possible.

The H_2O production rate of Borrelly at DS1 encounter was 3.5×10^{28} molecules/s (Stern *et al.*, 2003). That of Halley at Giotto encounter was 5.2×10^{29} molecules/s (Festou *et al.*, 1986). Thus the water production rate of Halley was approximately 15 times higher that of Borrelly. If it is assumed that the water production rate is approximately equal to the total gas production rate, the dust to gas production rate (χ) of both comets can be derived. By assuming that the dust size distribution for the two comets were comparable and by taking into account the above derived dust production rate ratio (80:1), it can be concluded that the dust to gas ratio of Halley was about five times that of Borrelly.

McDonnell *et al.* (1990) gave a dust to gas ratio for Halley of 2 at the nucleus

and hence that for Borrelly will be $\chi = 0.4$. A'Hearn *et al.* (1995) gave $\chi = 1.16$ for Borrelly (assuming that an $Af\rho$ of 1000 cm is roughly the dust production rate in metric tons/s). Their value for Halley was 1.6.

4.2.3   Radial Profile of Dust Outflow

In this section the radial profile of the brightness will be examined more closely, by looking if the profiles along different directions from the nucleus center changes. Figure 4.8 shows the two directions which are relevant for the analysis. The profiles along the main jet, the profile on the anti sunward side and the averaged profile over all 2π directions.
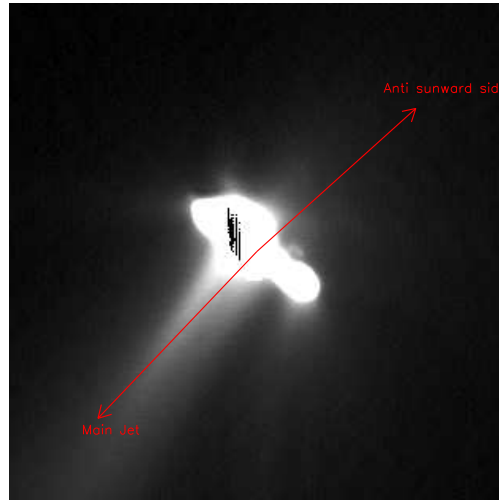
Figure 4.8: This plot gives the direction examined in the radial profile. The direction along the main jet and the nightside are indicated by the arrows.

This approach is based on the first order assumption that the nucleus is a point source with an isotropic dust outflow (Equation 4.1). Thus the observed column density has to decrease with increasing distance to the nucleus center, i.e. with $1/r$ (Equation 4.2).

The integrated intensity method, described in the previous section, examines the dust flux in an enclosed surface, and thus gives an average description of the outflow within the enclosed space. By examining the radial profile along different emission directions, the reason for the $1/r$ deviation observed in the integrated intensity method will be better localized.

Figure 4.9 show representative plots of the radial profiles for the VISCCD data sets; mid_1.2 (range of DS1 to Borrelly, $\Delta \simeq 82951$ km, and phase angle, $\alpha \simeq$

92°), mid_3.2 ($\Delta \simeq 7156$ km and $\alpha \simeq 71^{\circ}$), mid_4.2 image ($\Delta \simeq 6216$ km and $\alpha \simeq 68.7^{\circ}$) and mid_5.4 image ($\Delta \approx 4025$ km and $\alpha \simeq 56^{\circ}$). The radial profile has been multiplied by the distance to the nucleus center, ρ. It should be noted the first 4 km away from the center is taken by the nucleus body itself.

None of the averaged radial profiles follow strictly the $1/r$ behavior. The averaged radial profiles of the mid-images show all the same characteristics. They decrease with increasing distance from the nucleus (as do the integrated intensity along equidistance envelopes seen in the previous section). But if one analyzes the profiles separately, two different types of profile can be recognized.

The (I/F) profiles along the main jet increase in the first 3 km away from the nucleus surface and reach a constant value. On the closer images, mid_4.2 and mid_5.4 a slight increase of the curve is seen (probably because of noise).

Boice *et al.* (2002) has also investigated the radial intensity profile of Borrelly along the main jet and the fans. They concluded that the flattening of the intensity radial profile along the main jet with decreasing distance to the nucleus is explained with an extended active source.

The radial profile on the anti-sunward side decreases in all mid images out to the edge of the image. The flat section within the first 3 km should be ignored, because this is a contamination of light from the nucleus. If one examines the radial profile along the two fans observed at the upper and lower limb of the nucleus, they show the same behavior. Thus one can conclude that the deviation from the $(1/r)$ behavior in the integrated intensity is mainly because of the non-$1/r$ feature on the anti sunward side and the fans. The actual main jet follows the $(1/r)$ behavior at distances between 10 - 40 km away from the center.

Summarizing the discussion above about observed radial intensity profiles, it seems difficult to explain the night side dust with emission on the anti sunward side. This leads to the idea of hydrodynamical gas expansion dragging the dust particle onto the night side. Another explanation would be dust jets which are ejected not perpendicular to the line of sight but towards the observer (MICAS). This would also explain the strong intensity decrease of the night side and along the fans which together covers a bigger area than the actual main jet. Therefore the averaged intensity decreases.

4.3 Dust Activity

The dust activity of a comet can be measured in terms of a quantity, $Af\rho$. Consider the ratio of the coma intensity to the mean solar disk intensity, $i_{coma}/i_{\odot}$. The product of geometric albedo p, the phase function $\Phi(\alpha)$, and the local filling
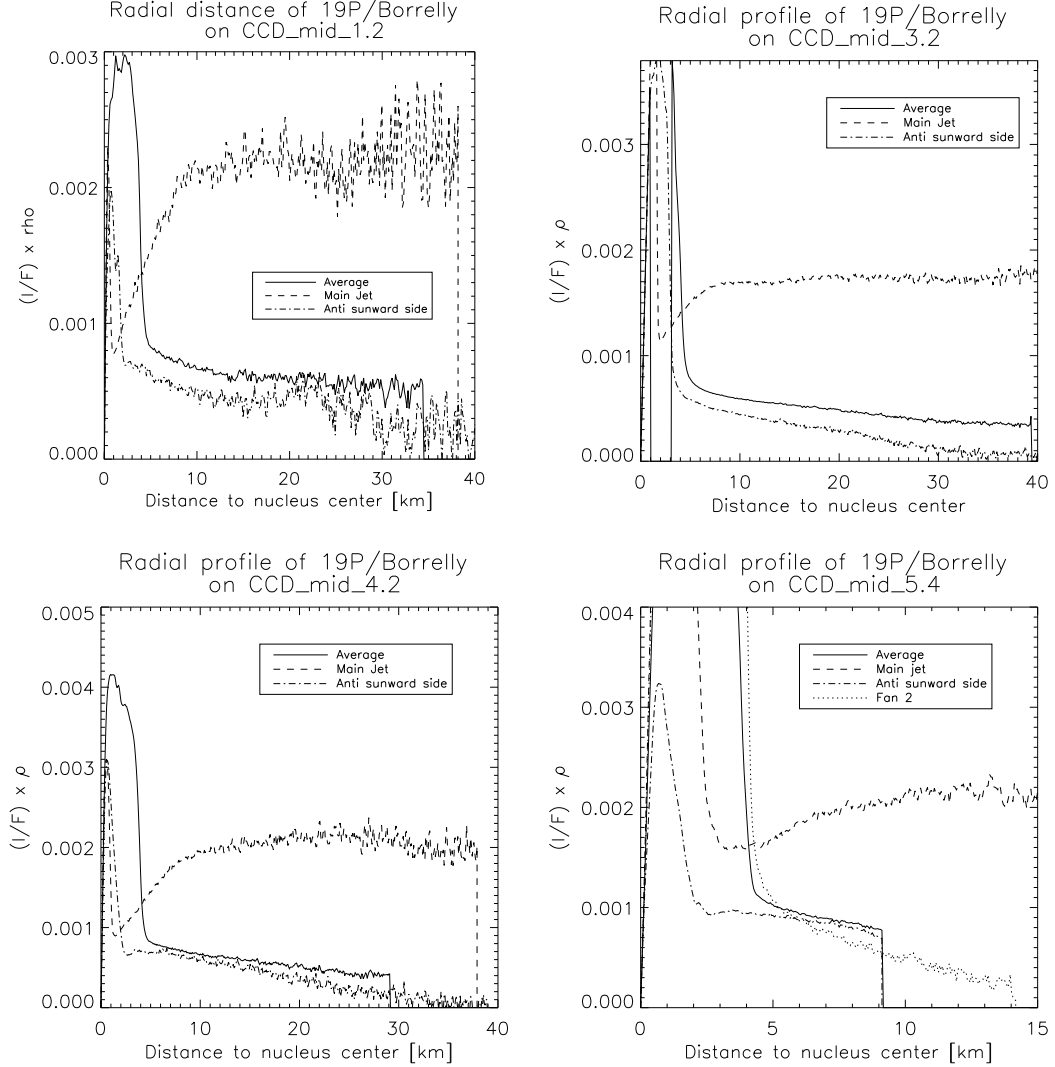
Figure 4.9: The I/F radial profile $\times\rho$ of the dust coma on the mid_1_2, mid_1_3, mid_4.2 and mid_5.4 images with increasing distance to the nucleus center. The averaged radial profile (——) has been obtained by averaging the I/F over the total azimuth (2π). The jet radial profile (- - -) considers the intensity along the main jet, whereby the intensity has been binned over an angle of $20°$. This match with its FWHM listed in Table 4.1. The radial profile of the anti sunward side $(- - -)$ is obtained from the intensity seen on the opposite side of the main jet, whereby the intensity is binned over an angle of $76°$, see Table 4.1. The nucleus body has an extension of about 4 km.

factor in the coma, f_{coma}, are then defined as

$$p\Phi(\alpha)f_{coma} = \frac{i_{coma}}{i_\odot}\left(\frac{r_h}{R_\odot}\right)^2 \tag{4.5}$$

where r_h is the heliocentric distance of the comet and $R_\odot$ denotes the radius of the Sun (Jockers, 1997). If the particles are emitted isotropically from the nucleus and move radially outward with constant velocity, the intensity in the coma is $\propto \rho^{-1}$, where ρ is the impact parameter. Then the product $p\Phi(\alpha)f_{coma}\rho$ is a constant than can be used as a measure of the dust production rate. The quantity $Af\rho$ introduced by A'Hearn *et al.* (1984) is connected to this product by

$$Af\rho = 8p\Phi(\alpha)f_{coma}\rho \tag{4.6}$$

(Jockers and Bonev, 1997). Figure 4.10 gives the scheme of the geometry described to define the dust activity.
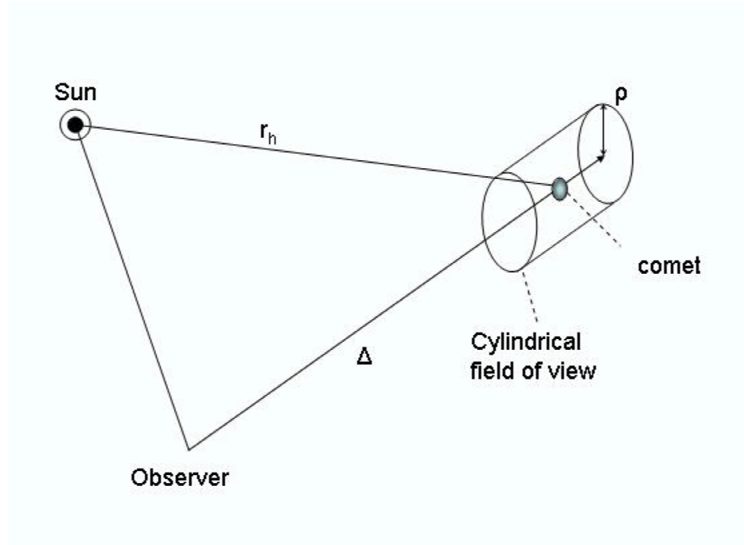
Figure 4.10: This is observation geometry scheme. r_h and Δ denote the heliocentric and observer centered distance of the comet, respectively. If the observer centered distance is large compared with the observed coma (which is true for Earth-based observations), the field of view can be approximated by a cylinder with radius ρ centered around the comet. This assumption is also applied for *in situ* observations to determine the observed column density, although the distance to the nucleus is commonly ranging between $1 \cdot 10^5$ until down to 5000 km (MICAS data).

Although the $Af\rho$ quantity is usually used for the evaluation of Earth-based

observations, the validity of its application on *in situ* data sets has been quantitatively examined in the following sections.

4.3.1   Dust Production

Comet Halley's total dust production rate at Giotto encounter has been determined to be $2.17 \cdot 10^4$ kg s^{-1} (Thomas and Keller, 1991). This value has been derived by taking into account the total effective mass of dust (m_{enc}) encountered by Giotto at 596 km away from the nucleus. m_{enc} has been measured by the radio science experiment (GRE). From the HMC images the intensity (I_{enc}) at 596 km could be determined. Thomas and Keller assumed the azimuthal average Z, (Equation 4.4), to be proportional to the column density of dust integrated over a circle at constant impact parameter, (Equation 4.1). Therefore the total production rate, Q_d, can be derived by

$$Q_d = \frac{2\pi Z m_{enc}\langle V\rangle}{I_{enc}\sigma_{s/c}(\langle \Xi \rangle + 1)} \qquad (4.7)$$

where $\langle V \rangle$ is the mean velocity of the particles perpendicular to the line of sight, ($\langle \Xi \rangle$) refer to the weighted mean momentum enhancement factor and $\sigma_{s/c}$ is the cross-sectional area of the spacecraft (2.88 m^2). $\langle V \rangle$ can be computed from the estimates of the terminal velocities of the particles (e.g. Gombosi *et al.*, 1986) and their size distribution along the line of sight.

As has been mentioned before, the dust production rate of a comet can also be explained by the $Af\rho$ value. To get a direct comparison, as the dust production rate of comet Halley is known, and to examine if one can also apply this parameter for *in situ* data sets as well, the $Af\rho$ value of Halley has been determined. Figure 4.11 gives the $Af\rho$ values of Halley within the first 40 km away from the nucleus. Image 3416, taken at a distance of $2.56 \cdot 10^5$ km, has been used. Figure 4.12 shows the $Af\rho$ values derived from image 1586 (clear filter at CA-128 min from $5.25 \cdot 10^5$ km) taken with the HMC. The $Af\rho$ values of Halley on image 3416 increase steadily without reaching a constant value in the first 40 km away from the nucleus. However, a constant value of $\approx 1.8 \cdot 10^4$ cm between 100 - 600 km away from the nucleus can be observed for the $Af\rho$ value obtained from the 1586 image (Fig. 4.12). Beyond 600 km the $Af\rho$ increases to a value of $2.0 \cdot 10^4$ cm, indicating an increasing intensity because of the increasing influence of gas molecules within the HMC broad-band clear filter (Thomas and Keller, 1990). Those are daughter products created through photodissociation and photoionisation of parent molecules. The contribution of the nucleus to this value is negligibly small ($< 1\%$).

With the crude assumption that the value of $Af\rho$ of about 1000 cm is roughly equal to the value of the production of dust in metric tons per second (A'Hearn
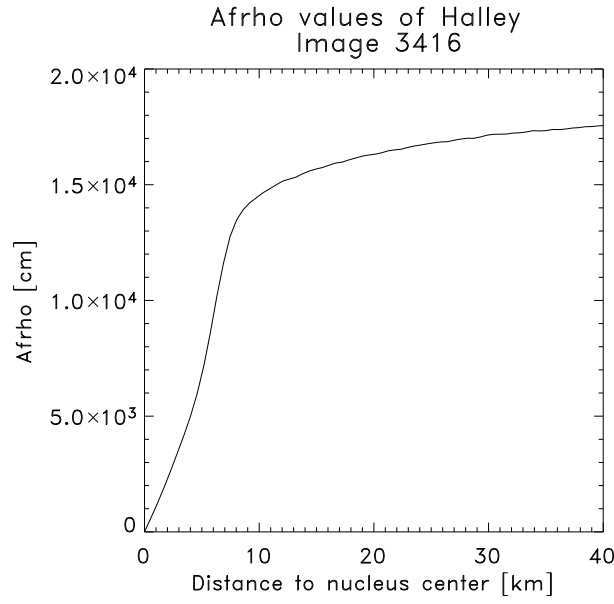
Figure 4.11: $Af\rho$ values of comet Halley (image 3416) until 40 km away from the nucleus. The spacecraft was $2.56 \cdot 10^5$ km away from the nucleus. The phase angle $= 105.9°$.
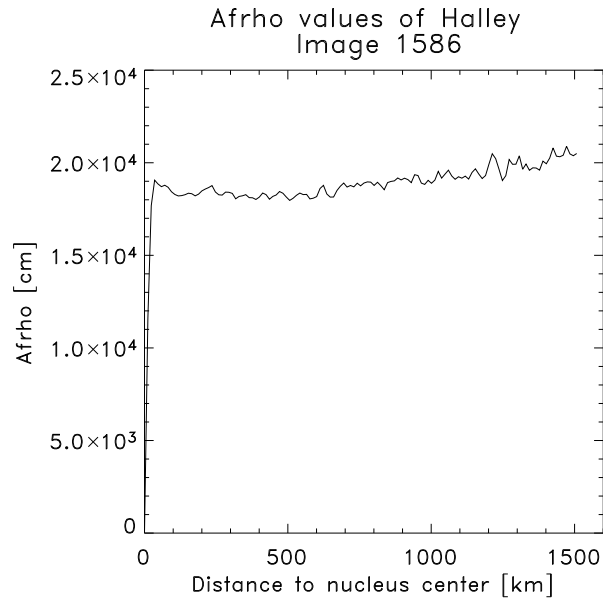

Figure 4.12: $Af\rho$ values of comet Halley (image 1586) until 1500 km away from the nucleus. The spacecraft was $5.25 \cdot 10^5$ km away from the nucleus. The phase angle $= 107°$.

et al., 1995), a total dust production of $1.8 \cdot 10^4$ kg s^{-1} is derived from the $Af\rho$ value at ≈ 600 km away from the nucleus (Figure 4.12). This is about 1.2 less than the value derived by Thomas and Keller (1991).

From narrowband filter photometry of Comet Halley, Schleicher *et al.* (1998) deduced an $Af\rho$ value of $\approx 2.04 \cdot 10^4$ cm in March 14, 1986. This value is about 10% higher than the $Af\rho$ derived from the HMC image. Considering the photometric errors in calibration, this result indicates excellent agreement.

The same procedure has been applied on the images obtained of Borrelly. Figure 4.13 and 4.14 give the $Af\rho$ values for two representative VISCCD images while the spacecraft was approaching the nucleus. The $Af\rho$ values of all "mid" images, which cover the region up to 40 km away from the nucleus, converge to a value between 200 - 250 cm. This is approximately half of the value obtained from the analysis of the Earth observational data sets (400 - 600 cm), which will be seen in section 6.1.4.

Table 4.2 summarized the $Af\rho$ values derived for Borrelly and Halley from the ground-based and the *in situ* observations.

Comet	$Af\rho$ (*in situ*) [cm]	Phase Angle [°]	$Af\rho$ (Earth) [cm]	Phase angle [°]
Halley	$1.8 \cdot 10^4$	107	$2.04 \cdot 10^4$	64.5
Borrelly	200-250	72	400-600	41

Table 4.2: Halley's and Borrelly's $Af\rho$ values derived from the *in situ* and Earth observations. The $Af\rho$ value of Halley observed from the Earth has been taken by the paper of Schleicher *et al.*, 1998. All the other values has been derived in this work. The $Af\rho$ values given for Halley has been derived in March 14, 1986. The values for Borrelly are for September 21, 2001.

It should be noted here that the $Af\rho$ of Halley in the first 40 km away from the nucleus was increasing. Only at distances > 100 km did the $Af\rho$ approaches a constant value. Unfortunately, the "far" images of MICAS could not be used to verify how the $Af\rho$ would change at distances > 100 km away from the nucleus and if an $Af\rho$ derived at such close distance (< 40 km) deviates systematically from the one calculated far away (> 100 km). It is arguable whether this could explain the whole difference between the ground-based and DS1 observation. Another explanation for this difference could be a calibration error.

During the 1981 apparition, at a heliocentric distance of ~ 1.34 AU, Newburn and Spinrad (1989) estimated a dust production rate of about 335 kg/s, assuming a nuclear radius of 3.5 km and an active fraction of 10% whereby a factor 2 error is estimated. Lamy *et al.* (1998) calculated from the HST observations a dust
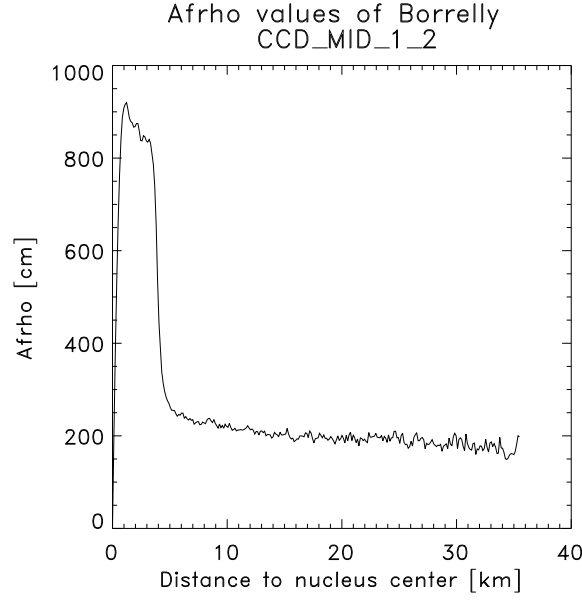
Figure 4.13: The $Af\rho$ values for mid_1.2 image. The spacecraft was $\approx$ 8927 km away from the nucleus and the phase angle $\approx$ 75°.
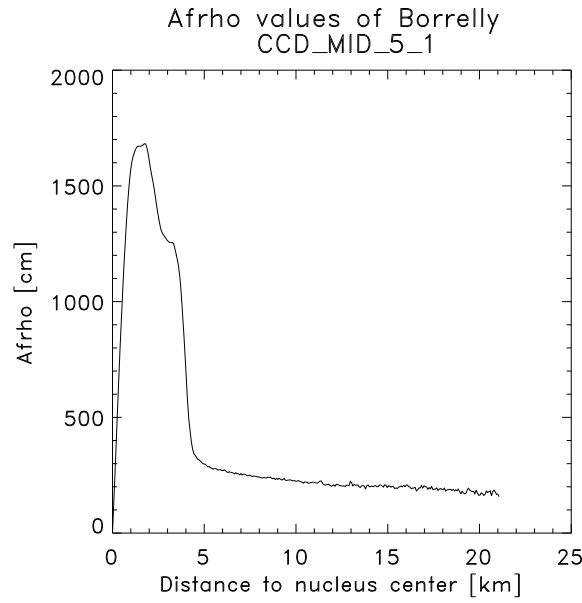
Figure 4.14: The $Af\rho$ values for mid_5.1 image. The spacecraft was $\approx$ 5341 km away from the nucleus and the phase angle $\approx$ 65.1°.

production rate of 180 - 215 kg/s for Borrelly.

4.4 Radiation Environment of the Inner Dust Coma

With the dust production rates received from the data analysis in the previous section and the optical parameters discussed in section 3.4.3 a quantitative interpretation of the observed brightness in the dust comae of comets Borrelly and Halley can be made. There follows an introduction about the radiative transfer by dust particles. Then the results of the brightness calculations for the *in situ* data sets will be presented.

4.4.1 Intensity received from a Line of Sight

To discuss radiative transfer by dust particles unpolarized radiation is assumed. The independent variables are time, position, direction and wavelength λ, of the observation. The major dependent variables are the differential intensity i and the flux j.

To examine the brightness seen in the coma by an observer, one has first to consider an isolated dust particle in sunlight. The solar flux reaching this particle is

$$j_{\odot,\lambda} = \frac{f_{\odot,\lambda}}{r_{hel}} e^{-\tau_\odot} \tag{4.8}$$

$f_\odot$ [W m^{-2}nm^{-1}] is the solar flux per wavelength at 1 AU, which is scaled by the heliocentric distance of the dust grain in [AU], r_{hel}, to get the solar flux reaching the particle. Further this flux is reduced through the optical depth which separate the particle from the Sun, $\tau_\odot$ (Equation 4.12).

The observed differential intensity (Divine *et al.*, 1986) along the line of sight in [Wm$^{-2}\mu$m^{-1}sr^{-1}] is defined as

$$i = \int_0^\infty e^{-\tau} \int_0^\infty n\sigma_{ext} \left[\omega\Phi_s j_\odot + \frac{\varepsilon\sigma T^4 f}{\pi Q_{ext}} + \omega \int_\pi \Phi_s i d\Omega \right] \mathrm{d}a \mathrm{d}s \tag{4.9}$$

whereby n is the local differential dust concentration in [m^{-3} size^{-1}] and σ_{ext} is the extinction cross-section (Eq. 3.1). Equation 4.9 consists of three terms. Term 1, which contains the single scattering albedo, ω, the normalized phase function according to Eq. 3.2, and the solar flux, $j_\odot$, describes the scattering of sunlight

by the dust.

The second term is the radiation term which is dominant in the IR but much less in the visible. ε is the emissivity, T is the local grain temperature in [K], and Q_{ext} denotes the extinction efficiency. The effect of multiple scattering is described by the last term, and can be neglected for a optical thin coma. The optical depth τ describes the power removed from the beam between the observer and the particles. These terms have to be integrated over all particles sizes with the local differential concentration n and over the pathlength s along the line of sight.

The calculations presented herein are applied to visible wavelengths and so term 2 can be ignored. In the case of an optical thin coma, multiple scattering processes will have little effect beyond a few kilometers from the nucleus and thus term 3 can be ignored as well. The total observed intensity along the line of sight is therefore

$$I = \int_{\lambda_1}^{\lambda_2} W_\lambda i d\lambda = \int_{\lambda_1}^{\lambda_2} \int_0^\infty \int_{-\infty}^\infty n\sigma_{ext} A\Phi_s j_\odot da ds d\lambda \qquad (4.10)$$

where the integration limits (λ_1 and λ_2) cover the effective bandwidth of the instrument. The dimensionless weighting function, W_λ, describes the spectral sensitivities of the detector. This is plotted in Figure 2.4 for the VISCCD.

By assuming a radial symmetric coma, n can be described by the number density of dust particles (see Equation 4.1).

Optical Depth

The optical depth between two positions $s1$ and $s2$ is described as the product of the local differential dust concentration, n, and the extinction cross section for all particle sizes along the line of sight

$$\tau = \int_{s1}^{s2} \int_0^\infty n\sigma_x da ds \qquad (4.11)$$

The incident Sun light at a position $\vec{r}$ in the coma is attenuated depending upon the extinction along the path from the Sun to the dust particle's position inside the coma. The optical depth from a particle to the Sun is then

$$\tau_\odot = \int_0^{r_{hel}} \int_0^\infty n(\vec{r}_\odot(s))\sigma_x da ds \qquad (4.12)$$

where $\vec{r}_\odot(s) = \vec{r} + s\vec{e}_\odot$ is the position in solar direction place at distance s from the required point $\vec{r}$ and $\vec{e}_\odot$ is the unit-vector pointing to the Sun.

The optical depth seen from an observer along the line of sight can be derived in the same way, whereby the integration has to be performed along the line of sight of the observer. Figure 4.10 gives a sketch of this geometry.

$$\tau_{obs} = \int_{-\infty}^{s_0} \int_{0}^{\infty} n(\vec{r})\sigma_x da ds \tag{4.13}$$

4.4.2   The Visible Radiation Environment of Borrelly

The intensity received from a dust column along the line of sight of MICAS has been calculated by assuming a total dust production rate of $Q_d \approx 200$ kg/s comparable with the value derived by Lamy *et al.* (1998). The particle size distribution of Borrelly is calculated by Equation 3.25 with a peak radius of a_p = 0.54 μm. The dust density follows the form (Divine *et al.*, 1986)

$$\rho_d = \rho_0 - \sigma_0 \left(\frac{a}{a + a_2} \right) \tag{4.14}$$

varies with grain radius a. For ρ_0 the grain density of the respective components are taken. The grain densities are given in section 3.4.

For the core-mantle particles, the density was found by dividing the total mass with the total volume of the particle. The effective density of a silicate core-organic refractory mantle is $\rho_d = 2196$ kg/m^3; the effective density for a silicate-core carbon-mantle particle is $\rho_d = 2421$ kg/m^3, the densities of the mixed 2-components particles are listed in the Appendix. σ_0 can be scaled according to the assumed porosity. Gombosi *et al.* (1986) suggested a density distribution which gives a porosity of P $\simeq$ 0.73 for mm-size particles, whereby Lamy *et al.*'s (1987) density function gives P = 0.64 for the mentioned size range. A value of 2 μm has been used for a_2. This has been suggested because studies of meteor streams which are connected with comets showed that larger dust grains have lower densities (Divine *et al.*, 1986). By applying this density function, dust grain porosity is considered, which has been determined for Halley's and Borrelly's dust by several authors including Li and Greenberg (1998).

If the volume of the particles is assumed to be equivalent to a sphere, the mass of each dust grain size can be derived. By scaling it with the size distribution, a mass distribution can be found. The differential dust production rate has been obtained by normalizing this mass distribution with the total dust production rate, Q_d.

The velocities of Borrelly's dust grains with a bulk density of 1000 kg/m^3, Fig. 4.15, have been obtained from a 2D-axissymmetric model (assuming a spherical nucleus) for the DS1 encounter period (Combi and Tenishev, 2003). The velocities of the various grain types can be derived by scaling the given velocities in
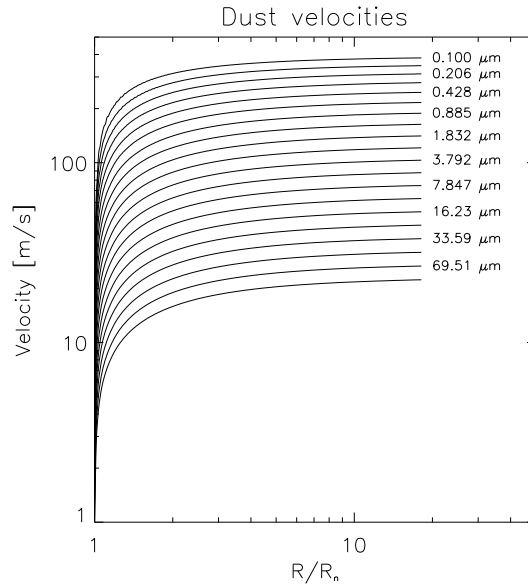
Figure 4.15: The dust velocity of Borrelly for grain radius between 0.1 μm - 100 μm and a bulk density of 1000 kg/m^3. This data has been calculated for the condition at encounter phase of DS1 and comet Borrelly in September 21, 2001 (Combi and Tenishev, 2003).

Figure 4.15 with the bulk densities of the required compositions. By inputting these velocities, dust acceleration is included. The local differential dust concentration n at increasing ρ is then obtained with Equation 4.1 assuming isotropic outflow. Thus the observed total intensity of the coma can be calculated with increasing distance from the nucleus following Equation 4.10. The resulting intensity can be converted to a reflectivity via $\varrho = \pi I / F$.

To model the radiation environment of Borrelly's inner dust coma following the above theoretical approach two values have been used. The assumed total dust production of $Q_d = 200$ kg/s and the averaged porosity of 0.68 from the suggested density functions of Gombosi (1986) and Lamy *et al.* (1987). The reflectivity of the dust coma has been modeled for all the particle compositions presented in Section 3.4.3.

Figure 4.16 presents the observed reflectivity of Borrelly on image mid_3.2 and the modeled values for a dust coma with pure silicate grains. As an isotropic dust outflow is assumed, the resulting reflectivities have to be compared in first instance to the averaged observed one. The best fit to the averaged observed reflectivity has been obtained for particles with porosity of 0.89 and a dust production rate of $Q_d = 200$ kg/s or for particles with P = 0.68 and $Q_d = 350$ kg/s. The resulting reflectivities are strongly dependent on the assumed porosities and dust production rates. However, both results are reasonable.

The reflectance of a dust coma containing core mantle particles is displayed in Figure 4.17 for silicate core-organic refractory mantle particles. To fit the observed reflectivity with a dust production rate of 200 kg/s, the particle densities have to range between $300 \leq \rho_d \leq 2200$ kg/m^3. This is equivalent to a porosity of 0.86. If the porosity of the mm-particle is P $\simeq$ 0.68 then the model has to produce 310 kg/s to fit the observed reflectivity.

By increasing the porosity, i.e. making the bigger particles lighter, a higher velocity will be obtained. One might expect the intensity to be lower. However, the intensity increases slightly. As the particles become lighter, the differential dust production rate will increase to meet the production rate constraint. This results in an increased number of particles, which will scatter more light. Heavier grains, i.e. lower porosity, give then lower observed intensities.

Further it is recognized that the modeled reflectivities are all higher at distances < 10 km to the nucleus surface than the observed one and higher values at distance > 25 km. This can be explained by the fall off on the night side, which can not be modeled with the outflow assuming here.

A remark also has to be made concerning the profiles of the main jet and the anti-sunward side. To be able to fit the observed reflectivity along the main jet, the production rate has to multiplied by a factor of about 2.2. In the case of the nightside, it has to be reduced. But a fit to the nightside profile is difficult to obtain because of the strong fall off.

The observed reflectance curve along the main jet is flatter than the observed one at distance < 5 km away from the nucleus. This can be explained by extended active sources (Boice *et al.*, 2002), which have been discussed in section 4.2.3. At higher distances the modeled curve and the observed one are nearly parallel to each other, indicating similar outflow processes.

The same relation between dust porosity and production rate like the one presented for pure silicate and core-mantle grains has been found for all dust compositions. For a dust production rate of 200 kg/s, the particle's porosity has to range between 0.78 (mixed silicate & organics grains) and 0.89 (pure silicate grains). To fit the observed reflectivity with P = 0.68, a dust production rate between $Q_d = 270$ kg/s (mixed silicate & organics grains) and $Q_d = 350$ kg/s (pure silicate grains) is needed. This would be in reasonable agreement with Q_d = 335 kg/s given by Newburn and Spinrad (1989).
If the dust coma is mainly dominated by core mantle particles (Li and Greenberg, 1997), the dust grains would have a porosity of 0.83 and 0.86 for silicate core-carbon mantle and silicate core-organics mantle grains, respectively. This is comparable with the porosity of P $\simeq$ 0.85 for core-mantle particles suggested by

Figure 4.16: Borrelly's observed (I/F) on mid_3.2 and the results of the brightness calculations. The (I/F) of Borrelly are presented as average over 2π (——), along the main jet (- - -) and on the anti sunward side ($\cdots$). The derived (I/F) for a coma of silicate grains has been calculated for two density and dust production rate. For P = 0.89 and Q_d = 200 kg/s: —— (blue). For P = 0.68 and Q_d = 350 kg/s: —— (red).

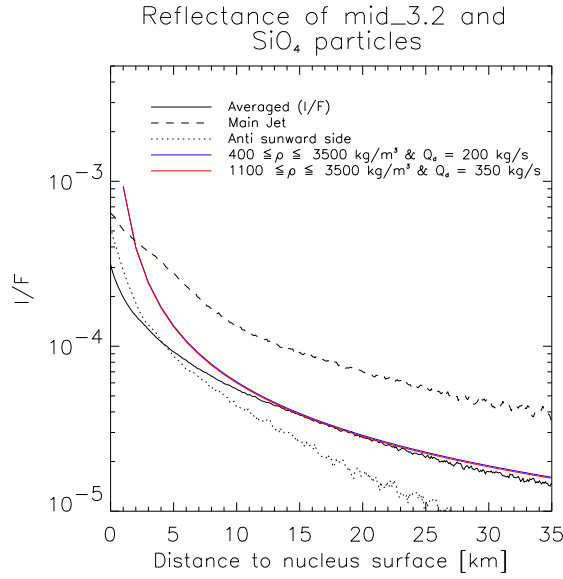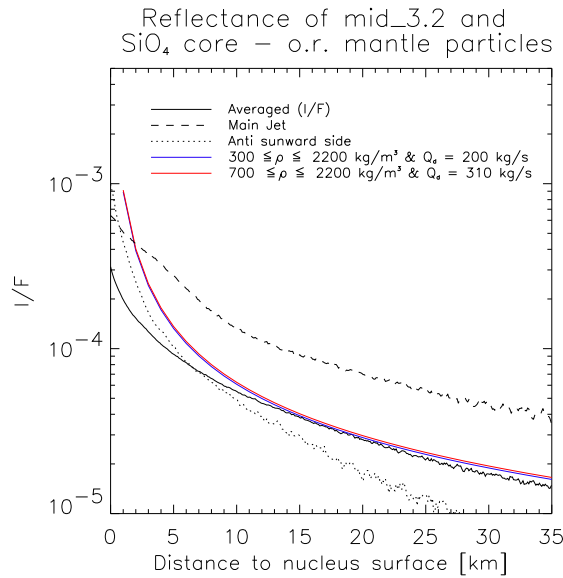Figure 4.17: Borrelly's observed (I/F) on mid_3.2 and the results of the brightness calculations. The (I/F) of Borrelly are presented as average over 2π (——), along the main jet (- - -) and on the anti sunward side ($\cdots$). The derived (I/F) for a coma of silicate core-organic refractory mantle grains has been calculated for P= 0.86 with Q_d = 200 kg/s: —— (blue), and for P = 0.68 with Q_d = 310 kg/s: —— (red).

Li and Greenberg.

To fit the observed reflectivity with P = 0.68, dust production rates about 1.5 times higher than the rates deduced from the *in situ*-$Af\rho$ values are needed. These production rates are between the $Af\rho$ values of the *in situ* and ground based data sets.

To fit the observed reflectivity of Borrelly with a dust production rate comparable to the $Af\rho$ values (400-600 cm) of the Earth observations, i.e. 400 - 600 kg/s, very compact grains with porosities around 0.2 are required. This departs strongly from the fluffy appearance widely assumed for cometary dust grains (Divine *et al.*, 1986).

No precise conclusion about the dust composition could be made from the analysis of the radiation environment because of the uncertainties in porosity and dust production rates. However, it can be said that the conversion of the "Earth"-$Af\rho$ values to kg/s do not give satisfactory fit to the reflectivity of the inner dust coma, unless the particle have a much lower porosity than is widely assumed.

4.4.3 Optical Depth of Borrelly and Halley

The resulting optical depths of the dust coma for Borrelly are presented in Fig. 4.18. The values for the simulations with a dust production rate of about 200 kg/s are plotted versus distance for pure silicate, pure organic refractory, core-mantle and mixed component grains.

All dust comae of the different compositions give an optical depth below 1. The highest optical depth would be obtained with a dust coma composed of silicate core-organic refractory mantle particles. The lowest optical depth value is given by a coma of pure silicate grains. Because the silicate grains are the heaviest among all the compositions, the particle number and thus the effective extinction cross section is lowest. In summary, Borrelly's dust coma can be considered to be optically thin.

Halley's optical thickness is presented in Figure 4.19, using a total dust production rate of $2.17 \cdot 10^4$ kg/s according to the dust production rate discussion in section 4.3.1. The dust coma contains 20% silicate, 40% organic and 40% silicate-organic mixed particles with the contributions determined by the PIA observations. The particles are assumed to have a porosity of $P \approx 0.81$ which is the mean value of the porosity derived by Greenberg and Li (1999), suggested by Lamy *et al.* (1987), and Gombosi (1986). Dust velocities of about 2 times higher than Borrelly's has been applied according to Gombosi *et al.* (1986). The optical depth reaches a maximum value $\tau = 1$ at 1 km above nucleus surface, beyond this distance the optical depth < 1. This is higher than the value calculated by

Optical depth of 19P/Borrelly
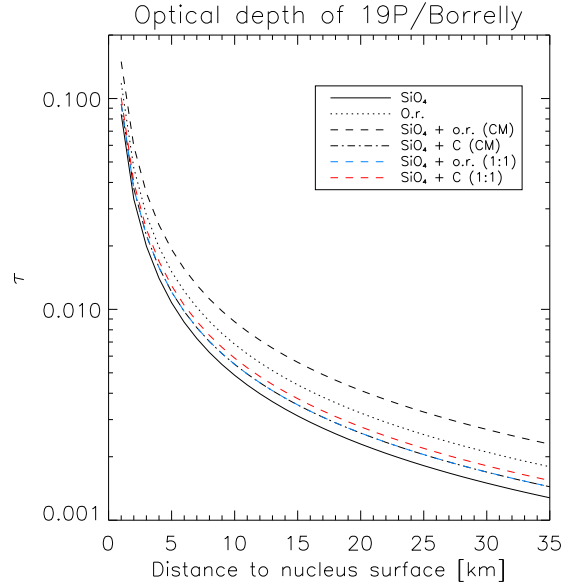
Figure 4.18: This are the calculated optical depths for different particle compositions of Borrelly assuming a dust production rate of 200 kg/s. SiO_4: ——, Organic refractory (o.r.): $\cdots\cdots$, SiO_4 core-o.r. mantle: - - -, SiO_4 core-C mantle: $-\cdot-\cdot-$, Mixed SiO_4 + o.r.: - - - (blue), mixed SiO_4 + o.r. (1:1): - - - (red). The optical depths have been derived for a coma which satisfied the observed reflectance of Borrelly on mid_3.2.

Optical depth of 1P/Halley
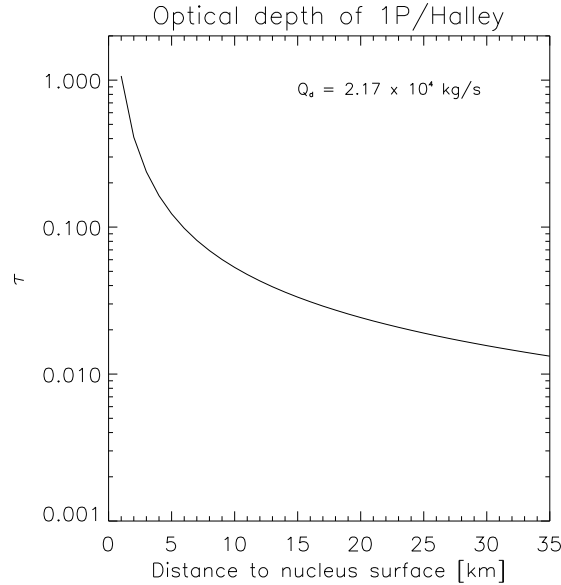
Figure 4.19: The optical depth of Halley for $Q_d = 2.17 \cdot 10^4$ kg/s and a coma composed of 20% SiO_4, 40% organic refractory, 40% SiO_4 + o.r. grains. This composition has been taken from the results of the PIA experiment onboard Giotto (Langevin $et\ al.$, 1987). For the size distribution the values of McDonnell $et\ al.$ (1991) for the Giotto encounter with Halley has been considered.

Keller *et al.* (1987) who deduced $\tau = 0.28$ assuming 1 μm size particles and a geometrical albedo of $p \simeq 0.03$.

However the optical depth has been calculated for an isotropic dust coma (radial symmetric). Mueller (1999) mentioned an increased optical depth for an axial symmetric compared to a radial symmetric coma over the subsolar point. Therefore anisotropic emission could further influence the optical depth.

Chapter 5

Modeling of the Spatial Distribution of the Dust

Remote sensing observations from spacecraft fly-bys can resolve the dust-gas coma of a comet within the first 30 km away from its nucleus. In this region the dust grains are accelerated through interaction with the gas streaming away from the surface. The physical interaction of the expanding gas and dust into the circum-nuclear environment is complicated and numerous theoretical models have been constructed.

At the beginning of this chapter a short overview of this model is given. Afterwards a new approach is introduced to interpret observations of this region close to the nucleus. This approach is based on the assumption that the dust grains are ejected in jets from point sources of different strengths distributed in extended areas of activity on the nucleus surface. These jets can have discrete or continuous cross-sections. The inner coma is interpreted as jets superpositioned around the nucleus body. The detailed steps to construct an inner dust coma of multiple jets will be explained and the physical consequences of the approach will discussed finally.

5.1 Gas Dust Interaction Region

It was recognized as early as the mid 1930s that gas outflow plays an important role in the cometary dust production process. In early treatments of the gas-dust interaction it was assumed that the dust drag coefficient was independent of the gas parameters and that the gas velocity was constant in the dust acceleration region (Whipple, 1951; Huebner and Weigert, 1966).

In the late 1960s the assumption of a constant gas velocity was dropped by introducing a two component treatment of the gas-dust interaction (e.g. Probstein, 1969). It was assumed that heavy dust grains have no thermal motion and collide only with gas molecules. It was pointed out that the gas mean free path was much larger than the dust particle dimensions. Consequently the gas flow could

be considered to be free molecular relative to the dust component. In Probstein's dusty-gas dynamic treatment, the traditional gas energy equation was replaced by a combined dust-gas energy integral. He assumed a single characteristic dust size (a = 0.5 μm) and neglected any external dust or gas heating in the interaction region. Later Hellmich and Keller (1980) pointed out that dust grains can be heated significantly in the inner coma by multiple-scattered solar radiation.

Hellmich (1981) and Gombosi *et al.* (1983) included in their calculations a dust size distribution and could demonstrate that Probstein's single size approximation and their results showed significant differences. Gombosi *et al.* considered as first step, the outflow of gas and dust into an empty coma until the system reached steady state. The sublimating surface was replaced by a reservoir of stationary perfect gas. The surface of this reservoir was covered by a thin layer of friable dust according to the friable-mantle model of Horanyi *et al.* (1984). The gas leaves the reservoir through the friable mantle and starts to carry away dust grains. The outer surface temperature is higher than the sublimation temperature at the bottom of the layer. Gombosi *et al.* described the outflow following the concept of a Laval nozzle with an effective-cross section that varies with distance from the nucleus, reaching its minimum at the sonic point. This approach also provided for a non-steady state solutions and hence descriptions of the onset of outbursts.

Hellmich (1981) further examined how the gas and dust production rates could be influenced by radiation transfer in the coma. The radiative transfer problem in a dusty cometary coma is far from simple and has been investigated by a number of groups using different methods, e.g. Hellmich and Keller (1980); Marconi and Mendis (1984). Marconi and Mendis (1986) investigated the effects of the dust thermal radiation on the energetics of the neutral gas.

Modeling efforts have shown that the spatial extent of the gas-dust interaction region is limited to less than $\sim 30\ R_n$ (see Keller, 1983; Mendis, 1983). Gas particles typically spend about 100 s in this region. This time scale is too short for any significant change in the chemical composition of the gas. Thus a single - fluid dusty hydrodynamical approach is adequate for describing the dynamics of the gas-dust interaction region.

The gas dynamic outflow in two dimensions has been considered by Kitamura (1986 & 1987) who simulated symmetric jets of gas loaded with dust emanating from active source regions. He investigated different activity distributions considering inactive areas and uniform weak outflow from areas surrounding the active source regions. The jet-like structure was followed out to around 100 km from the nucleus. The anisotropy produced by the gas jet smooths out beyond this distance and the coma becomes isotropic.

A further, more recent, model is that of Crifo and Rodionov (1999) who modeled
the circumnuclear environment with multifluids whereby they grouped not only
gas and dust in two fluids but they also distinguished between different "dust
fluids" depending on the dust's nature. The nucleus is assumed to be homogenous
with a constant value of icy area fraction over its surface.

5.2 Inner Dust Coma Model Data Analysis Approach

To be able to study the dust emission in more detail, to constrain possible physics
behind it, and to determine the sources on the nucleus surface,we introduce a new
analysis method. Based on Kitamura's hydrodynamic models of isolated dusty
gas jets, the dust emission is approximated as jets with a fixed opening angle
emitted from active regions on the nucleus surface. This is a simplified model of
the outgassing features, in which the dust emission is assumed to undergo force
free outflow within a fixed opening angle from individual sources. Thomas *et
al.* (1988) already suggested a similar approach with dust cones to explain the
intensity profiles around the nucleus of comet Halley. The observed emission of
superimposed dust jets emitted from an elliptical nucleus can be simulated and
compare with the resulting brightness distribution.

Jets are assumed to emit with a fixed opening angle from point sources distributed
over the nucleus. These multiple discrete sources themselves can appear to form
active areas. Due to the superposition of jets complex patterns are formed in the
coma. The attempt is to model the brightness map of the first 30 kms around
the nucleus by fitting it with a number of discrete sources. This superpositioning
dust jet model (SDJM) is based on a linear algebraic idea, where each signal can
be written as a sum of weighted source terms depending on the opening angle of
the jets and their positions (Figure 5.1).

Thus a linear system of equations can be set up

$$\rho_{0,0}\frac{Q_0}{4\pi v_0} + \rho_{0,1}\frac{Q_1}{4\pi v_1} + \cdots + \rho_{0,n}\frac{Q_n}{4\pi v_n} = S_0$$

$$\rho_{1,0}\frac{Q_0}{4\pi v_0} + \rho_{1,1}\frac{Q_1}{4\pi v_1} + \cdots + \rho_{1,n}\frac{Q_n}{4\pi v_n} = S_1$$

$$\cdots\cdots\cdots\cdots\cdots\cdots\cdots\cdots\cdots\cdots\cdots\cdots\cdots\cdots\cdots$$ (5.1)

$$\rho_{n,0}\frac{Q_0}{4\pi v_0} + \rho_{n,1}\frac{Q_1}{4\pi v_1} + \cdots + \rho_{n,n}\frac{Q_n}{4\pi v_n} = S_n$$

where two types of profile can be chosen for ρ, namely,

- Cone profile:

$$\rho = 2 \cdot \int_0^l \frac{1}{r^2} dl \tag{5.2}$$

whereby the cone opening angle has to be considered in r.

- Gaussian profile:

$$\rho = 2 \cdot \int^{l_1} \frac{1}{r^2} \cdot e^{\frac{-\theta^2}{2\sigma^2}} dl \tag{5.3}$$

The angle between the vector (source-signal) and the symmetry axis of the jet is ϑ and σ is the full width half maximum (FWHM).

In Eq. 5.1, Q is the dust production rate and v is the dust velocity. The column density, N, for a jet is defined: $N = \frac{Q}{4\pi v} \cdot \rho$.
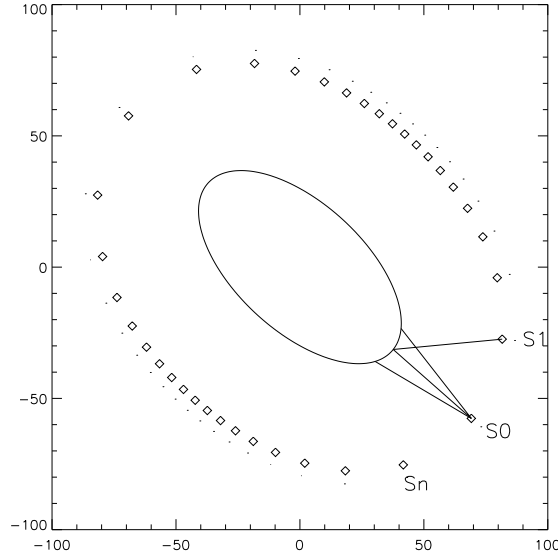

Figure 5.1: The first ellipse represents the nucleus. The source are situated on the perimeter of the ellipse. The signals taken into the linear combination system are equidistant to this ellipse. The signals shown here are place every 10° away from each other.

By solving the linear system, eq. 5.1, a n-vector $\frac{Q}{4\pi v}$ is obtained which gives information about the ratio of the production rate to the outflow velocity. The right-hand side quantities of the linear system are the signals of the MICAS images along one equidistant envelope around the nucleus (Figure 5.1 and Figure 4.6). This approach attempts to place constraints on hydrodynamic models by direct analysis of the data in a simple and rapid way. With the solution of the linear system the position and Q/v values of the dust emission on the nucleus are received. These inputs can then be used to produce a simulated image of the inner coma.

5.3 The SDJM with Discrete Dust Cones

The simulation of the dust ejection with cones is described schematically in Figure 5.2. The emission cones were placed at equal angular distances (e.g. $10°$, $20°$, etc.) and with fixed half-opening angle around the nucleus. Depending on the opening angle and the location of the dust jets, a linear system according to Equation 5.1 can be set up and solved for the groups of input parameters which have been applied.
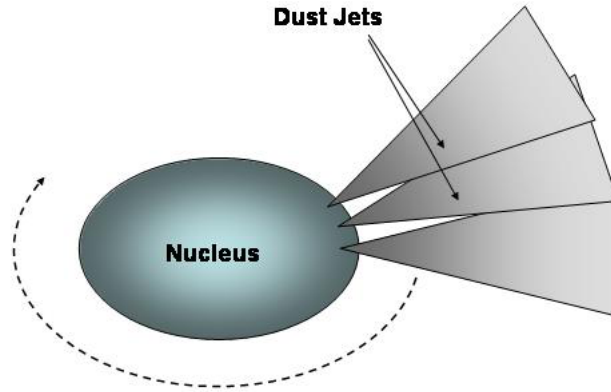

Figure 5.2: This sketch shows an example of three dust cones which are ejected from the nucleus surface. The emission sources are lying below the nucleus boundary, simulating active areas lying closer to the center nucleus in projection. The subsequent cones are placed at equal angular steps around the nucleus (marked with the arrow).

Several simulations were run with different combinations of input parameters and assuming constant dust outflow velocity. The simulations with half-opening angles between $10°$ - $40°$ were able to reproduce most features e.g. the main jet, the nightside dust and the fans if the input signal is chosen between 2 - 5 km away from the projected edge of Borrelly's nucleus. Using dust cones of $10°$ half opening angle leads to resolved structures (Figure 5.3) which requires higher angular resolution (i.e. more sources). A better fit is obtained with larger half-opening angles, e.g. $20°$ to $40°$ (Figure 5.3 left). However, the linear system of equations

forces an almost perfect fit at the distance from the nucleus where the signal from
the image is taken from to solve the system. One can only judge the accuracy
of the solution by then extrapolation the resulting cones to simulate the whole
image.

When the extrapolation is made, one discovers severe difficulties. Firstly, the
cones become resolved close to the nucleus. Secondly, adjacent cones can give
alternately positive and unphysical negative values indicating instability in the
solution. The extrapolation to larger distances then fails badly to match the
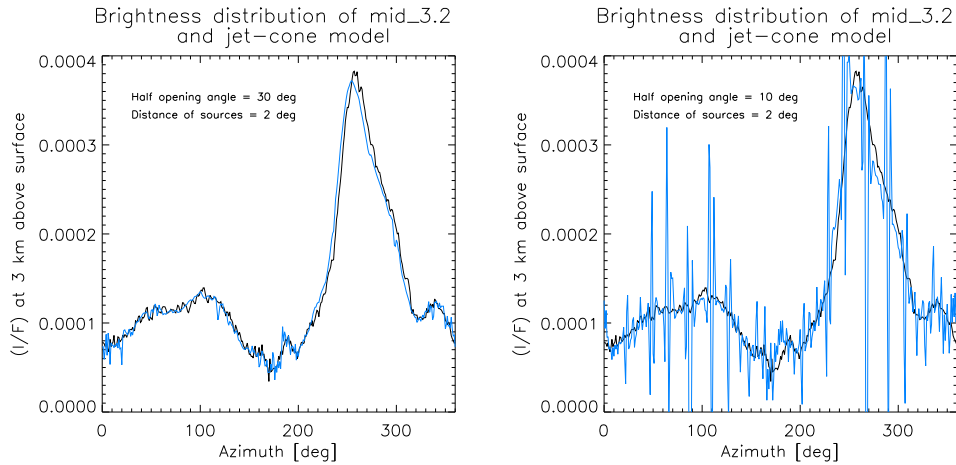observations. Discrete cones are therefore a poor approach.

Figure 5.3: The image on the left is the brightness distribution of the simulated
dust coma (blue line) and the observed one of Borrelly at 3 km above the nucleus.
The half opening angles of the cones are $30°$, the sources are situated $2°$ (equal
angle step) away from each other. The input signal has been taken at 3 km
above the projected nucleus surface. The image on the right side results from the
simulation considering a dust cone of $10°$ half opening angle. The sources are
placed at $2°$ away from each other and the input signal height is 3 km.

5.4   SDJM with Gauss-Profile Jets and Acceleration

Because the interpretation of the dust emission with discrete cones did not give
satisfactory results, Gaussian profiles has been used as an alternative. This ap-
proach reproduces the main emission features well, giving no resolved structures
even with an opening angle of $10°$ FWHM. Figure 5.4 gives the results of a dust
coma structured by Gaussian jets with a FWHM of $10°$ and an angular sepa-

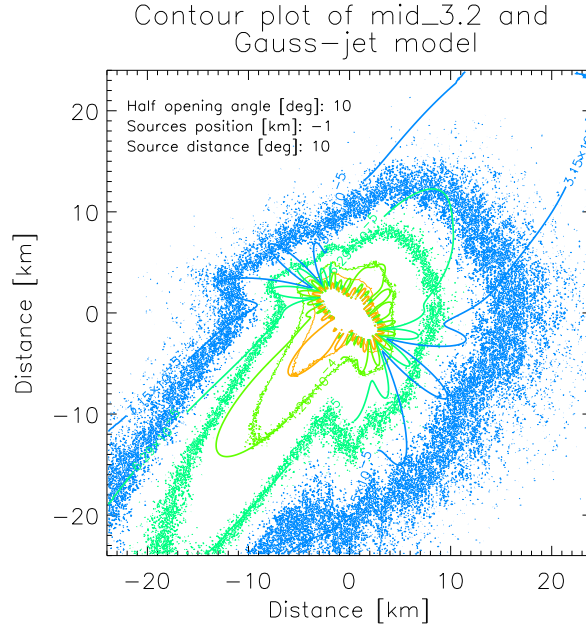Figure 5.4: This figure shows the contour of Borrelly on mid_3.2 and of the SDJM with Gauss-profile jets. The FWHM is 10° and the jets are positioned 10° away from each other around the nucleus. The jet sources are 1 km away from the projected margin of the nucleus.
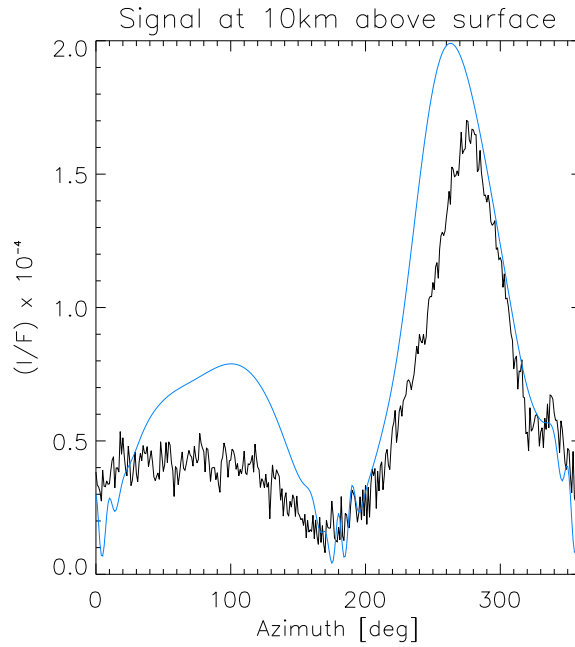

Figure 5.5: This plot shows the brightness distribution of Borrelly (black line) and the SDJM (blue line) at 10 km above the nucleus surface.

ration of 10° for the sources. The linear system constrains the model to fit the observed intensity at 3 km above the nucleus. On the contour plot it is recognized that the main jet of the SDJM is less collimated than the one of Borrelly. This can be explained by the construction of the observed main jet. The main jet comprises several components (the α and β jets) which merge non-radially into one prominent dust emission. This means that the dust do not leave the nucleus along a trajectory orthogonal to its surface. This assumption is made in this "ideal"-case model.

The dust fans at the lower and upper tip of the nucleus could not be reproduced with this combination of free parameters (i.e. FWHM and source distances). The sources are too far from each other or the opening angle is too narrow.
The brightness of Borrelly's coma is higher close to the nucleus than in the model. At greater distances from the nucleus (> 8 km) the brightness distribution of the real comet is lower (see Figure 5.5). A big difference can be seen between the observed and the simulated feature on the "night side". The model's $\oint I ds$ is almost constant which suggests that the deviation from a point source is not an adequate explanation for the observed behavior at Borrelly. Other physics must be included.

SDJM with dust acceleration   The next step was to consider acceleration of dust particles in the SDJM. This has been done by inserting a variable dust velocity in the integral described in Equation 5.3. The velocity values presented in Figure 4.15 have been applied. The dust velocity of grains with radius $\approx 0.5 \ \mu$m has been used. The resulting dust coma is given in Figure 5.6. The contour plot shows the observation and the model result. The sources are positioned 12° away from each other. Sources are placed on the surface of the ellipse and also 1 km inside the ellipse (simulating sources closer to the nucleus center in projection). The sources of the jets located on the outer margin of the projected nucleus(= 0 km) have 30° FWHM, those 1 km inside the ellipse have a FWHM of 15°.

The collimated shape of the main jet on the sunward side is well fit with these parameters. The fit of the dust fans and the nightside feature has been improved in this approach. However it can be recognized that in the observations the dust fans on the tip of the nucleus smooth out with increasing distance to the nucleus. However, this emission features are still recognized distinctly in the model.

The brightness radial profile of Borrelly and the SDJM along the main jet and the nightside are plotted in Figure 5.7. The profile along the main jet of the model fits the observed one, showing the constant outflow behavior at higher distances and decrease closer to the nucleus indicating deviation from a point source. In the first 3 km away from the nucleus center the model's profile show a steeper slope compared with the observed one. This can be explained with the assumed
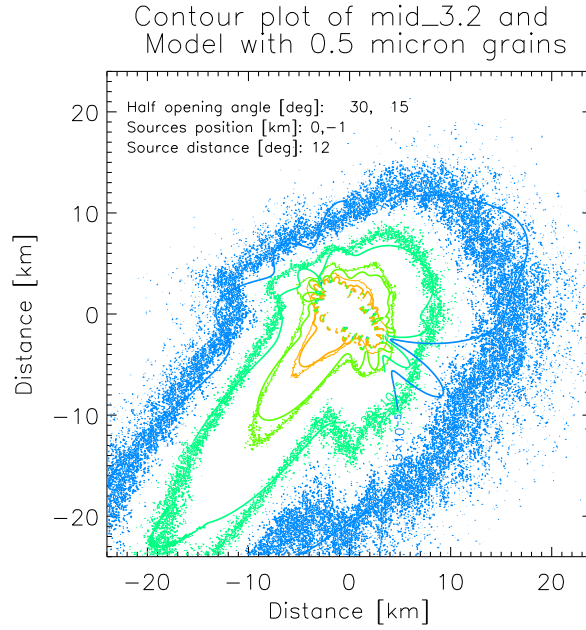
Figure 5.6: Modeling the dust coma (solid line) with two Gauss-jets of different FWHM, 30 and 15°, and acceleration. The velocity values has been taken from Figure 4.15 with considering the values of particles of 0.5 μm size. The jet sources are positioned at 0 and -1 km away from the nucleus projected margin, respectively. The contour of SJDM simulation is overplotted by the observed dust coma of Borrelly seen on mid_3.2.

elliptical nucleus of the model and the irregular shape of Borrelly's actual nucleus. Straylight also influences the observed intensity. This will be discussed later. On the other hand, the decrease of Borrelly's profile with increasing distance to the nucleus on the night side could not be reproduced by the model.

Figure 5.8 gives the integrated intensity, $\oint I ds$, of the SDJM and Borrelly. The model's $\oint I ds$ increases with decreasing distance to the nucleus surface only until ≈ 200 m away from the nucleus surface, afterwards its gradient goes to ∞. The model appears to fit the observation well but there is a systematic difference. The observed $\oint I ds$ increases continuously.
The $\oint I ds$ values of the model reaches a constant value at > 10 km away from the nucleus, indicating constant free-radial outflow. The observation however shows a steady decrease with distance. This deviation of the model and the observed $\oint I ds$ might be expected if one considers the radial brightness profiles plotted in Figure 5.7. The decrease of the radial profile on the nightside could not be reproduced and thus the difference in $\oint I ds$ is clear.

Many other input parameters, e.g. varying the source positions and the opening
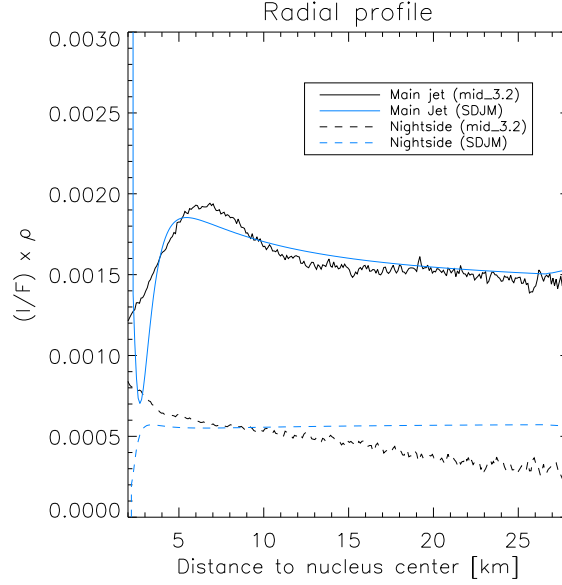
Figure 5.7: The radial profile of Borrelly (black) and the SDJM (blue) along the main jet and on the nightside.

angle, has been tested but the presented parameters provided the best fit.

One possible explanation for the steepening of the intensity profile could not only be acceleration processes but straylight from the nucleus inside the camera. To examine the contribution of straylight to the observed brightness, the Braille data taken by MICAS have been used. Because asteroids are not surrounded by any observable dust and gas coma, one should observe a sharp profile at their limbs. Any deviation from this signal can be attributed to straylight. From the analysis of the Braille images it has been deduced that straylight plays only a major influence in the first 2 pixels away from the limb of the solid body. Here it has a contribution of $\approx$ 10 - 30 % of the observed signal. Because this is the region of strong $\oint I ds$ increase, the signal of Borrelly's dust coma will decrease significantly if the straylight contribution is subtracted. Nevertheless the observed $\oint I ds$ is still higher than seen in of the SDJM.

Halley's inner dust coma has also been modeled with the SDJM without satisfactory results. The decrease of Halley's $\oint I ds$, Fig. 4.7, with decreasing distance to the nucleus could not be obtained. This could be explained with an optical thick coma in the first 10 km away from the nucleus or particle fragmentation into optically large sizes. Thus this approach can not be applied because the dust emission cannot be traced back easily.

In summary Borrelly's inner dust coma can be approximated by accelerated dust grains emanated in jets from distributed point sources forming active regions on
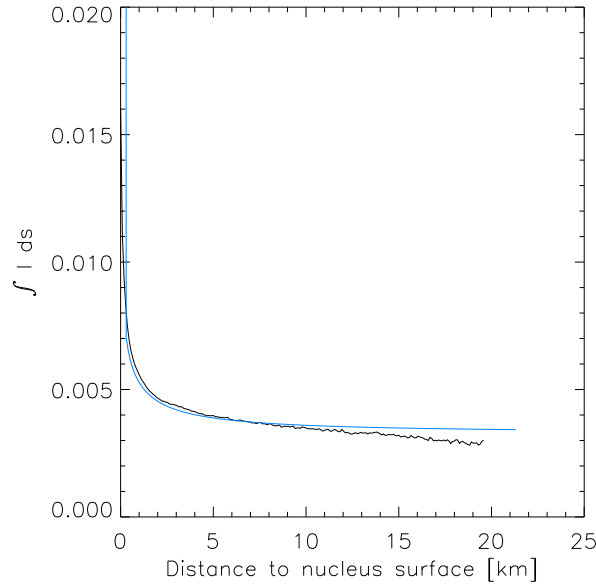
Figure 5.8: The integrated intensity of the model result presented in Figure 5.6 and Borrelly's on mid_3.2.

the nucleus surface. The dust particles can not be entrained in distinct sharp cones but in smooth jets with a peak density along its symmetric axis. The collimated main jet could be well generated with narrow jets, whereby the fans and night side emission are better generated with broader jets.

The SDJM cannot reproduce all of Borrelly's peculiarities. The intensity gradient on the anti sunward side cannot be modeled. This is a further evidence that dust seen in projection in the nightside hemisphere is probably dust swept around from dayside regions through lateral expansion (Keller and Thomas, 1989; Knollenberg, 1994).

The solution of the linear equation still gives negative "source strengths". If the linear system is force to render only positive values, the fit is changed for the worse of model and observed brightness distribution. Fig. 5.9 gives the brightness distribution at 3 km away from the nucleus for two SDJMs with Gauss-jets. Both simulations have the same input parameters but the figure on the left includes the negative values of the linear equation system. The figure on the right belongs to the simulation with only positive source strengths. It is recognized that the main jet of the SDJM of the right figure is less collimated than the one on the left. Also the dust fans could not be well reproduced and the nightside brightness is higher. Therefore negative solutions of the linear equation system are indicative of departure from assumed gaussian profiles.
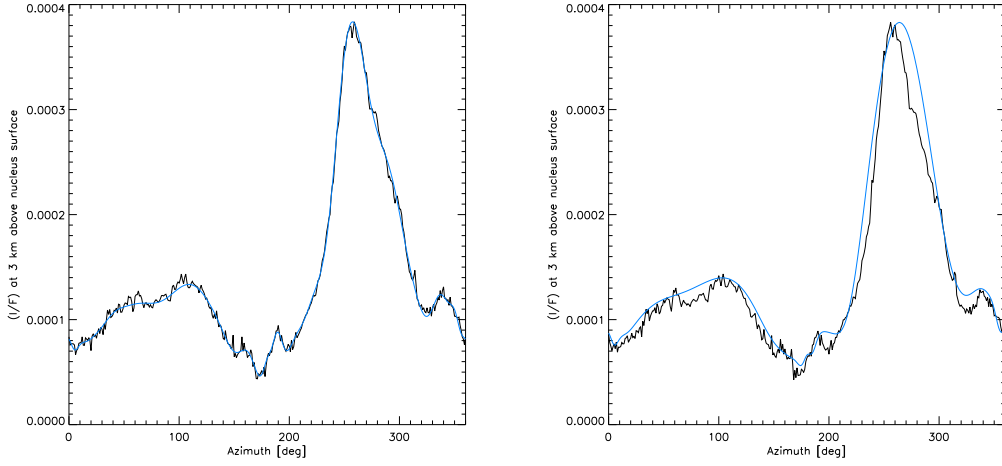
Figure 5.9: The brightness distributions of the SDJM with jets of 20° FWHM and the observed brightness distribution at 3 km away from the nucleus. The sources are 10° away from each other. The left plot shows the simulation including positive and negative source strengths. The plot on the right belongs to the model with the solutions of the linear equation being forced to be positive.

The increase of $\oint I ds$ close to the nucleus surface indicates not only dust acceleration. A noticeable increase of $\oint I ds$ with superpositioned jets of two opening angles has been obtained. However, the magnitude of this increase could still not match the data. This might be explained by particle fragmentation into optically small particles or differences in the assumed acceleration. If fragmentation occurs, then the question arises why this process only takes place in the first 200 - 800 m away from the nucleus. It seems questionable if fragmentation can take place already within such short distance from the nucleus.

Chapter 6

Observations at Pik Terskol

The goal of the ground based observation campaign of comet Borrelly at the 2m-Zeiss telescope at the Pik Terskol observatory was to place the DS1 encounter observations into a broader context. Compared with the in situ data, which reveal a nucleus vicinity dominated by anisotropic dust emission, the remote data provide images of a coma out to a distance of 10^3 km. These images give a view of a region, where the resolved emission features in the circumnuclear environment have already "dissolved" into a broader dust cloud, in which different forces begin to dominate the motion of the dust grains.

This chapter will deal with the analysis of the Earth-based observation data. First, the normalized brightness map of Borrelly taken with different filters will be presented. The radial profiles have examined for departure from the $1/\rho$ law. The dust production in terms of $Af\rho$ has been determined. In addition the color of the dust has been analyzed, giving further information about the spatial dust size distribution. Finally the morphological peculiarity of Borrelly has been examined. For this, a special processing technique has to be employed to enhance possible asymmetries, which could have their origin in the anisotropic dust emissions seen on the encounter images.

6.1   The Outer Dust Coma and Tail of Borrelly

The observations themselves have been described in chapter 2. To give an overview of the brightness of Borrelly's dust coma, the continuum images taken with the narrowband filters have been normalized with the mean solar disk intensity, $i_\odot$. Unfortunately only the images of Borrelly on the night between September 19/20 and 20/21 could be used here. The images taken at the time of DS1's encounter, September 21/22, were disturbed by dense clouds and do not give any useful information. Some of the images contain some very extended bright patches. This are the star trails which could not be removed without influencing the original source data.

Figure 6.1: This are two representative continuum images taken in the blue range (IF444) normalized by the mean solar disk intensity for two subsequent nights (September 19/20 & 20/21, 2001). The distances were transformed from equal angular sizes to km. The lower color bar shows the intensity scale.
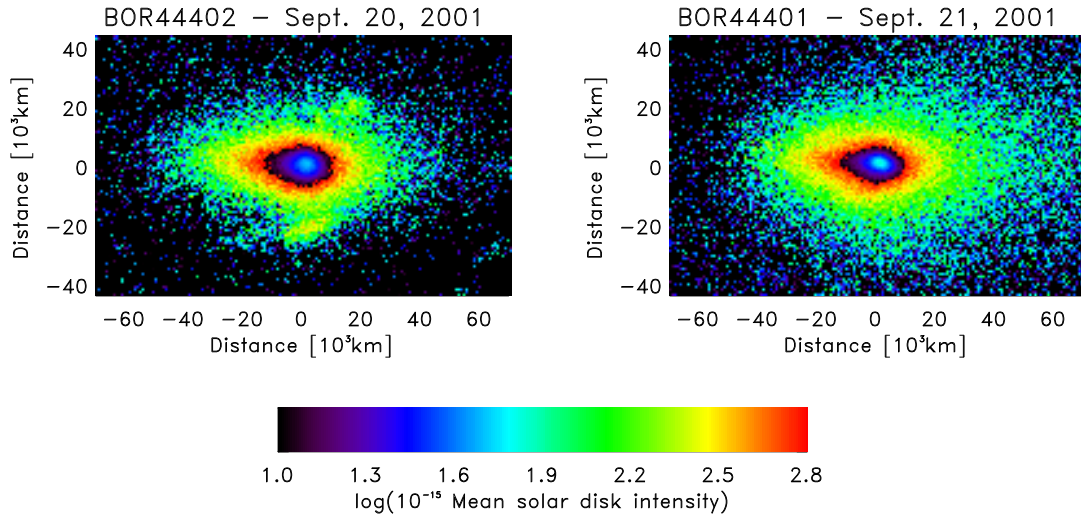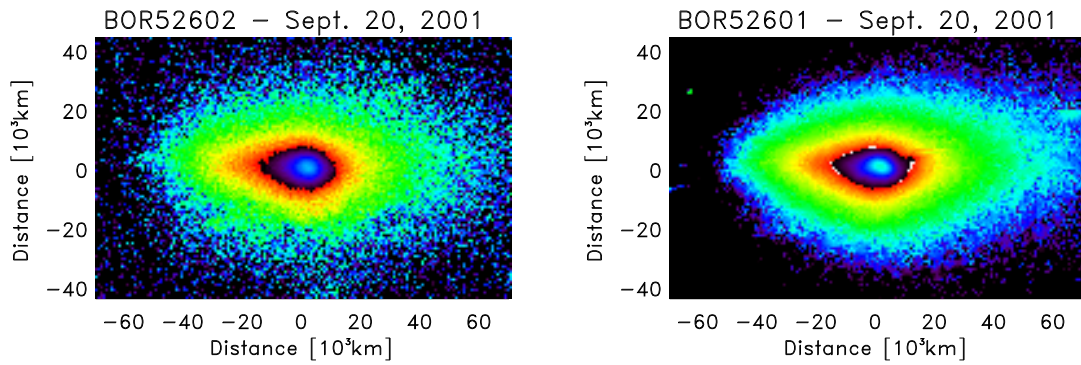

Figure 6.2: Two representative continuum images taken in the visible range (IF526) normalized by the mean solar disk intensity for two subsequent nights (September 19/20 & 20/21, 2001). The intensity scale of the images follows the color bar in Figure 6.1.

Figure 6.1 shows calibrated brightness images in blue continuum from two nights. The intensity scale of all images is presented by the logarithm of $10^{-15} \times$ the mean solar disk intensity. The color table repeats if the intensity exceeds $2.8 \cdot 10^{-15}$ mean solar disk intensity. This provides a better insight into the region in the center of about $20 \cdot 10^3$ km away from the nucleus. The same procedure has been applied to the continuum images taken with the IF526 (see Fig. 6.2), IF631 (see Fig. 6.3) and IF642 (see Fig. 6.4) filters.

The dust coma of Borrelly has in all continuum images an elongated shape with a peak pointing in projection towards the Sun. The projection of the Sun-comet vector is situated $\approx 18°$ above the horizontal line and to the left. The averaged extension of the coma is around $80 \cdot 10^3$ km in length and $40 \cdot 10^3$ km in width. The observations on September 21 show a more prominent dust tail than on the day before, probably indicating an increased dust production. Apart from this increased intensity of the tail structure, no further dominant variability can be recognized. A peak intensity between $2.5 - 4 \cdot 10^3 \times$ the (solar disk intensity $\times 10^{-15}$) is observed on every image in a region of $\approx 2\text{-}3 \cdot 10^3$ km away from the center of the coma. Comparing to the similar shape of the coma in the IF444, IF 526 and IF642 images, the IF631 image appears to have a spherical shape superimposed over mentioned elongated form. This is because of the emission of of O ^{1}D at 630.8 nm.

6.1.1 The O ^{1}D emission

The intensity of O ^{1}D can be derived from the continuum images of IF631 and IF642. The brightness observed with the IF631 filter is composed by the brightness of the O ^{1}D molecules and the continuum brightness

$$I_{631} = I_{[OI]} + I_{cont} \tag{6.1}$$

Assuming that the brightness of the dust coma at 642 is similar like the one at 631 without any contribution of this O^{1D} molecule, its intensity can be derived by

$$I_{[OI]} = I_{631} - I_{cont} = I_{631} - I_{642} \tag{6.2}$$

Figure 6.5 gives the subtracted image of O ^{1}D from the two continuum images. A slightly higher column density of O ^{1}D on the sunward side can be recognized, indicating an asymmetry of the emission of the parent species, H_2O and OH. A stronger asymmetry of gas emission on Borrelly's sunward side has been detected by Schleicher et $al.$ (2003) for CN. This indicates an anisotropic emission of CN and O ^{1}D on the sunward side.
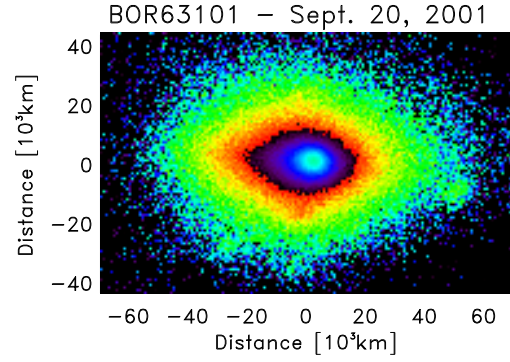
Figure 6.3: This image shows the brightness of the dust coma on September 21, 2001. Its intensity scale of the image follows the color bar in Fig. 6.1. The shape of this dust coma appears to be less elongated than the shape on the other images, which can be explained by O^1D molecules.
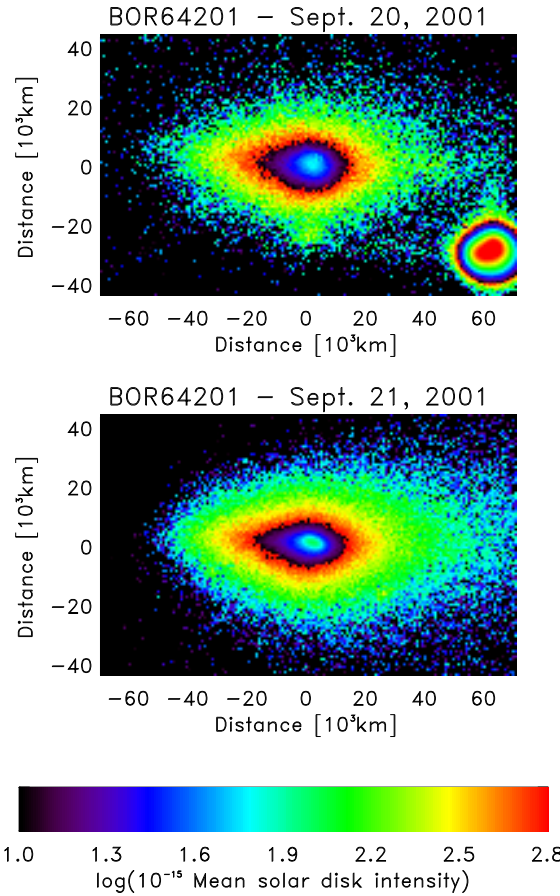
Figure 6.4: This are the red continuum (IF642) images normalized by the mean solar disk intensity. The distances were transformed from equal angular sizes to km.
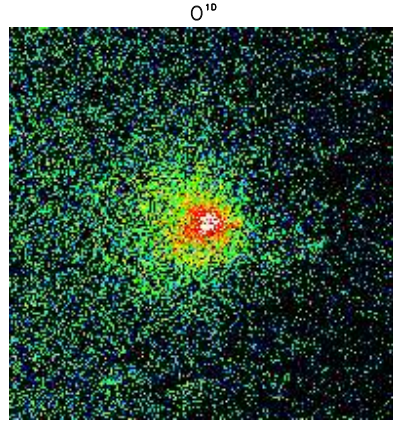
Figure 6.5: This O ^{1}D frame has been continuum subtracted. The resulting image is essentially only O ^{1}D emission. The image comprise a region of 130 $\cdot 10^3$ km along the x-and y-axis, with north at the top and east to the left.

6.1.2 The Radial Dust Profile

To investigate any trends of the dust outflow with aperture size (such as deviations from free radial outflow) the normalized intensity has been plotted versus ρ. Thus the gradient of this radial profile of the coma should equal -1 in a log-log fit.

Figures 6.6, 6.7, 6.8 and 6.9 show the radial normalized intensity plotted against the projected radial distance to the comet's supposed nucleus along the sunward side direction, the tailward side direction and as average over the whole azimuth of 2π. The sunward side and tail profile are medians of a 10° wedge centered on the measured peak direction and in the opposite direction.

The profiles on all plots decrease monotonically with increasing aperture. However the gradient of the fall-off is not constant along all distances. The intensity curve flattens below about 3 $\cdot 10^3$ km from the center. This can be explained with seeing, telescope tracking and the spatial quantization on the image by the CCD pixel grid (Jewitt and Meech, 1987). At higher distances the gradient steepens.

As expected, the radial profile along the sunward side is higher than the one along the tail. On all plots, a rather steep gradient for this direction can be recognized. This steep gradient is indicative of acceleration of the dust grains by radiation pressure. In comparison the tailprofile follows the $1/\rho$ fall-off constantly until an aperture size of $3 \cdot 10^4$ km. The averaged profile follows in a limited region between $\approx$ 3 - 7 $\cdot 10^3$ free radial outflow behavior, and further it decreases faster because of the contribution of the sunward side and the one perpendicular to the sun-comet line, where radiation pressure dominates.
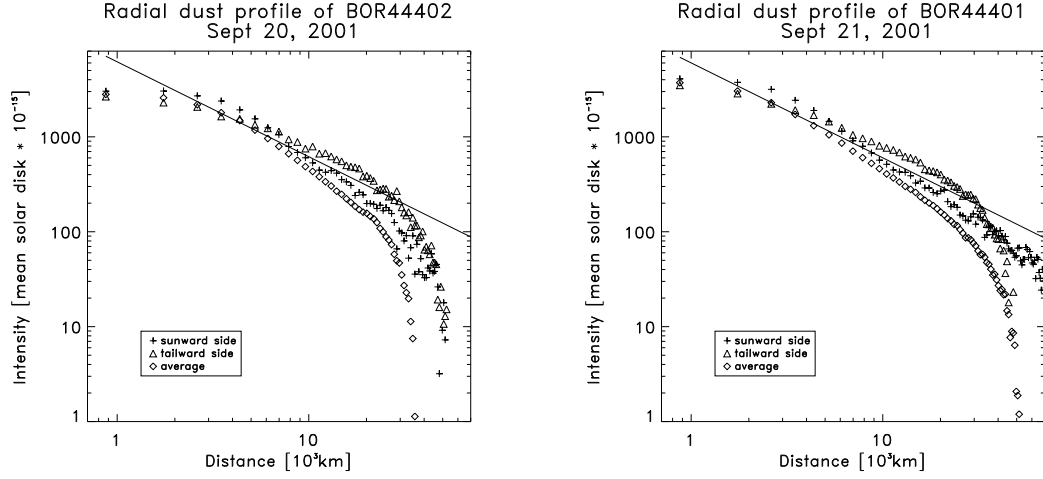
Figure 6.6: The dust intensity of the IF444 images with respect to the mean solar disk is plotted versus the projected radial distance from the comets center. The straight line with a slope of -1 represents the 1/r behavior of the dust outflow. The symbols denote measurements of the sunward (+), tailward ($\triangle$) and azimuthally averaged ($\Diamond$) profiles.
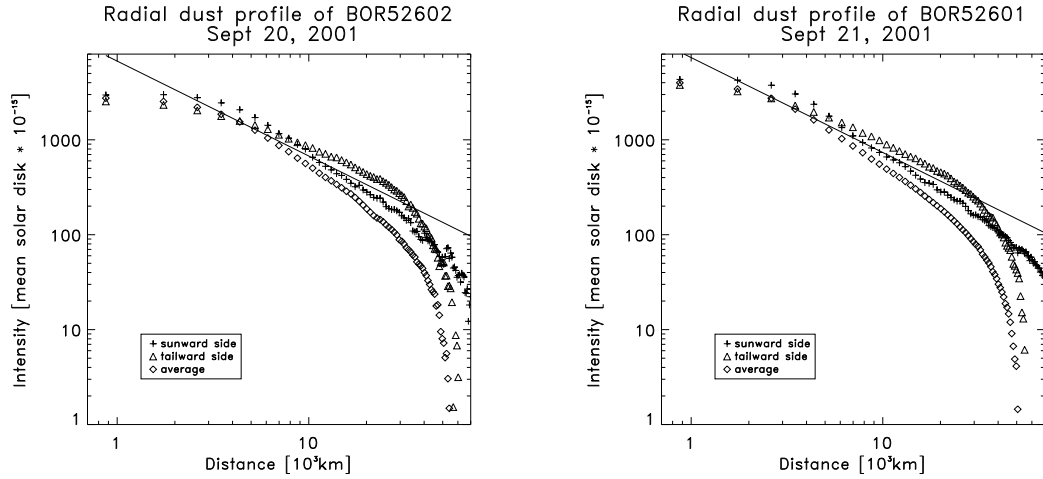
Figure 6.7: This are the radial dust profiles of the IF526 images. The straight line represents the $1/\rho$ behavior of the dust outflow. The sunward side: (+), the tailward side: ($\triangle$) and the azimuthally averaged profile: ($\Diamond$).
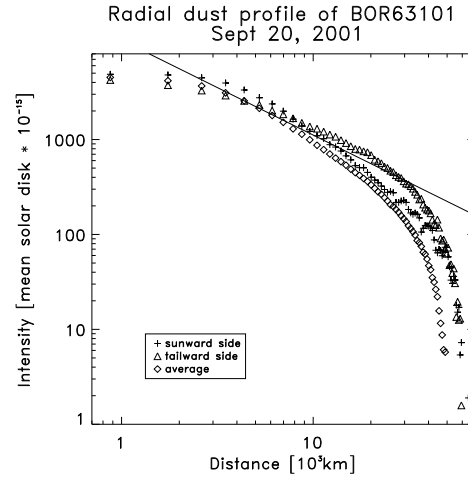
Figure 6.8: This plot shows the radial dust profiles of the IF631 images. The straight line represents the $1/\rho$ behavior of the dust outflow. The sunward side: ($+$), the tailward side: ($\triangle$) and the azimuthally averaged profile: ($\diamondsuit$).
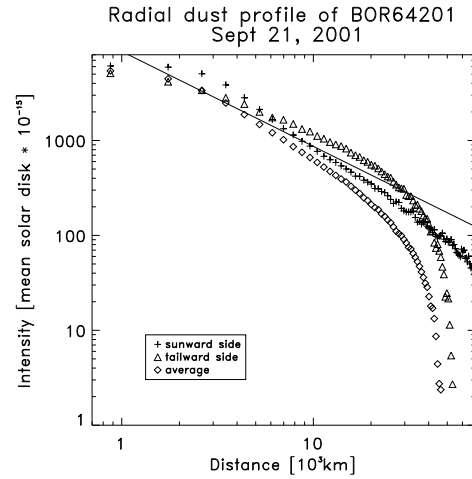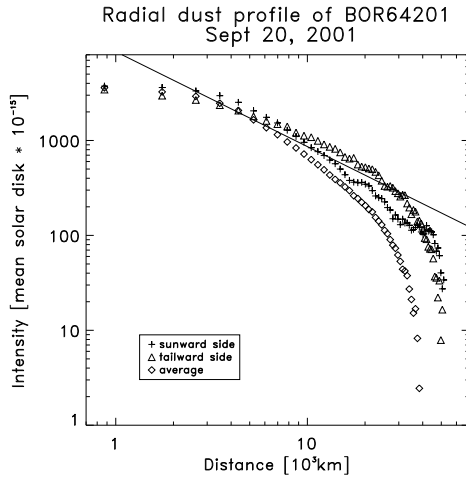
Figure 6.9: The radial dust profiles of the IF642 images. The straight line represents a $1/\rho$ behavior. The sunward side: ($+$), the tailward side: ($\triangle$) and the azimuthally averaged profile: ($\diamondsuit$).

6.1.3   Color of the Dust

Variations among the continuum colors of the comets at a given wavelength are significant and not correlated with heliocentric distance, phase angle or mass-loss rate. The color differences seem to result from intrinsic differences among the grains in different comets, (Jewitt and Meech, 1986).
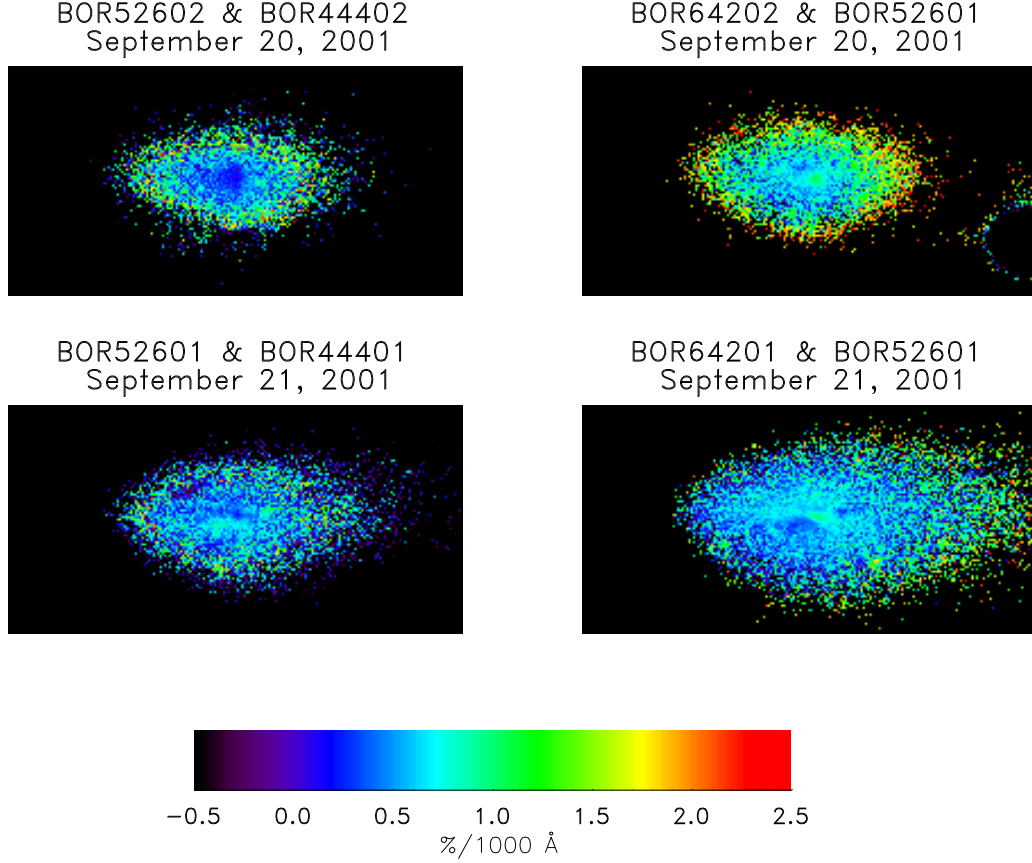
Figure 6.10: Color maps of the dust distribution on September 20, 2001 and September 21, 2001.

To facilitate a comparison of measurements which are obtained with different filters one may use % reddening per 1000 Å (A'Hearn *et al.*, 1984; Jockers, 1997). If B and R are the filters, and λ_B and λ_R the corresponding wavelength in Å, the reddening percentage can be obtained from following equation:

$$S'(\lambda_B, \lambda_R) = \frac{I_B - I_R}{\lambda_B - \lambda_R} \times \frac{2000}{I_B + I_R} \tag{6.3}$$

I_R and I_B are the intensities (relative to the Sun) at the wavelengths, λ_R and λ_B. The pairs of red and blue images from each particular night were use to produce

color maps of the dust continuum.

To improve the signal-to-noise ratio on the color maps, some preprocessing steps were performed. A mask was created with values equal to 1 where the image contains signal greater than 1σ of the sky background and 0 elsewhere. The masks for the pair of blue and red image are multiplied with each other and a final mask was obtained. The blue and red image were multiplied with this mask. To obtain the color map, Equation 6.3 has been applied. The results of this procedure are presented in Figure 6.10, which shows the dust color obtained from the IF444 and IF526 filters or IF526 and IF642 filters.

The systematic differences among the standard stars images were ≈ 0.23 % from 4445 Å to 6425 Å wavelength. Therefore the gradient errors were $\pm\ 0.11$ % per 1000 Å.

Grains, which are small compared to a wavelength satisfy the Rayleigh approximation. Thus the scattered radiation is relatively blue. For larger grains the scattering efficiency falls from the maximum towards the large-particle limit and scattered radiation in this regime is relatively red (Jewitt and Meech, 1986). Thus reddening is indicated by $S'(\lambda_1, \lambda_2) > 0$ and blue scattered radiation by $S'(\lambda_1, \lambda_2) < 0$.
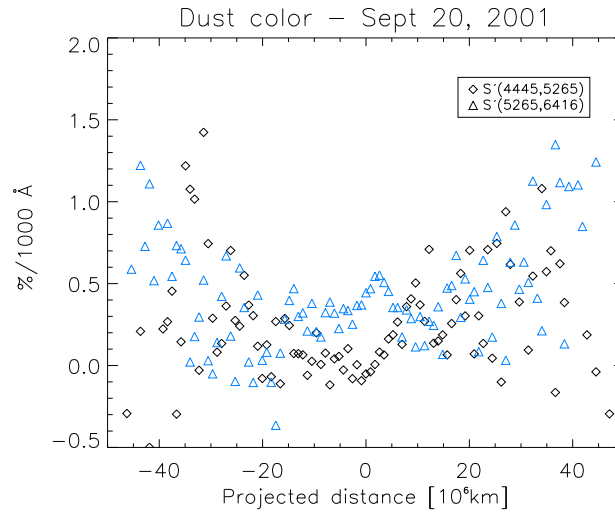
Figure 6.11: The reddening profile derived from IF444/IF526 ($\diamond$) and IF526/IF642 ($\triangle$) of September 20, 2001 along projected distance from the nucleus. The negative distances denote the sunward side and the positive distances the tailward side.

The color maps for the filter pairs IF444/IF526 and IF526/IF642 are presented in Figure 6.10 for the two nights of Sept 19/20 and 20/21, 2001. The reddening

of Borrelly's dust coma is very low with values < 2 %/1000 Å and an average value of ≈ 0.5 %/1000 Å. In the range of $20 \cdot 10^6$ km away from the nucleus the reddening of the scattered light is around 0.5 %/1000 Å with values going below zero, indicating blue scattering. The reddening increases at distances $> 20 \cdot 10^6$ km away from the supposed position of the nucleus.

Compared to other comets (notably Halley) Borrelly's coma is therefore dominated by small grains. The outer margin of the dust coma, the envelope, is popularized by bigger particles. Because there is a maximum radius which will reach the maximum apex distance.

The S'(4445,5265) of the two nights do not show any significant changes. The same behavior has been observed for the S'(5265,6426) image of September 20, 2001. But significant differences can be recognized for the S'(5265,6426) of the subsequent night, which reddening varies only around 0.2 %/1000 Å. Again this is very low for comets.

6.1.4   Dust Production Rate

The dust activity of a comet, measured in terms of the quantity $A(\theta)f\rho$ has been introduced in Equation 4.7. Following this equation, the $Af\rho$ values of Borrelly seen from the Earth for the IF444, IF526, IF631 and IF642 images have been derived (Table 6.1). To obtain the albedo-filling factor product (Eq. 4.5) a straight line with a slope of -1 has been fitted to the log-log plot of the intensity versus the projected radial distance (Fig. 6.6 - 6.9).

To derive the dust production rate, the values between $\approx 3 - 8 \cdot 10^3$ km of the averaged profile has been used, because they follow the $1/r$ profile. This line is plotted on all images.

The Afρ at $\lambda = 443.5$ nm and $\lambda = 525.5$ nm ranges between 400 - 500 cm, while the $Af\rho$ at the longer wavelength of 641.6 nm is higher with an average value around 600 cm. Apart from the $Af\rho$ value derived from the IF526 images no variations can be recognized in the two nights. This is somewhat surprising because of the more pronounced dust tail on 21th September.

Schleicher *et al.* (2003) derived $Af\rho$ values between 400 - 500 cm for the encounter period of DS1 and Borrelly. This agrees well with the value obtained from the Pik Terskol data.

6.1.5   Morphological Features

To enhance the visibility anisotropic emissions in the coma, the images have been processed by converting the image of the comet to a (r,θ)-plot, an azimuthal plot of the coma with increasing distances, r, to the nucleus. Each horizontal line

Data	Date	$Af\rho$ [cm]
BOR44401	Sept. 20	432 ± 2
BOR44402	Sept. 20	436 ± 9
BOR52601	Sept. 20	416 ± 15
BOR52602	Sept. 20	453 ± 8
BOR64201	Sept. 20	600 ± 16
BOR64202	Sept. 20	588 ± 8
BOR44401	Sept. 21	403 ± 11
BOR44402	Sept. 21	417 ± 7
BOR52601	Sept. 21	482 ± 20
BOR64201	Sept. 21	584 ± 22

Table 6.1: The $Af\rho$ values determined from the continuum images of the Pik Terskol data set with the standard deviations.

of the (r,θ) representation was then normalized to the maximum and minimum values along this line (A'Hearn *et al.* (1986). This procedure removes all radial variations. Afterwards the plot is converted back to the conventional image format.

The results of this procedure applied to the Pik Terskol data are shown in Figures 6.12 and 6.13, which are representative for all images taken in this campaign. Celestial North is at the top of all images, and East is on the left in all images. The Sun direction is defined.

A dominant dust emission on the sunward side is visible on all processed images, while a fainter enhanced dust "fan" is seen on the opposite direction. The strength of the second feature varies from image to image. It can be well recognized on the images taken with the IF526 and the broadband RX filters, but less strong on the IF444 and IF642 images. There are no spiral shapes identified in this dust emission which could be attributed to rotation. An averaged position angle[1] of $\approx 92°$ has been obtained for the sunward side emission. Its width is around $30°$ whereby the emissions on the IF642 images have a lower width of $\approx 25°$. There are no variations in the width observed between the two subsequent nights.

Because of the narrow and straight appearance of the sunward side emission, it has been concluded that the dominant emission is emitted closed to the pole of the nucleus. This has been reported by Sekanina (1979), Fulle *et al.* (1997) and Schleicher *et al.* (2003). This evidence points to a correlation between the dominant sunward emission peak seen from the Earth and the main jet observed on the MICAS images.

---

[1]Position angles are measured from 12pm counter clock wise
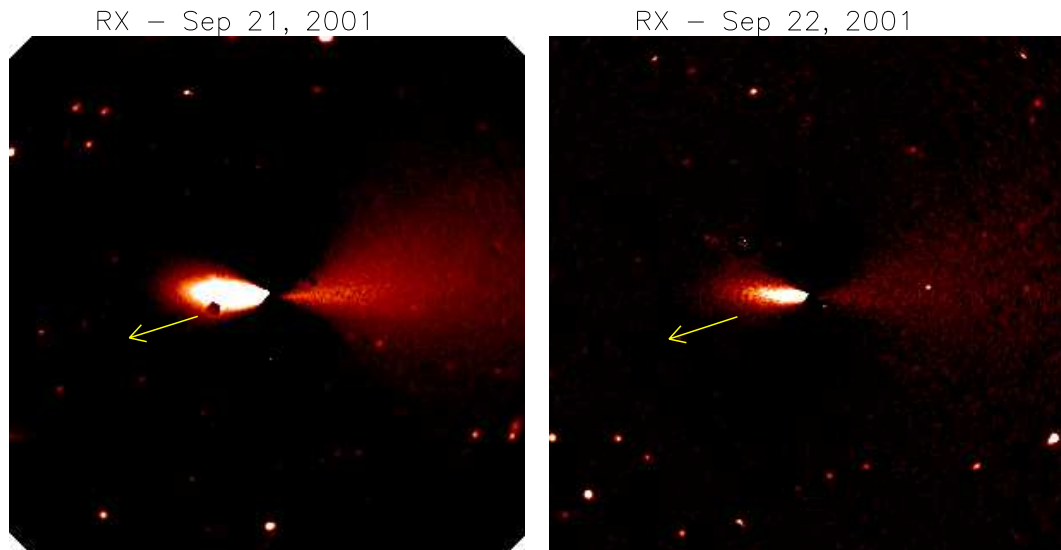
Figure 6.12: The azimuthal median technique has been applied on the broad band images to enhance Borrelly's in evident dust asymmetries. The left image was taken on the September 21, 2001. The right image was taken one night later, September 22, 2001. A strong linear dust stream pointing to the Sun is recognized on both images and a fainter dust stream on the anti sunward side. The projected direction of the Sun is indicated by the yellow arrow. North is on the top of the images and East on the left.
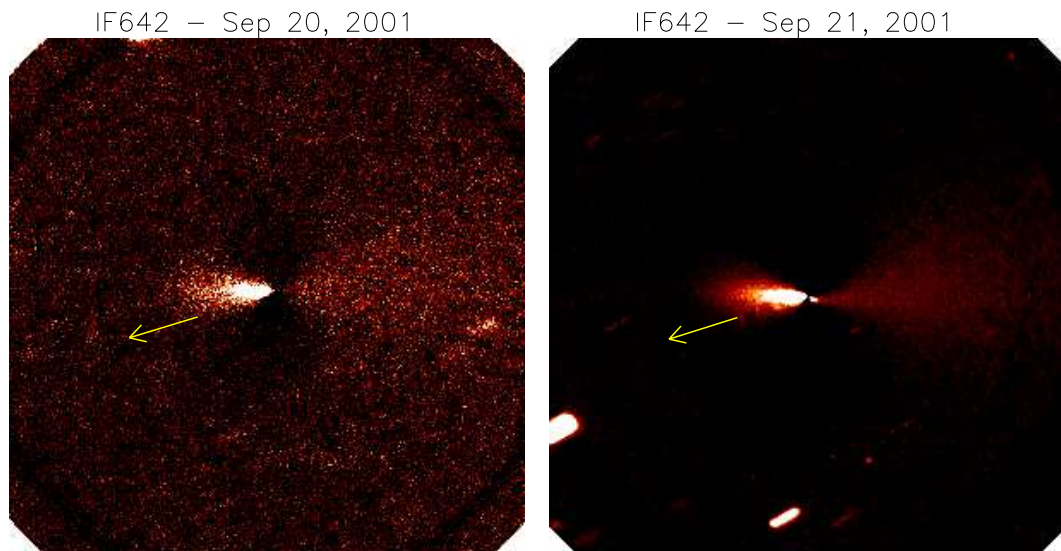
Figure 6.13: These images are processed by taking the IF642 images on the September the 20, 2001 and September, 21, 2001. The main dust emission on the sunward side is also identifiable on these images, whereby a small amount of dust is seen on the night side comparing with the RX images in Figure 6.12. The projected Sun's direction is indicated by the yellow arrow. North is on the top of the images and East on the left.

Chapter 7

Model of Outer Dust Coma and Tail

The emission of dust from a comet nucleus and its acceleration by expanding gas in the circumnuclear environment has been treated in a number of theoretical works and with the linear system model, which have been introduced in chapter 5. But this process takes place within a domain which is not resolved in ground based imaging.

Farther out, where ground based resolution becomes adequate, the grain flow can be modeled by radial expansion, influenced by solar radiation pressure. Although the emission of material from the nucleus is not spherically uniform, the resulting deviation from symmetry in the inner coma tends to be small but nevertheless measurable.

The purpose of this chapter is to compare the Pik Terskol data with a model describing the outer dust coma and tail whereby the peculiar anisoptropic shape of Borrelly will be included. The first section will describe the physics acting on the dust particles after they have de-coupled from the gas. The orbital calculations of the particles will be explained. Afterwards follow the results of the model and the comparison with the observational data.

7.1   Model of the Dust Coma and Tail

After being released from the nucleus surface (section 5.1), the dust grains travel through a region where gas and dust interacts. At about 300 cometocentric distance (Gombosi *et al.*, 1986) the gas and dust become decoupled and both components approach their terminal velocities.

Beyond a distance of a few times 1000 km from the nucleus the influence of solar radiation pressure (F_R) on micrometer-sized particles becomes increasingly evident in the particle motion (Whipple, 1950).

For a spherical dust particle of radius a and density ρ_d at a heliocentric distance r, the two acting forces, radiation pressure and solar gravity (F_G), are expressed as

$$F_G = \frac{GM_\odot}{r^2} \left(\frac{4}{3}\pi a^3 \rho_d \right) \tag{7.1}$$

$$F_R = \frac{Q_{pr}}{c} \left(\frac{L_\odot}{4\pi r^2}\pi a^2 \right) \tag{7.2}$$

where $L_\odot$ is the solar luminosity and c is the speed of light. The efficiency factor for radiation pressure is expressed by Q_{pr}.

$$Q_{pr} = Q_{sca} \left(\frac{1}{\omega} - \langle \cos\theta \rangle \right) \tag{7.3}$$

where θ is the scattering angle. The term $\langle cos\theta \rangle$, also called the asymmetry parameter (Bohren and Huffman, 1983), accounts for the anisotropy of the scattered radiation. For forward scattering of the incident radiation $\langle cos\theta \rangle = 1$; for isotropic scattering $\langle cos\theta \rangle = 0$ while back scattering would have $\langle cos\theta \rangle = -1$. The parameters Q_{sca} and ω denotes the efficiency factor for scattering and the single scattering albedo, respectively. Q_{pr} depends on the particle radius a, the wavelength λ and the material properties of the dust (Burns *et al.*, 1979; Hellmich and Schwehm, 1983; and chapter 3).

Since both forces, F_G and F_R, are radial, opposite and vary with r^{-2}, a dust particle will follow a Keplerian trajectory corresponding to a reduced "effective" gravity field $(1 - \beta)F_G$ where

$$\beta = \frac{F_R}{F_G} = 0.585 \times 10^{-4} \text{kg m}^{-2} \frac{Q_{pr}}{\rho a} \tag{7.4}$$

is called the acceleration ratio. β does not depend on the distance from the Sun but only on particle properties.

The concept of the outer dust coma model is to follow the dust orbit after it has been released from the nucleus. The dynamical theory of the dust trajectory will be introduced in the following section. The parameters used for all models are the same. $N_d \times N_n \times N_t$ samples of dust grains are considered, whereby N_d is the number of dust sizes considered in the simulations, N_n denotes the number of grains of a fixed size either emitted uniformly or anisotropically according to the emission features, and N_t is the time interval of the dust ejection.

In the model N_n particles are emitted into a randomly distributed direction, either isotropically or within a 3D-Gaussian cone with assumed orientation and FWHM. It has been shown in the previous chapter that Borrelly's dust emission

is characterized by a dominant jet, which is ejected close to the pole in the sunward direction. This jet is initially assumed to explain the elongated dust coma seen on the Earth based observations (see chapter 6). To include this emission in the outer dust coma and tail simulation the cone will be positioned at the nucleus rotation pole.

The model includes a particle size range of 0.1 μm to 5 mm. The latter is the largest grain which can be lifted from the nucleus surface. This size range has been divided into 85 size bins (N_d) and $N_n = 200$ particles are emitted per size bin in equidistant intervals of the comet's true anomaly. In each simulation the emission starts 60 days before the date of observations, and 200 emission events, N_t, are considered. The particle sizes are distributed according to Equation 3.25.

The simulation provides the spatial distribution of the number of particles N projected on sky plane for 85 particle size bins. To calculate the surface brightness, $B(x, y)$, from this spatial distribution, the particle number distribution has to be combined with the particle size distribution, $n(a)$ (Eq. 3.25), and the brightness of the particles, $Q_{sca}\pi a^2 P(\theta)$, so that

$$B(x, y) \propto \int_{a_{min}}^{a_{max}} Q_{sca}\Phi(\theta)N\pi r^2 n(a)da \qquad (7.5)$$

(Bonev *et al.*, 2001). $\Phi(\theta)$ is the phase function at the scattering angle θ of the observations. Q_{sca} has been calculated for an ensemble of non-spherical particles between $a_{min} = 0.1$ μm and $a_{max} = 0.005$ m and a size distribution $n(a)$. $\Phi(\theta)$ and Q_{sca} are presented in section 3.4.4.

7.1.1 Theory of Motion

The orbit of the dust grains can be solved by the inverse problem of Kepler's equations. If $\vec{r}$ and $\dot{\vec{r}}$ is given at some time $t = t_0$ then the orbital elements of the dust trajectories can be computed and the location of the grains can be propagated for any time. The semimajor axis of the dust particles is

$$\frac{1}{a} = \frac{2}{|\vec{r}|} - \frac{|\dot{\vec{r}}|}{\mu GM} \qquad (7.6)$$

$\mu = 1 - \beta$ describes the reduced gravitational force on the particles. If $a > 0$ then the orbit is an ellipse. If $a < 0$ then the orbit is a hyperbola. The angular momentum per unit mass, $\vec{L}$, is equal to the cross product of the heliocentric radius vector and the velocity vector at the apsidal endpoint: $\vec{r} \times \vec{v}$. The angular momentum is a conserved quantity and the components of $\vec{L}$ are constant for the entire transfer orbit. i.e. (Taff, 1985).

$$\begin{pmatrix} L_x \\ L_y \\ L_z \end{pmatrix} = \begin{pmatrix} yv_z - zv_y \\ zv_x - xv_z \\ xv_y - yv_x \end{pmatrix} = L \begin{pmatrix} \sin i \sin \Omega \\ -\sin i \cos \Omega \\ \cos i \end{pmatrix} \tag{7.7}$$

Two intermediate quantities are obtained

$$p \;\; = \;\; \frac{L^2}{\mu GM} \tag{7.8}$$

$$q \;\; = \;\; xv_x + yv_y + zv_z \tag{7.9}$$

The eccentricity of the orbit is defined as

$$e = \left(1 - \frac{p}{a}\right)^{\frac{1}{2}} \tag{7.10}$$

thus the eccentricity < 1 if the orbit is ellipsoid and > 1 if it is hyperbolic. If the orbit is an ellipse, the eccentricity can be written as

$$e_x \;\; = \;\; 1 - \frac{r}{a} \tag{7.11}$$

$$e_y \;\; = \;\; \frac{q}{\sqrt{aGM}} \tag{7.12}$$

The inclination i is obtained by solving Equation 7.7

$$i = \arccos\left(\frac{L_z}{L}\right) \tag{7.13}$$

similarly to the longitude of the ascending node, Ω, can be found from

$$\Omega = \arctan\left(\frac{L_x}{-L_y}\right) \tag{7.14}$$

The next element which need to be determined is the argument of perihelion, ω. For this the true anomaly, θ, will be required.

$$\theta_x \;\; = \;\; \frac{L^2}{r\mu GM} - 1$$

$$\theta_y \;\; = \;\; \frac{Lq}{r\mu GM}$$

$$\theta \;\; = \;\; \arctan(\theta_y, \theta_x) \tag{7.15}$$

Now the following intermediate relations are introduced:

$\cos(\omega + \theta) = (x \cos \Omega + y \sin \Omega)/r$
If $i = 0$ or $i = \pi$ then $\sin(\omega + \theta) = (y \cos \Omega - x \sin \Omega)/r$
If i is neither 0 nor π then $\sin(\omega + \theta) = z/(r \sin i)$

and the argument of perihelion is obtained via

$$\omega = \arctan \left(\frac{\sin(\omega + \theta)}{\cos(\omega + \theta)} \right) - \theta \tag{7.16}$$

where θ is the true anomaly of the object's current position in its orbit. The true anomaly is zero at perihelion, but it will be π radians at aphelion. ω has to be corrected to the interval $[0, 2\pi)$ if necessary.

Finally the time of perihelion passage, T, is needed. For that the mean motion is defined as

$$n = \sqrt{\frac{\mu G M}{a^3}} \tag{7.17}$$

whereby n has to be adjusted depending if it is a ellipsoid or a hyperbolic orbit.

Elliptical orbits

If the orbit is an ellipse, the eccentric anomaly, E, is found from

$$E = \arctan \left(\frac{e_y}{e_x} \right) \tag{7.18}$$

and the mean anomaly, M, is found from Kepler's equation:

$$M = E - e \sin E \tag{7.19}$$

T is also derived by Kepler's equation

$$T = t - \frac{M}{n} \tag{7.20}$$

the unit of the mean motion [rad/day] or [rad/s] should be chosen according to the time units used for T and t.

Hyperbolic Orbits

If the orbit is a hyperbola, the eccentric anomaly is found from

$$H = \text{arccosh} \left(\frac{e + \cos \theta}{1 + e \cos \theta} \right) \tag{7.21}$$

The mean anomaly is derived from the hyperbolic orbital equation

$$M = e \sinh H - H \tag{7.22}$$

and the time of perihelion passage, T, is obtained by the same relationship used for the elliptical orbit (see Eq. 7.18).

When all orbital elements $(a, e, i, \omega, \Omega$ and $T)$ are known, the position of each particle at a given time t can be propagated with its Keplerian motion. The position vector $\vec{r}$ at time of emission, t_e, of the dust grains is assumed to be the position vector of the cometary nucleus at time t_e. The dust grain velocity vector $\vec{V_d}$ of a given grain size is calculated by the relation taken from Fulle (1989).

$$\vec{V_d} = \vec{V_c} + v(1-\mu)^{(1/k)}\vec{u_q}; \qquad q = 1...N_s \tag{7.23}$$

where $\vec{V_c}$ is the Keplerian velocity vector of the cometary nucleus, $\vec{u}$ denotes the unit vector along the ejection velocity and v the dust ejection velocity. v is considered to be the terminal velocities given in Figure 4.15. k should range between 4 to 6 as discussed by Fulle (1989).

7.2   Model and Observation - a Comparison

To define the orientation of the sunward side dust Gauss-cone, the spin axis of Borrelly has to be determined. Several authors have determined the pole orientation of Borrelly and their results are in Table 7.1. They range between $\alpha = 225 \pm 15°$ and $\delta = $ -10 $\pm$ 10° .

References	α	δ
Thomas et al. (2001)	233	-18
Samarasinha and Mueller (2002)	221	-7
Schleicher et al. (2003)	214.1	-5.7

Table 7.1: P/Borrelly's spin axis determinations of several authors. (α, δ) are the equatorial coordinates of the pole.

For the model of Borrelly, two dust grains compositions are considered: pure silicate and silicate core-amorphous mantle particles. The main jet has been modeled with a Gauss-cone, positioned 7° away from the pole orientation and with a FWHM of 25°. Further two broader dust fans of 50° FWHM have been included. They are 18° and 25°° away from the pole. Figure 7.1 gives the

contour plot of the observation, image BOR64201, and the simulated coma containing pure silicate particles and Fig. 7.2 a coma of silicate core-amorphous mantle particles. The particle's porosity is P = 0.69. The contour plots have been normalized. The images have been divided by their maximum brightness and multiplied by a factor of 512. The scale of the contour plot follows 2^x with x = 0...8.

The main jet, 25° FWHM, contributes with 40% and the two fans of 50° FWHM with 30% each to the total dust coma. This combination could provide a reasonable fit to the observed shape of Borrelly's dust coma. The MICAS data gives a 3:1 ratio of the projected dayside to nightside emission. The dayside contribution is therefore $\approx$ 75%. A direct comparison cannot be made between the contribution of the emissions for the ground-based observational model and the one obtained from the MICAS data because the model did not include an nightside "emission". But for both cases, most of the dust grains are ejected from the dayside.

To provide a reasonable fit and to obtain Borrelly's characteristic sunward elongation, the dust in the main jet have to be $\approx 1.4 - 1.7\times$ higher than the dust in the fans. Further have the core-mantle particles to faster than the pure silicate particles for comparable sizes, because they are stronger influenced by the solar radiation pressure than the pure silicate grains (Eq. 7.3).

A pole orientation of $\alpha = 235°$ and δ = -16° has been determined for the model, which is in good agreement with the values of the other authors.

The observed inner dust coma is nearly isotropic and the sunward elongation of Borrelly increases with increasing distance from the nucleus. It has been mentioned in the previous section that the center of the coma is not well resolved because of seeing, telescope tracking and spatial quantization of the images. Therefore the model will show a steeper density gradient than the observed coma.

At the outer margin of the coma, the observed density gradient is steeper than the model's. The main influence for this could be attributed to the radiation pressure acting on the dust grains. In this work Q_{pr} has been considered to be a constant value for all particles sizes. But it is known that the radiation pressure depends not only on the dust composition but also on the grain radius (Burns *et al.*, 1979; Hellmich and Schwehm, 1983). Therefore an improved fit of the modeled dust coma with the observed one will be expected for size dependent Q_{pr}.

Fig. 7.3 gives the distribution of the dust particles according to their size ranges for the above mentioned Gaussian jet. The color coding refers to Σ, where Σ is the total scattering area of the particles in each particular range of size. It can be
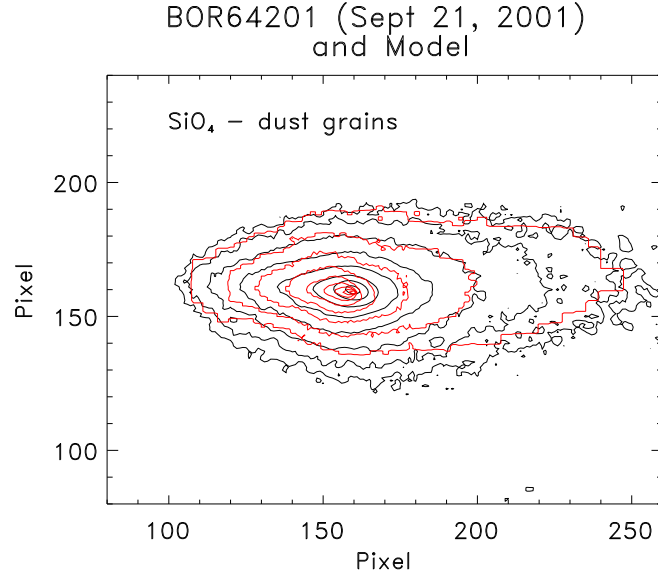
Figure 7.1: This is the contour plot of BOR64201 (——) and the modeled dust coma (- - -) of SiO$_4$ particles with a gauss jet of 25° FWHM and 7° away from the pole orientation. ($\alpha = 235$°, $\delta = -16$°). The projection of the Sun-comet vector is ≈ 18° above the horizontal line to the left.
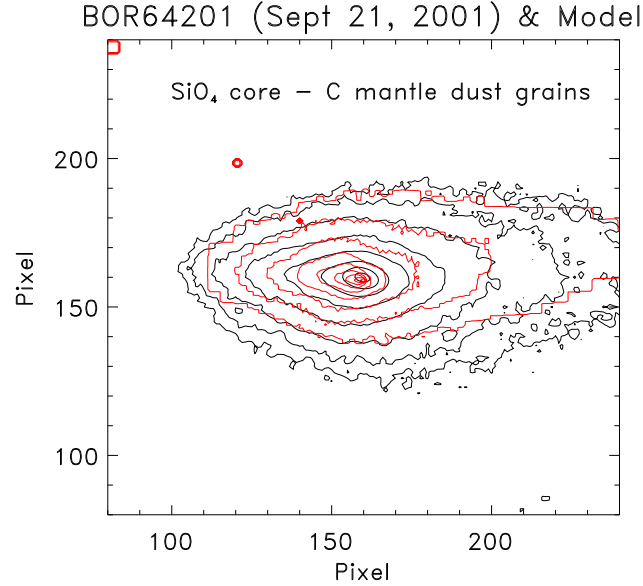
Figure 7.2: This is the contour plot of BOR64201 (——) and the modeled dust coma (- - -) of SiO$_4$ core-carbon mantle particles with a gauss jet of 25° FWHM and 7° away from the pole orientation. ($\alpha = 235$°, $\delta = -16$°). The projection of the Sun-comet vector is ≈ 18° above the horizontal line to the left.

seen that the jet towards the sun is formed by particles between $1 \cdot 10^{-7}$ - $1 \cdot 10^{-5}$ m which are also the fastest particles ($1000 \le v_d \le 160$ m/s). The intermediate size particles $70 \le v_d \le 160$ m/s also give a sunward fan, which is less collimated compared to the smaller particles. The bigger particles and therefore the heaviest particles generate a more isotropic dust coma $8 \le v_d \le 70$ m/s.
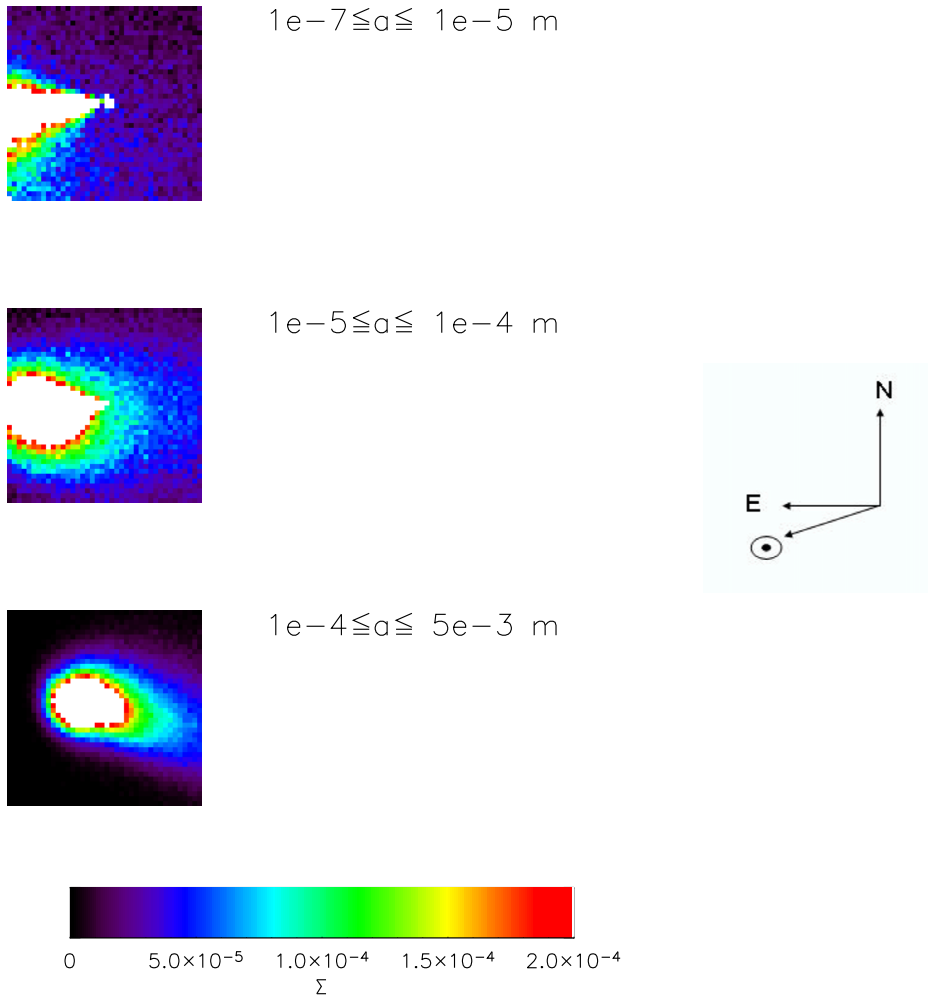
Figure 7.3: The distribution of dust silicate core-amorphous carbon grains at three different size bins ($1 \cdot 10^{-7}$ - $1 \cdot 10^{-5}$ m; $1 \cdot 10^{-5}$ - $1 \cdot 10^{-4}$ m and $1 \cdot 10^{-4}$ - $5 \cdot 10^{-3}$ m). The color coding refers to the total scattering area Σ. The direction of the Sun, North and East are given.

In summary it can be said that the elongated dust coma of Borrelly, observed on the Earth based images can be attributed to the main jet seen on the MICAS data. A Gaussian jet positioned closed to the pole orientation was able to reproduce the peculiar shape of Borrelly. A perfect agreement with the observations could

not be obtained. The MICAS data show that the emission distribution is more complex than assumed here and this obviously has influence on the observed structure. Changes in the radiation pressure efficiency, Q_{pr}, with grain radius might also improve the fit.

Chapter 8

Summary and Conclusion

The dust coma of comet 19P/Borrelly has been analyzed based on images obtained from the MICAS (VISCCD) onboard the Deep Space 1 spacecraft. Near simultaneous ground-based observations were obtained from the observatory of Pik Terskol, and have also been analyzed. To support the analysis, two models have been developed which simulate the dust coma in the circumnuclear environment. For comparison, data of comet 1P/Halley have been investigated in a similar manner.

In MICAS data the inner dust coma is dominated by dust jets leaving the nucleus surface. The dimensions and position angles of these jets have been determined. The dust outflow has been investigated, whereby differences between Halley and Borrelly were observed in the variation of brightness with distance. By integrating around the nucleus a quantity, $\oint Ids$, has been obtained, where I is the intensity and s is the distance. $\oint Ids$ should be a constant for force-free radial outflow of an optically thin, non-fragmenting dust emission. However, the quantity decreases with increasing distance to the nucleus for Borrelly. In comparison Halley's $\oint Ids$ increases, indicating that different physical processes dominate in the vicinity of Halley's nucleus.

The analysis of the MICAS data combined with the Superpositioning Dust Jet Model (SDJM) have shown that Borrelly's dust emission can be understood as dust jets emanating from active regions distributed on the nucleus surface which form together prominent features such as the main jet, and the observed fans. However not all dust features could be reproduced with the SDJM. The scheme of fitting the emissions requires that the axis of symmetry of the individual jets is normal to an idealized surface (ellipse). It is apparent that although the scheme reproduces the inner coma fairly well, there are significant departures from the assumption (i.e. jet structures which are not aligned parallel to the idealized surface normal).

The dust on Borrelly's nightside can be attributed to lateral dust flow being

swept from the dayside (Keller and Thomas, 1989; Knollenberg, 1994), which also would explain the observed differences between the nightside and dayside radial profiles. Therefore SDJM is limited because its approach is based on dust jets which are assumed to be ejected perpendicular or close to perpendicular to the line of sight. However, SDJM is able to constrain the physics which influences Borrelly's dust outflow. By including acceleration and superimposed jets, the model could fit the observed $\oint Ids$ reasonably well and could constrain possible explanations for the increase of $\oint Ids$ with decreasing distance to the nucleus. Particle fragmentation is not needed to explain the observed intensity profile in the first km away from the nucleus. Dust acceleration contributes significantly to the observed increase of $\oint Ids$ close to the nucleus surface, but the SDJM showed that a combined effect of acceleration and distributed jets was able to fit best the observations.

Halley's inner dust coma could not be reproduced with the SDJM approach. This can be explained by a optical thick inner coma and/or particle fragmentation into optically large particles. Both these processes can explain the flattening of $\oint Ids$ close to the nucleus surface. With a dust production rate of $2.17 \cdot 10^4$ kg/s derived by Keller and Thomas (1991) a maximum optical depth of about 1 was obtained < 1 km away from the nucleus. Beyond this distance the optical thickness decreases continuously. The optical depth of the dust coma has been calculated assuming an isotropic dust outflow. For a non radial-symmetric coma, see Müller (1999), these values can change. However they are strongly dependent upon the dust size distribution.

The $Af\rho$ (see section 4.3) of Halley at a distance of 600 km away from the nucleus is about $1.8 \cdot 10^4$ cm. Considering an photometric error of $\approx 10\%$ inherent in the relative calibration of the data sets, it can be concluded that the value agrees reasonably with the one obtained by Schleicher *et al.* (1998) for March 1986, $Q_d = 2.04 \cdot 10^4$ cm.

The expected reflectivity of Borrelly's dust has been calculated for a given dust production rate and compared with the observed reflectivity. A good fit of the modeled reflectivity with the observed one has been obtained with dust production rates between $Q_d \simeq 200$ - 250 kg/s and particle porosity of $P \approx 0.86$ for silicate, core-mantle and 2-component mixed grains and the particle size distribution of Hanner *et al.* (1985). The good agreement between modeled and observed reflectivity has also been obtained with $Q_d \simeq 300$ - 350 kg/s and $P = 0.68$ for the mentioned dust grain compositions. The former given porosity is in good agreement with the one suggested by Li and Greenberg (1999) for Borrelly's core-mantle dust grains. The derived dust production rates agree well with the values found by Lamy *et al.* (1998), $Q_d \simeq 185$ - 215 kg/s, and Newburn *et al.* (1989), $Q_d \simeq 335$ kg/s for Borrelly.
With a dust production rate of 200 - 350 kg/s and a gas production rate of 3

$\cdot 10^{28}$ molecules s^{-1} (Weaver *et al.*, 2003), a dust to gas ratio of $\chi = 0.25$ - 0.4. This agrees well with the ratio of 0.4 derived in section 4.2.2.

The $Af\rho$ also has been derived for Borrelly from the *in situ* and from the Earth observations. These values disagree by a factor of two. Given that an identical approach for the analysis of comet Halley has been used, this is hard to explain. Three possibilities are proposed.
Firstly, they may be a systematic calibration error in the MICAS images.
Secondly, the $Af\rho$ in MICAS data was measured at only 40 km from the nucleus. The signal level beyond this distance was too low. For Halley, the value of $Af\rho$ increased with distance from the nucleus out to around 100 km before reaching a constant value. This was possibly caused by optical depth effects although Thomas and Keller (1991) considered particle fragmentation as a more likely reason based on the dust size distribution of McDonnell *et al.* (1990). In the case of comet Borrelly, optical depth effects are unimportant. But particle fragmentation may continue out to larger distances at Borrelly.
Thirdly the lower $Af\rho$ value of Halley at distance within 40 km away from the nucleus compared to the final value at 500 km could also be attributed to anisotropic outflow, which also might play a role in the determination of the *in situ* $Af\rho$ for Borrelly. Some combination of these three possibilities cannot be ruled out.

The dust outflow along the main jet observed on the MICAS images can be thought of as constant for the duration of the observation. Unfortunately the "far" images from MICAS, which should have given the dust coma up to 300 km away from the nucleus, are so poorly calibrated and an analysis of the data cannot be performed. The resolution closer to the nucleus (< 3000 km) of the Earth observations is also limited, but, in this case, by of observational conditions.

The observed brightness in the inner dust coma could be well fitted with the particle size distribution of Hanner *et al.* (1985). The SDJM was also able to reproduce the increased $\oint Ids$ close to the nucleus surface with the dust velocities of 0.54 μm grains, taken from the 2D-axissymmetric model of Combi and Tenishev (2003).
The reddening of Borrelly's dust coma is around 2 %/1000Å close to the center of the coma which is an indication of the presence of small grains.

The observations of O ^{1}D towards show anisotropic emission suggesting that the dust jet anisotropy is driven by gas emission anisotropy. Schleicher *et al.* (2003) reported an anisotropic emission of CN towards the Sun. The source of CN is inferred to be dust (A'Hearn *et al.*, 1995). Therefore a connection between the elongated sunward dust emission, the CN and O ^{1}D can be inferred.

Models of Borrelly's dust coma seen from the Earth have shown that an anisotropic dust emissions of Gaussian profile is able to reproduce the observed elongated

shape of the coma. The pole orientation has been determined to be $\alpha = 135°$ and $\delta = -16°$. The Gauss-jet is $7°$ away from the pole with $25°$ FWHM, points towards sun direction and is supposed to represent the main jet observed on MI-CAS. To be able to reproduce a similar coma shape like the one observed, two further dust fans, also of Gaussian profiles but with $50°$ FWHM are needed. The dust particles in the jet are about 2 times faster than the one in the fan emissions. Still a best fit has to be achieved. An optimization of the fit is complex and remains to be completed as future works.

Further modeling of the dust coma of comet Borrelly with better defined input parameters will improve the characterization of its dust coma and add further information to a broader understanding of cometary dust comae. But more *in situ* data are needed to improve the understanding of the inner dust coma of a comet and to allow a direct comparison with observations performed from the Earth.

An improved knowledge of the dust environment is also necessary for ESA's cornerstone mission, Rosetta, which successfully lifted off from Kourou, French Guiana, at 04:17 local time (08:17 CET) on 2 March 2004. It will reach comet 67P/Churyumov-Gerasimenko in 2014. The spacecraft comprises a large orbiter, which is designed to operate for a decade at large distances from the Sun, and a small lander. Each of these carries a large complement of scientific experiments designed to complete the most detailed study of a comet ever attempted. After entering orbit around comet Churyumov-Gerasimenko (C-G), the spacecraft will release a small lander onto the icy nucleus, then spend the next two years orbiting the comet as it heads towards the Sun. OSIRIS, the main imaging system onboard the orbiter, will perform observations of the innermost coma throughout this phase. Simultaneous ground-based observations will provide a link between near-nucleus observations and the other coma so that, in future, we can hope to estimate changes in the outgassing properties of the nucleus from low resolution ground-based data.

This work has shown that while the physics needed to understand the outflow is fairly well established, in detail there remain practical difficulties in constraining models of the innermost coma and their extrapolation to scales of several tens of thousands of kilometers from the nucleus.

Appendix A

Publications

A.1   Comparative study of the dust emission of
      19P/Borrelly (Deep Space 1) and 1P/Halley,
      Advances in Space Research, 31, 2583-2589,
      2003.

COMPARATIVE STUDY OF THE DUST EMISSION OF 19P/BORRELLY (DEEP SPACE 1) AND 1P/HALLEY

T. M. Ho[1], N. Thomas[2], D. C. Boice[3], C. Kollein[1], L. A. Soderblom[4]

[1]MPI fuer Aeronomie, Max-Planck-Strasse 2, 37191 Katlenburg-Lindau, Germany
[2]Physikalisches Institut, Universitaet Bern, Sidlerstrasse 5, CH-3012 Bern, Switzerland
[3]SWRI, 6220 Culebra Road, San Antonio, Texas 78228-0510, United States
[4]USGS, Flagstaff, 2255 N Gemini Drive, Flagstaff, Arizona 86001, United States

ABSTRACT

Images obtained by the Miniature Integrated Camera and Imaging Spectrometer (MICAS) experiment onboard the Deep Space 1 spacecraft which encountered comet 19P/Borrelly on September 22nd 2001 show a dust coma dominated by jets. In particular a major collimated dust jet on the sunward side of the nucleus was observed. Our approach to analyse these features is to integrate the observed intensity in concentric envelopes around the nucleus. The same procedures has been used on the Halley Multicolour Camera images of comet 1P/Halley acquired on March 14th 1986. We are able to show that at Borrelly the dust brightness dependence as a function of radial distance is different to that of Halley. At large distances both comets show constant values as the size of the concentric envelopes increases (as one would expect for force free radial outflow). For Halley the integral decreases as one gets closer to the nucleus. Borrelly shows opposite behaviour. The main cause for Halley's intensity distribution is either high optical thickness or particle fragmentation. For Borrelly, we have constructed a simple model of the brightness distribution near the nucleus. This indicates that the influence of deviations from point source geometry is insufficient to explain the observed steepening of the intensity profile close to the nucleus. Dust acceleration or fragmentation into submicron particles appear to be required. We also estimate the dust production rate of Borrelly with respect to Halley and compare their dust to gas ratios. © 2003 COSPAR. Published by Elsevier Ltd. All rights reserved.

BACKGROUND

Deep Space 1 (DS1) made its closest approach to the nucleus of comet 19P/Borrelly on September 22nd 2001 at 22:30 UT. The fly-by distance was 2174 km on the sunward side. The relative velocity at the time of encounter was 16.58 km s^{-1}; the phase angle of the approach was 88°. The comet was 1.36 AU away from the Sun and 1.47 AU from the Earth. A description of the first results of the MICAS (Miniature Integrated Camera and Imaging Spectrometer) experiment has been presented in Soderblom et al. (2002). Further results on the observed dust distribution were given in Boice et al. (2002). In this paper, we present an analysis of the intensity profiles in the inner coma of Borrelly and compare these with observations of the inner coma of comet 1P/Halley acquired during the Giotto encounter.

DATA ANALYSIS

Available Data Sets

We used the Standard Level 1 data set from the United States Geological Survey. These data have been absolute calibrated in units of reflectivity with an accuracy of ≈ 20%. For comparison we have analysed images of comet Halley obtained on 13 - 14 March 1986 by the HMC (Halley Multicolour Camera) onboard Giotto. The distance between the Sun and Halley was 0.89 AU and the Earth-comet distance was 0.96

AU at the time of the Giotto encounter. The phase angle was 107°. These data have also been absolute calibrated and are available through the Planetary Data System (Keller et al., 1996).

Dust Emission

On all MICAS images, a non-isotropic emission is observed which is illustrated by plotting the azimuthal intensity distribution around Borrelly's nucleus (see Figures 1 and 2). A fit using three Gaussians has been made to the azimuthal distribution following Reitsema et al. (1989). Thus the full width half maximum (FWHM) of the observed emission features could be determined. The resulting parameters of the fit are shown in Table 1.
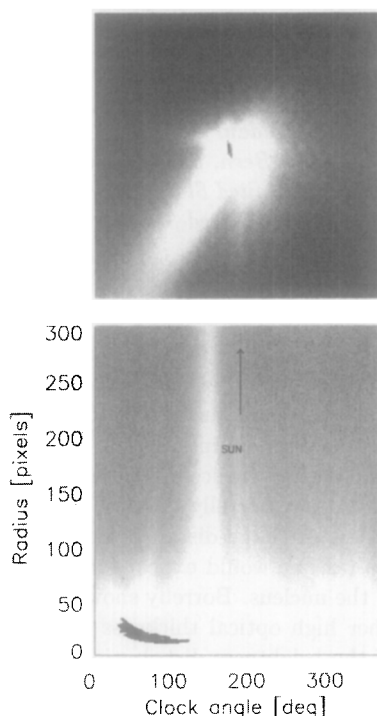
Fig. 1. The upper image is MID3.2 acquired by MICAS seven minutes before closest approach (range=7150 km, 1 pixel ≈ 0.093 km). The field of view is ≈ 50 x 50 km. The nucleus was deliberately saturated to enhance the dust emission (black stripes indicate saturated data). Below a polar projection about the nucleus centre of this image is shown. The Sun direction is indicated by the arrow. Several linear features (jets) can be seen.
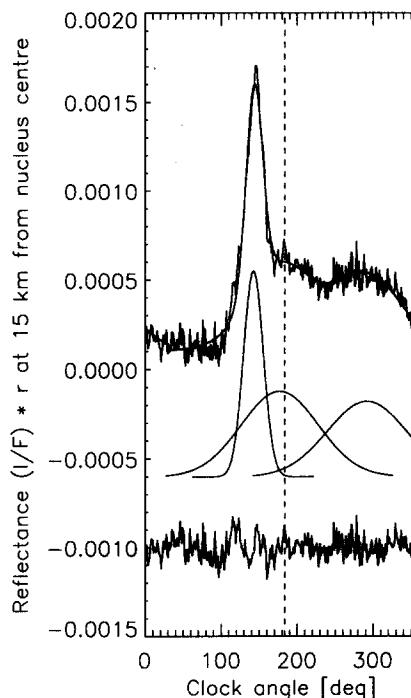
Fig. 2. This plot shows the azimuth brightness distribution at 15 km above the assumed nucleus centre of Borrelly and the fitted Gaussians. The fit parameters are presented in Table 1. The lowest plot is the residual. The fitted Gaussian and the residual have been offset by -6×10^{-4} and -1×10^{-3} respectively for clarity. The direction of the Sun is indicated by a dashed line.

The Gaussian representing the main jet on the dayside appears narrow and collimated superimposed over a broader emission. Despite the fact that it is the most dominant feature seen on the images, its contribution to the total emission is relatively low (see Table 1). Because of the uncertainty of the background level in the analysis, we also present the relative strengths of the jets compared with the total emission of all jets. The ratio of the projected dayside to nightside emission is estimated to be $3.3 \pm 1.0 : 1$. The amount of dust over the nightside is surprisingly high although the features on the dayside seem to be so dominant

Table 1. Results of the azimuthal intensity distribution fit are shown in Figure 2. The Sun's clock angle ≈ 177°

Emission	Clock angle on image [deg]	FWHM [deg]	Contribution to total emission (%)	Contribution to total jet emission (%)
Jet1	142	18	19	24
Jet2	177	72	31	40
Jet3	292	74	28	36
Constant	–	–	23	–

on the images. This does not, however, imply necessarily nightside activity. Hydrodynamical expansion of the gas which drags dust particles from the sunward-facing active regions across the projection of the terminator could explain these observations (Keller and Thomas, 1989 & Knollenberg, 1994). A dayside : nightside asymmetry ratio of 3.2 :1 was observed at Halley from a similar phase angle.

Jet Dimension

Because of the elongated shape of the nucleus (roughly 4 km x 8 km in projection) the images have been transformed into a coordinate system based upon an ellipse centred on the nucleus. Figure 3 shows the intensity profile on a mininum size ellipse surrounding the nucleus but without intersecting it. We have fitted this plot with four Gaussians to obtain an objective measure of the width of the observed jets near their bases. The width for the main jet on the sunward side of the nucleus seen in MICAS images has a FWHM of about 3.07 km. The FWHM of the emission on the nightside is 3.11 km. That of the weaker dust fans is around 0.51 and 0.93 km. These values probably comprise an upper limit to the actual width of the emitting region, because of the rapid lateral expansion immediately above the source. In this plot four emission features are identified while Figure 2 shows only three. The reason is that fan No. 2 diverges at higher altitude and gets fainter.
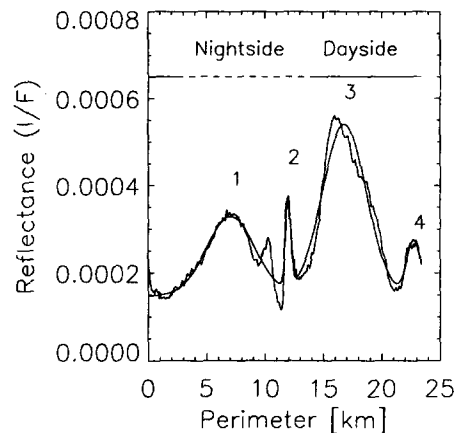
Fig. 3. Intensity along an ellipse surrounding the nucleus. The projected day- and nightside hemispheres are marked. A fit to the data has been superimposed. The emission features are nummbered.

Dust Outflow

To examine the dust outflow of the comet we approximate the nucleus as an ellipse and assume that the gas/dust sources are situated on the surface of this ellipse. Further we assume a continuous constant emission of dust from these sources. If this outgassing expands radially without being influenced by any forces, the dust flux in concentric envelopes remains constant. If we integrate the intensity, I, around an envelope, the quantity $\oint I ds$ (where s represents the distance around the perimeter of the envelope) should be constant with increasing radial distance to the nucleus surface for free radial dust outflow. Thus a variation of this integral will indicate sources, sinks, or changes in the scattering or flow characteristics of the dust (Thomas and Keller, 1990).

We applied this method to analyse and compare the dust outflow behaviour of Borrelly and Halley. Borrelly's integral, $\oint I ds$, increases with decreasing distance to the nucleus surface, while Halley's decreased (see Figure 4). One can interpretate this in terms of deviations from 1/r dependence of intensity. Halley's

1/r profile flattens close to the nucleus (Thomas et al., 1988); Borrelly's steepens. There are several possible explanations for this observation. A high optical depth above active regions can flatten 1/r profiles close to the nucleus and would be a plausible explanation for Halley. Also fragmentation into optically large particles can cause similar behaviour of the intensity because of the change in the scattering area at visible wavelengths (Thomas et al., 1988). Earlier observations of Halley have detected a high amount of large dust particles (Fulle et al., 2000), thus this fragmentation process is possible. In Borrelly's case, particles fragmentating into submicron size would explain a decrease of the integral with distance. These particles would not contribute to the scattering process at large distances and the intensity will drop. Soderblom et al. (2002) also suggested that Borrelly's dust particles seem to be small. Another potential reason for Borrelly's behaviour is dust acceleration which steepens the intensity profile near the nucleus, because of the increasing dust number density. Also the existence of distributed sources on the nucleus surface might influence the intensity profile (see below).
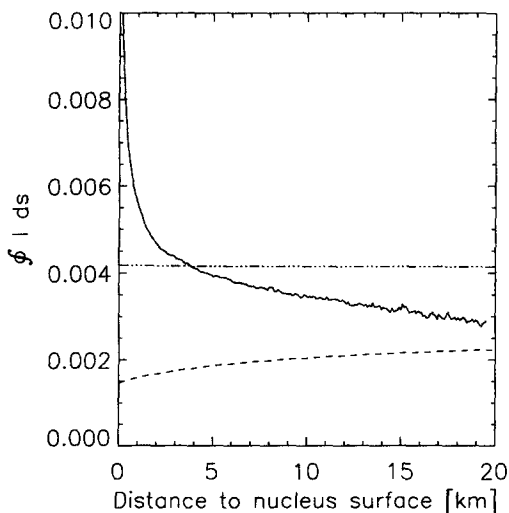
Fig. 4. The integrated intensity along equidistant envelopes is plotted for Halley (- - -), Borrelly (——) and the model of Borrelly (— - -). This plot shows Halley's integral, $\oint I ds$, divided by 48.

Dust to Gas Ratio

In Figure 4 Halley's integrated intensity $\oint I ds$ has been divided by 48, which is approximately the ratio of the dust emission brightnesses at large cometocentric distances. The dust production rate ratio is even greater because the dust outflow velocity at Halley was almost certainly higher than at Borrelly. Models by Gombosi et al. (1986) indicate $v_{Halley} \approx 200$ m/s and $v_{Borrelly} \approx 120$ m/s for micron-sized particles. Consequently the production rate ratio could be as large as 80:1. The H_2O production rate of Borrelly at DS1 encounter was 3.5×10^{28} molecules/s (Stern et al., 2002). That of Halley at Giotto encounter was 5.2×10^{29} molecules/s (Festou et al., 1986). Therefore, if the dust size distribution for the two comets were similar then the dust/gas ratio (χ) of Halley was about five times that of Borrelly. McDonnell et al. (1990) gave a dust to gas ratio for Halley of 2 and hence, we estimate that for Borrelly, $\chi = 0.4$. A'Hearn et al. (1995) gave $\chi = 1.16$ for Borrelly (assuming that an $Af\rho$ of 1000 cm is roughly the dust production rate in metric tons/s). Their value for Halley was 1.6.

DUST EMISSION MODELING

Model

To be able to study the dust emission in more detail, to constrain possible physics behind it and to determine the sources on the nucleus surface, we introduce a new analysis method. Based on Kitamura's hydrodynamic models (1986 & 1987) of isolated dusty gas jets, we approximate the dust emission as jets with Gaussian intensity profiles. This is a simplified model of the outgassing features, in which dust emission is assumed to undergo force free outflow within a fixed opening angle from individual sources. Thomas et al. (1988) already suggested a similar approach with dust cones to explain the intensity profiles around the nucleus of comet Halley. We simulate the observed emission with superimposed Gauss - shaped jets emitted from an elliptical nucleus and compare the resulting brightness distribution. The jets emit with a fixed opening angle from point sources distributed over the nucleus. These multiple discrete sources themselves form active areas. This approach differs from the assumption of Crifo et al. (1999) who created the dust

and gas emissions as fluids described by hydrodynamic equations. Due to gas and dust interaction complex patterns are formed in the coma. We avoid this complex scenario by simply superimposing all jets. Our result is a 2D array of superimposed jets which forms a brightness map of the first 30 kms around the nucleus. We can write each signal as a sum of weighted source terms depending on the opening angle of the jets and their positions. Thus we can set up a linear system of equations (see Eq. (1)).

$$\rho_{0,0}\frac{Q_0}{4\pi v_0} + \rho_{0,1}\frac{Q_1}{4\pi v_1} + \cdots + \rho_{0,n}\frac{Q_n}{4\pi v_n} = S_0$$

$$\rho_{1,0}\frac{Q_0}{4\pi v_0} + \rho_{1,1}\frac{Q_1}{4\pi v_1} + \cdots + \rho_{1,n}\frac{Q_n}{4\pi v_n} = S_1$$

$$\quad (1)$$

$$\cdots\cdots\cdots\cdots\cdots\cdots\cdots\cdots\cdots\cdots\cdots\cdots$$

$$\rho_{n,0}\frac{Q_0}{4\pi v_0} + \rho_{n,1}\frac{Q_1}{4\pi v_1} + \cdots + \rho_{n,n}\frac{Q_n}{4\pi v_n} = S_n$$

where:

$$\rho = 2 \cdot \int^{l_1} \frac{1}{r^2} \cdot e^{\frac{-\theta^2}{2\sigma^2}} dl \qquad (2)$$

Q is the dust production rate and v is the dust velocity at the source points on the surface. ρ is the integral term of the brightness column density, N, calculated for a Gaussian jet by $N = \frac{Q}{4\pi v} \cdot \rho$. The angle between the vector (source-signal) and the symmetry axis of the Gaussian is θ and σ is the FWHM. By solving the linear system we get a n-vector $\frac{Q}{4\pi v}$ which gives us information about the ratio of the production rate to the outflow velocity. The right-hand side quantities of the linear system are the signals of the MICAS images along one envelope around the nucleus. The point of this approach is to try to place constraints on hydrodynamic models by direct analysis of the data in a simple and rapid way.

Modeling Results

With the solution of the linear system we get the position and Q/v values of the dust emission on the nucleus. These inputs can then be used to simulate an image of the inner coma. Figure 5 below shows the dust emission model with Gaussian jets of 10° FWHM. This model reproduces the main emission features

Fig. 5. This figure shows the simulation of the inner coma by Gauss - shaped jets. The FWHM is 10°. The sources are lying 1 km below the surface border.

Fig. 6. This plot shows the brightness distribution of Borrelly (——) and the model (- - -) at 10 km above the nucleus surface.

fairly well. The dust fans at the lower and upper tip of the nucleus could not be reproduced with an half

opening angle of 10° and a source distance of 10° (angle step around the assumed nucleus center). The sources are too far from each other or the opening angle is too narrow. The linear system constrains the model to fit perfectly at 3 km (the altitude of the input signal). The brightness of Borrelly's coma is higher close to the nucleus. At greater distances from the nucleus (> 8 km) the brightness distribution of the real comet is lower (see Figure 6). This can be also seen in Figure 4. The model's $\oint Ids$ is almost constant which suggests that the deviation from a point source is not an adequate explanation for the observed behaviour at Borrelly. Acceleration and/or fragmentation into small particles will be the subject of future investigation. We are not able to reproduce exactly the brightness distribution around the nucleus with the assumptions set up for the linear system. But we have examined the influence of inclined and non radial jets on $\oint Ids$. The increase of the intensity of the model towards the nucleus comparing with Borrelly's is very small.

SUMMARY AND CONCLUSION

Comet Borrelly's inner dust coma, as observed by the Deep Space 1 spacecraft on 22 Sept. 2001, was dominated by a main collimated dust emission on the dayside (FWHM = 18°) and a broader emission feature on the nightside (FWHM = 74°) of the nucleus. The dayside to nightside brightness ratio was $\approx$ 3.3 :1.0. This is remarkably similar to that of Halley at a similar phase angle as observed from Giotto. The integrated brightness of Borrelly's coma was a factor of 48 below that of Halley at Giotto encounter. Taking into account the outflow velocity, we estimate a dust production rate ratio between the two comets of 80:1 and a dust to gas ratio for Borrelly five times less than that of Halley at Giotto encounter. The integrated intensities around concentric envelopes show significant differences close to the nucleus for Halley and Borrelly. In the case of Halley, a flattening of the intensity was observed which could result from high optical thickness effects or particle fragmentation into optically large sizes. On the other hand, Borrelly's coma shows a steepening of the intensity. This slope could be explained by particle acceleration, particle fragmentation to submicron sizes or deviations from a point source. We have analysed these possibilities with a model which assumes force free radial outflow and dust emission coming from distributed sources. Deviations from point source geometry do not appear to have sufficient influence on the intensity distribution to explain the observed behaviour at Borrelly. Either fragmentation or acceleration effects seem to be more important.

REFERENCES

A'Hearn, M.F., R.L. Millis, D.G. Schleicher et al., The ensemble properties of comets: Results from narrowband photometry of 85 comets, 1976-1992, *Icarus*, **118**, 223-270, 1995.

Boice, D.C., D.T. Britt, R.M. Nelson et al., The near-nucleus environment of 19P/Borrelly during the Deep Space One encounter, *Lunar and Planetary Science XXXIII*, 2002.

Crifo, J.F. and A.V. Rodionov, Modeling the circumnuclear coma of comets: objectives, methods and recent results, *Planetary and Space Science*, **47**, 797-826, 1999.

Festou, M.C., P.D. Feldman, M.F. A'Hearn et al., IUE observations of comet Halley during the VEGA and Giotto encounters, *Nature*, **321**, 361-368, 1986.

Fulle, M., A.C. Levasseur-Regourd, N. McBride et al., In situ dust measurements from within the coma of 1P/Halley: First-order approximation with a dust dynamical model, *Astron. J.*, **119**, 1968-1977, 2000.

Gombosi, T. I., A.F. Nagy and T.E. Cravens, Dust and neutral gas modeling of the inner atmospheres of comets, *Reviews of Geophysics*, **24**, 667-700, 1986.

Keller, H. U. and N. Thomas, Evidence for near surface breezes on comet P/Halley, *Astron. Astrophys.*, **226**, L9-L12, 1989.

Keller, H. U., W. Curdt, J.-R. Kramm et al., Images of the nucleus of comet Halley, *ESA SP-1127*, **Vol. 1**, 1994.

Kitamura, Y., Axisymmetric Dusty Gas Jets in the Inner Coma of a Comet I, *Icarus*, **66**, 241-257, 1986.

Kitamura, Y., Axisymmetric Dusty Gas Jets in the Inner Coma of a Comet II, *Icarus*, **72**, 555-567, 1987.

Knollenberg, J., Modellrechnungen zur Staubverteilung in der inneren Koma von Kometen unter spezieller Beruecksichtigung der HMC-Daten der GIOTTO-Mission, *Ph.D. thesis*, Georg-August-Universitaet, Goettingen, Germany, 1994. (In German)

McDonnell, J.A.M., G.S. Pankiewicz, P.N.W. Birchley et al., The comet nucleus - Ice and dust morphological

balances in a production surface of Comet P/Halley, *Lunar and Planetary Science Conference, Proceedings (A90-33456 14-91)*, 373-378, 1990.

Reitsema, H. J., W.A. Delamere, A.R. Williams et al., Dust distribution in the inner coma of Comet Halley - Comparison with models, *Icarus*, **81**, 31-40, 1989.

Soderblom L.A., T.L. Becker, G. Bennet et al., Observations of Comet 19P/Borrelly by the Miniature Integrated Camera and Spectrometer aboard Deep Space 1, *Science*, **296**, 1087-1091, 2002.

Stern, S.A., H.A. Weaver and J.Wm. Parker, HST/STIS Observations of Comet 19P/Borrelly during the DS1 encounter, submitted to *Science*, 2002.

Thomas, N., D.C. Boice, W.F. Huebner et al., Intensity profiles of dust near extended sources on comet Halley, *Nature*, **332**, 51-52, 1988.

Thomas, N. and H.U. Keller, Interpretation of the inner coma observations of comet P/Halley by the Halley Multicolour Camera, *Annales Geophysicae*, **8**, 147-166, 1990.

Appendix B

Data sets

On the following pages, the images of the MICAS and Pik Terskol data sets are listed including the important identifications, like phase angle, exposure time etc. Not all data could be used in the analysis because of bad calibration or bad observational conditions, which is in the case of the ground-based data.

B.1   DS1-MICAS

Image name	Time Relative to C/S [s]	Phase angle [°]	Exposure [ms]	Range [km]	Resolution (m/pixel)
CCD_Far_1_4	-4996	87.6	874	82882.2	1089.1
CCD_Far_1_5	-4966	87.6	1750	82384.9	1082.5
MID_1_1	-578	76.4	614	9825.9	129.1
MID_1_2	-548	75.7	109	9341.3	122.7
MID_2_1	-518	75.0	218	8858.2	116.4
MID_2_2	-483	74.0	109	8296.6	109.0
MID_3_1	-437	72.5	218	7562.7	99.4
MID_3_2	-407	71.3	614	7087.8	93.1
MID_4_1	-377	70.0	109	6616.0	86.1
MID_4_2	-347	68.5	218	6148.2	80.8
MID_5_1	-290	64.9	109	5274.3	69.3
MID_5_2	-260	62.5	218	4825.3	63.4
MID_5_3	-230	59.6	77	4386.7	57.6
MID_5_4	-200	56.0	154	3962.0	52.1
NEAR_1	-170	51.6	77	3556.3	46.7

Table B.1: The encounter images taken by the VISCCD of MICAS applied for the data analysis. Additional to that the characteristics of each single image is also included. C/S denotes the encounter time of closest approach. Phase angle is the angle between Sun-Target-Observer. Range is the distance of the spacecraft to the nucleus.

B.2 Pik Terskol

Filename	Filter	Time [UT]	Exposure Time [s]	Phase angle [°]	Δ [AU]	r [AU]
20/09/01						
Bor64201	IF642	00:08:02	300	41.0481	1.485448	1.359590
Bor52601	IF526	00:20:08	300	41.0487	1.485411	1.359594
Bor44401	IF444	00:29:08	300	41.0490	1.485383	1.359598
Bor63101	IF631	00:36:55	300	41.0494	1.485358	1.359601
Bor44402	IF444	01:30:58	600	41.0519	1.485189	1.359621
Bor52602	IF526	01:45:06	600	41.0525	1.485146	1.359626
Bor64202	IF642	01:57:34	600	41.0531	1.485105	1.359631
21/09/01						
Borrx01	RX	00:12:06	100	41.1154	1.481128	1.360168
Bor64201	IF642	00:18:33	600	41.1158	1.481106	1.360171
Bor52601	IF526	00:33:02	600	41.1164	1.481063	1.360177
Bor44401	IF444	00:49:03	600	41.1171	1.481013	1.360184
Bor44402	IF444	00:59:55	600	41.1175	1.480980	1.360189
22/09/01						
Borrx01	RX	00:15:05	100	41.1797	1.476867	1.360845
Borrx02	RX	00:19:34	100	41.1799	1.476852	1.360848
Borrx03	RX	00:22:41	100	41.1800	1.476843	1.360849
Bor64201	IF642	00:26:08	600	41.1802	1.476833	1.360851
Bor66201	IF662	00:37:57	1200	41.1807	1.476797	1.360857
Bor52601	IF526	01:51:55	1200	41.1836	1.476572	1.360894
Borrx04	RX	02:14:11	50	41.1845	1.476503	1.360906

Table B.2: This Table contains the continuum images at Pik Terskol taken on the night September 19/20, 20/21 and 21/22 2001. The time is presented as Universal Time [UT], Δ represents the geocentric distance of the comet and r its heliocentric distance, both in Astronomical Units. The Phase angle is the angle between the Sun, the target and the observer.

Appendix C

Refractive Indices

The complex refractive indices of all components considered to be dust grain material are listed in the following tables for the MICAS (500 - 1000 nm) and the Pik Terskol (443.5 nm, 525.5 nm, 630.8 nm, 641.6 nm) data sets. The values has been obtained by interpolating given values in the papers of Draine (1985), Weingartner and Draine (2001), Jenniskens (1993), Rouleau and Martin (1991). Also given are the densities of the materials.

Further are listed the combined complex refractive indices for particles which are made of a mixture of two components. This indices has been derived by the Maxwell-Garnett function.

C.1   Refractive Indices for the Analysis of the VISCCD Data set - 1 component

Material	$\lambda[\mu m]$	n	k
Astronomical silicates [1]	500	1.722354	0.029321
$\rho = 3500$ kgm^{-1}	600	1.716439	0.029422
	700	1.714901	0.029739
	800	1.714901	0.029739
	900	1.714910	0.030031
	1000	1.714911	0.030322
Astronomical silicates	500	1.673223	0.030116
smoothed UV [2]	600	1.669410	0.030309
$\rho = 3500$ gm^{-1}	700	1.667298	0.030529
	800	1.666405	0.030770
	900	1.666190	0.030961
	1000	1.666000	0.031140
Organic refractories,	500	1.855	0.4500
heavily UV processed [3]	600	1.908	0.3893
$\rho = 1600$ kgm^{-1}	700	1.971	0.3170
	800	2.000	0.2425
	900	1.995	0.2593
	1000	2.005	0.229
Amorphous carbon [4]	500	2.19894	0.226425
$\rho = 1850$ kgm^{-1}	600	2.18045	0.223074
	700	2.15920	0.226526
	800	2.13984	0.231300
	900	2.12022	0.234744
	1000	2.10483	0.234003

Table C.1: The interpolated complex refractive indices at wavelengths specific for the Micas data sets for silicate, organic refractory and amorphous carbon. ρ denotes the material density. [1] taken by Draine, 1985. [2] taken by Weingartner and Draine, 2001. [3] taken by Jenniskens, 1993. [4] taken by Rouleau and Martin, 1991.

C.2 Refractive Indices for the Analysis of the VISCCD Data set - 2 component

Material	λ [nm]	n	k	density [kg m^{-1}]
Astronomical silicates [1]	500	1.81417	0.314713	2196
+ organic refractory	600	1.84777	0.273796	2196
1:1	700	1.88034	0.241257	2196
	800	1.89931	0.208761	2196
	900	1.90611	0.186023	2196
	1000	1.91292	0.165524	2196
Astronomical silicates [1]	500	1.83100	0.369444	2507
+ organic refractory	600	1.87236	0.320495	2507
2:1	700	1.91153	0.281563	2507
	800	1.93412	0.242796	2507
	900	1.94220	0.215642	2507
	1000	1.95028	0.191169	2507
Astronomical silicates [1]	500	2.03187	0.157455	2421
+ amorphous carbon	600	2.01780	0.155282	2421
1:1	700	2.00346	0.157579	2421
	800	1.99088	0.160625	2421
	900	1.97816	0.162911	2421
	1000	1.96819	0.162498	2421
Astronomical silicates [1]	500	2.09755	0.184460	2698
+ amorphous carbon	600	2.08175	0.181828	2698
2:1	700	2.06470	0.184582	2698
	800	2.04947	0.188308	2698
	900	2.03405	0.191053	2698
	1000	2.02196	0.190516	2698

Table C.2: The complex refractive indices for a mixture of astronomical silicate Typ1 and organic refractory or amorphous carbon at MICAS wavelengths. These values are derived with the Maxwell-Garnett function.

C.3   Refractive Indices for the Analysis of Pik Terskol Data - 1 component

Material	[nm]	n	k
Astronomical silicates [1]	443.5	1.72630	0.0292537
$\rho = 3500$ kgm^{-1}	525.5	1.72004	0.0293600
	630.8	1.71559	0.0294360
	641.6	1.71530	0.0294411
Astronomical silicates,	443.5	1.67773	0.0299899
smoothed UV [2]	525.5	1.67187	0.0301634
$\rho = 3500$ kgm^{-1}	630.8	1.66840	0.0303697
	641.6	1.66818	0.0303908
Organic refractory,	443.5	1.80325	0.484330
heavily UV processed [3]	525.5	1.87030	0.430620
$\rho = 1600$ kgm^{-1}	630.8	1.92102	0.376292
	641.6	1.92663	0.370784
Amorphous carbon [4]	443.5	2.22056	0.228245
$\rho = 1850$ kgm^{-1}	525.5	2.19187	0.223114
	630.8	2.17328	0.225035
	641.6	2.17056	0.225670

Table C.3: These are the interpolated complex refractive indices at wavelengths specific for the Pik Terskol data sets for silicate, organic refractory and amorphous carbon. ρ denotes the material density.. [1] taken by Draine, 1985. [2] taken by Weingartner and Draine, 2001. [3] taken by Jenniskens, 1993. [4] taken by Rouleau and Martin, 1991.

C.4   Refractive Indices for the Analysis of Pik Terskol Data - 2 component

Material	λ [nm]	n	k	density [kg m^{-1}]
astronomical silicates [1] + organic refractory 1:1	443.5	1.7851190	0.34214676	2196
	525.5	1.8281049	0.30282800	2196
	630.8	1.8599233	0.26410233	2196
	641.6	1.8635032	0.26029579	2196
astronomical silicates [1] + organic refractory 2:1	443.5	1.7732548	0.26737673	2507
	525.5	1.8040071	0.23665400	2507
	630.8	1.8265544	0.20674788	2507
	641.6	1.8291434	0.20373747	2507
Astronomical silicates [1] + amorphous carbon 1:1	443.5	2.0431870	0.15193397	2421
	525.5	2.0229449	0.14921772	2421
	630.8	2.0097565	0.15068905	2421
	641.6	2.0079709	0.15113077	2421
astronomical silicates [1] + amorphous carbon 2:1	443.5	1.9596782	0.11819007	2698
	525.5	1.9432415	0.11636531	2698
	630.8	1.9324525	0.11752556	2698
	641.6	1.9310793	0.11786081	2698

Table C.4: This are the complex refractive indices of silicate and organic refractory mixtures or silicate and amorphous carbon mixture at wavelengths of the Pik Terskol filters for different ratios of the components. This effective refractive indices are calculated with the Maxwell-Garnett function.

Bibliography

[1] **A'Hearn, M.F., D.G. Schleicher, R.L. Millis, P.D. Feldma, and D.T. Thompson.** *Comet Bowell 1980b.* Astron. J., 89, 579-591, **1984**.

[2] **A'Hearn, M.F., R.L. Millis, D.G. Schleicher, D.J. Osip, and P.V. Birch.** *The Ensemble Properties of Comets: Results from Narrowband Photometry of 85 Comets, 1976-1992.* Icarus, 118, 223-270, **1995**.

[3] **A'Hearn, M.F., S. Hoban, P.V. Birch, C. Bowers, R. Martin, and D. Klinglesmith III.** *Cyanogen jets in comet Halley.* Nature, 324, 649-651, **1986**.

[4] **Aitken, R.G..** *Observations of Comet a 1904 (Brooks); Observations of Comet D 1904 (Giacobini) ; Observations of Comet E 1904 (Borrelly); Observations of Comet a 1905 (Giacobini); Observations of Comet B 1905 (Schaer).* Lick Observatory bulletin, 89, 189-191, **1905**.

[5] **Biermann, L..** *Kometenschweife und solare Korpuskularstrahlung.* Zeitschrift für Astrophysik, 274, **1951**.

[6] **Bockelée-Morvan, D., N. Biver, P. Colom, J. Crovisier, F. Henry, A. Lecacheaux, J.K. Davies, W.R.F. Dent, and H.A. Weaver.** *Radio Investigations Of 19p/Borrelly In Support To The Deep Space 1 Flyby.* Icarus, 167, 113-128, **2004**.

[7] **Boice, D.C., D.T. Britt,R.M. Nelson, B.R. Sandel, L.A. Soderblom, N. Thomas, and R.V. Yelle.** *The near-nucleus environment of 19P/Borrelly during the Deep Space One Encounter.* Lunar and Planetary Science XXXIII, **2002**.

[8] **Bohren, C.F. and D.R. Huffman.** *Absorption and scattering of light by small particles.* New York: Wiley, **1983**.

[9] **Bonev, T., K. Jockers, E. Petrova, M. Delva, G. Borisov, and A. Ivanova.** *The Dust in Comet C/1999 S4 (LINEAR) during Its Disintegration: Narrow-Band Images, Color Maps, and Dynamical Models.* Icarus, 160, 419-436, **2002**.

[10] **Burns, J.A., P.L. Lamy, and S. Soter**. *Radiation forces on small particles in the solar system.* Icarus, 40, 1-48, **1979**.

[11] **Cochran, A.L. and E.S. Barker.** *McDonald Observatory Spectral Observations of Comet 19P/Borrelly.* Icarus, 141, 307-315, **1999**.

[12] **Combi, M. and V. Tenishev**. Personal communication. **2003**.

[13] **Courtès G.**. *Methodes d'observations et etude de l'hydrogene interstellaire en emission.* Ann. d'Astrophys., 23 N 2, 115-217, **1960**.

[14] **Cremonese, G., H. Boehnhardt, J. Crovisier, H. Rauer, A. Fitzsimmons, M. Fulle, J. Licandro, D. Pollacco, G.P. Tozzi, and R.M. West.** *Neutral Sodium from Comet Hale-Bopp: A Third Type of Tail.* Astrophysical Journal Letters, L199, **1997**.

[15] **Crifo, J.F., A.L. Itkin, and A.V. Rodionov**. *The Near-Nucleus Coma Formed by Interacting Dusty Gas Jets Effusing from a Cometary Nucleus: I.* Icarus, 116, 77-112, **1995**.

[16] **Crifo, J.F. and A.V. Rodionov**. *The Dependence of the Circumnuclear Coma Structure on the Properties of the Nucleus.* Icarus, 129, 72-93, **1997**.

[17] **Crifo, J.F. and A.V. Rodionov.** *Modeling the circumstannuclear coma of comets: objectives, methods and recent results.* Planetary and Space Science, 47, 797-826, **1999**.

[18] **Davidsson, B.J.R. and Y.V. Skorov.** *On the Light-Absorbing Surface Layer of Cometary Nuclei. I. Radiative Transfer.* Icarus, 156, 223-248, **2002**.

[19] **Davidsson, B.J.R. and P.J. Gutiérrez.** *Estimating the nucleus density of Comet 19P/Borrelly.* Icarus, 168, 392-408, **2004**.

[20] **Divine N. and Newburn**. *Numerical Models of Cometary Dust Environments.* Cometary exploration; Proceedings of the International Conference, Budapest, Hungary, November 15-19, Ajademiai Kiado, 2, A84-47701 23-90, **1983**.

[21] **Divine, N., H. Fechtig, T.I. Gombosi, M.S. Hanner, H.U. Keller, S.M. Larson, D.A. Mendis, R.L. Newburn, R. Reinhard, Z. Sekanina, and D.K. Yeomans.** *The Comet Halley dust and gas environment.* Space Science Reviews, 43, 1-104, **1986**.

[22] **Draine, B.T. and H.M. Lee.** *Optical properties of interstellar graphite and silicate grains.* Astrophys. J., 284, 89-108, **1984**.

[23] **Draine, B.T..** *Tabulated optical properties of graphite and silicate.* Astrophys. J. SS, 57, 587-594, **1985**.

[24] **Edgeworth, K.E..** *The evolution of our Planetary System.* J. of the British Astron. Assoc., 53, 181-188, **1943**.

[25] **Edgeworth, K.E..** *The origin and evolution of the solar system.* Mon. Not. R. Astr. Soc., 109, 600-609, **1949**.

[26] **Festou, M.C., Feldman, P.D., M.F. A'Hearn, C. Arpigny, C.B. Cosmovici, A.C. Danks, L.A. McFadden, R. Gilmozzi, P. Patriarchi, G.P. Tozzi, M.K. Wallis, and H.A. Weaver.** *IUE observations of comet Halley during the VEGA and Giotto encounters.* Nature, 321, 361-368, **1986**.

[27] **Festou, M.C., H. Rickman, and R.M. West**. *Comets I. Concepts and Observations.* The Astron. Astrophys. Rev., 4, 363-447, **1993**.

[28] **Finson M.L. and R.F. Probstein**. *A Theory of Dust Comets. I. Model and Equations.* Astrophys. Journal, 154, 327-352, **1968**.

[29] **Finson M.L. and R.F. Probstein**. *A Theory of Dust Comets. II. Results for Comet Arend-Roland.* Astrophys. J., 154, 353-379, **1968**.

[30] **Fulle, M**. *Evaluation of cometary dust parameters from numerical simulations: comparison with an analytical approach and the role of anisotropic emissions.* Astron. Astrophys., 217, 283-297, **1989**.

[31] **Fulle, M., A. Milani, and L. Pansecchi.** *Tomography of a sunward structure in the dust tail of comet 19P/Borrelly.* Astron. Astrophys., 321, 338-342, **1997**.

[32] **Fulle, M., A.C. Levasseur-Regourd, N. McBride, and E. Hadamcik.** *In Situ Dust Measurements From within the Coma of 1P/Halley: First-Order Approximation with a Dust Dynamical Model.* Astron. J., 119, 1968-1977, **2000**.

[33] **Gombosi, T.I..** In: 20th ESLAB Symposium on the Exploration of Halley's comet. Ed. B. Basttrick, E.J. Rolfe, and R. Reinhard. ESA-SP-250, 167-171, **1986**.

[34] **Gombosi, T.I., K. Szego, B.E. Gribov, R.Z. Sagdeev, V.D. Shapiro, V.I. Shevchenko, and T.E. Cravens.** *Gas dynamic calculations of dust terminal velocities with realistic dust size distributions.* In: Cometary exploration; Proceedings of the International Conference, Budapest, Akademiai Kiado, 2, 99-111, **1983**.

[35] **Gombosi, T.I., T.E. Cravens, and A.F. Nagy**. *Time-dependent dusty gasdynamical flow near cometary nuclei.* Astrophys. J., 293, 328-341, **1985**.

[36] **Gombosi, T.I., A.F. Nagy, and T.E. Cravens.** *Dust and neutral gas modeling of the inner atmospheres of comets.* Reviews of Geophysics, 24, 667-700, **1986**.

[37] **Greenberg, J.M. and J.I. Hage.** *From interstellar dust to comets. A unifications of observational constraints.* Astrophys. J., 361, 260-274, **1990**.

[38] **Greenberg, J.M. and A. Li.** *All comets are born equal: infrared emission by dust as a key to comet nucleus composition.* Planetary and Space Science, 47, 787-795, **1999**.

[39] **Groussin, O..** *Les noyaux cométaires et leurs processus d'activité.* Ph.D. Thesis. Université de la Méditerranée Aix-Marseille II. **2002**. (In French)

[40] **Grün, E. and E.K. Jessberger.** *Dust.* In *Physics and chemistry of comets.* W.F. Huebner (Ed.), Springer, **1990**.

[41] **Hamuy, M., A.R. Walker, N.B. Suntzeff, P. Gigoux, S.R. Heathcote, and M.M. Phillips.** *Southern Spectrophotometric Standards. I.* Astronomical Society of the Pacific, 104, 533-552, **1992**.

[42] **Hamuy, M., A.R. Walker, N.B. Suntzeff, P. Gigoux, S.R. Heathcote, and M.M. Phillips.** *Southern Spectrophotometric Standards. II.* Astronomical Society of the Pacific, 104, 533-552, **1994**.

[43] **Hanner, M.S., R.H. Giese, K. Weiss, and R. Zerull.** *On the Definition of Albedo and Application to Irregular Particles.* Astron. Astrophys., 104, 42-46, **1981**.

[44] **Hanner, M.S..** In: Cometary Exploration. Central. Res. Inst. Physics, Hungarian Acad. Sci., Budapest, T.I. Gombosi (ed.), 2, 1, **1983**.

[45] **Hanner M.S., E. Tedesco, A.T. Tokunaga, G.J. Veeder, D.F. Lester, F.C. Witteborn, J.D. Bregman, J. Gradie, and L. Lebofsky.** *The Dust Coma of Periodic Comet Churyumov-Gerasimenko (1982 VIII).* Icarus, 64, 11-19, **1985**.

[46] **Hanner, M.S., A.T. Tokunaga, W.F. Golisch, D.M. Griep, and C.D. Kaminski.** *Infrared emission from P/Halley's dust coma during March 1986.* Astron. Astrophys., 187, 653-660, **1987**.

[47] **Hanner, M.S..** *Mid-Infrared Spectra of Comets P/Borrelly, P/Faye, and P/Schaumasse.* Icarus, 124, 344-351, **1996**.

[48] **Hansen, J.E. and L.D. Travis.** *Light scattering in planetary atmospheres.* Space Sci. Rev., 16, 527-610, **1974**.

[49] **Hellmich,R..** *The Influence of the Radiation Transfer in Cometary Dust Halos on the Production Rates of Gas and Dust.* Astron. Astrophys., 93, 341, **1981**.

[50] **Hellmich, R. und H.U. Keller.** *On the dust production rates of comets.* In: Solid particles in the solar system, Proceedings of the Symposium, Ottawa. Dordrecht, D. Reidel Publishing Co., 255-258, **1980**.

[51] **Hellmich, R. and G. Schwehm**. *Predictions of dust particle number flux and fluence rates for the ESA-Giotto and USSR Vega-missions to Comet Halley - A comparison.* IN: Cometary exploration; Proceedings of the International Conference. Budapest, Akademiai Kiado, 175-183, **1983**.

[52] **Hodkinson, J.R. and I. Greanleaves.** *Computations of light scattering and extinction by spheres according to diffraction and geometrical optics, and some comparisons with Mie theory.* J. Opt. Soc. Amer., 53, 577-588, **1963**.

[53] **Horanyi, M., T.I. Gombosi, T.E. Cravens, A. Korosmezey, K. Kecskemety, A.F. Nagy, and K. Szego.** *The friable sponge model of a cometary nucleus.* Astrophys. J., 278, 449-455, **1984**.

[54] **Huebner, W. F..** *Dust from cometary nuclei.* Astron. Astrophys., 5, 286-297, **1970**.

[55] **Huebner, W.F. and A. Weigert**. *Eiskörner in der Koma von Kometen.* Z. Astrophys., 64, 185-201, **1966**.

[56] **Hulst van de, H.C..** *Light scattering by small particles.* New York, Dover Publications, **1981**.

[57] **Jackson, J.D..** *Classical Electrodynamics*, Wiley, **1998**.

[58] **Jeffers, H.M., S. Vasilevskis, and E. Roemer.** *Observations of comets and asteroids.* Astron. J., 59, 305, **1954**.

[59] **Jenniskens, P..** *Optical constants of organic refractory residue.* Astron. Astrophys., 274, 653-661, **1993**.

[60] **Jenniskens, P., G.A. Baratta, A. Kouchi, M.S. de Groot, J.M. Greenberg, and G. Strazzulla.** *Carbon dust formation on interstellar grains.* Astron. Astrophys., 273, 583, **1993**.

[61] **Jessberger, E.K., A. Christoforidis, and J. Kissel.** *Aspects of the major element composition of Halley's dust.* Nature, 332, 691-695, **1988**.

[62] **Jewitt, D.C. and G.E. Danielson.** *Charge-coupled device photometry of Comet P/Halley.* Icarus, 60, 435-444, **1984**.

[63] **Jewitt, D.C. and K.J. Meech.** *Cometary Grain Scattering Versus Wavelength, or "What color is comet dust?"* Astrophys. J., 310, 937-952, **1986**.

[64] **Jewitt, D.C. and K.J. Meech.** *Surface brightness profiles of 10 comets.* Astrophys. J., 317, 992-1001, **1987**.

[65] **Jewitt, D.C. and J.X. Luu.** *Discovery of the Candidate Kuiper Belt Object 1992QB$_1$.* Nature, 362, 730-732, **1992**.

[66] **Jockers, K.** *Observations Of Scattered Light From Cometary Dust and Their Interpretation.* Earth, Moon and Planets, 79, 221-245, **1997**.

[67] **Jockers, K. and T. Bonev.** *H$_2$O$^+$, CO$^+$ and dust in Comet P/Swift-Tuttle.* Astron. Astrophys., 319, 617-629, **1997**.

[68] **Jockers, K., T. Credner, T. Bonev, V.N. Kiselev, P. Korsun, I. Kulyk, V. Rosenbush, A. Andrienko, N. Karpov, A. Sergeev, and V. Tarady.** *Exploration of the Solar System with the Two-Channel Focal Reducer at the 2m-RCC Telescope of Pik Terskol Observatory.* Astron. Astrophys. Rev., 4, 363-447, **2000**.

[69] **Keller H.U..** *Gas and dust models of the coma.* In Cometary Exploration, Ed. T.I. Combosi. Central Research Insitute for Physics, Hungarian Academy of Sciences, Budapest, 119-137, **1983**.

[70] **Keller, H.U., C. Arpigny, C. Barbieri, R.M. Bonnet, S. Cazes, M. Coradini, C.B. Cosmovici, W.A. Delamere, W.F. Huebner, D.W. Hughes, C. Jamar, D. Malaise, H.J. Reitsema, H.U. Schmidt, W.K.H. Schmidt, P. Seige, F.L. Whipple, and K. Wilhelm.** *First Halley multicolour camera imaging results from Giotto.* Nature, 321, 320-326, **1986**.

[71] **Keller, H. U., W.A. Delamere, W.F. Huebner, H.J. Reitsema, H.U. Schmidt, F.L. Whipple, K. Wilhelm, W. Curdt, R. Kramm, N. Thomas, C. Arpigny, C. Barbieri, R.M. Bonnet, S. Cazes, M. Coradini, C.B. Cosmovici, , C.B. Cosmovici, C. Jamar, D. Malaise, K. Schmidt, W.K.H. Schmidt, and P. Seige.** *Comet P/Halley's nucleus and its activity.* Astron. Astrophys., 187, 807-823, **1987**.

[72] **Keller, H.U., R. Kramm, and N. Thomas.** *Surface features on the nucleus of Comet Halley.* Nature, 331, 227-231, **1989**.

[73] **Keller H.U. and N. Thomas.** *Evidence for near surface breezes on comet P/Halley.* Astron. Astrophys., 226, L9-L12, **1989**.

[74] **Keller, H.U., W. Curdt, J.-R. Kramm, and N. Thomas.** *Images of the nucleus of comet Halley.* ESA SP-1127, Vol.1, **1994**.

[75] **Kissel, J., R.Z. Sagdeev, J.L. Bertaux, V.N. Angarov, J. Au-douze, J.E. Blamont, K. Buchler, E.N. Evlanov, H. Fechtig, M.N. Fomenkova, H. von Hoerner, N.A. Inogamov, V.N. Khromov, W. Knabe, F.R. Krueger, Y. Langevin, B. Leonasv, A.C. Levasseur-Regourd, G.G. Managadze, S.N. Podkolzin, V.D. Shapiro, S.R. Tabaldyev, and B.V. Zubkov.** *Composition of comet Halley dust particles from VEGA observations.* Nature, 321, 280-282, **1986a**.

[76] **Kissel, J., D.E. Brownlee, K. Buchler, B.C. Clark, H. Fechtig, E. Grün, K. Hornung, E. Igenbergs, E.K. Jessberger, F.R. Krueger, H. Kuczera, J.A.M. McDonnell, G.M. Morfill, J. Rahe, G.H. Schwehm, Z. Sekanina, N.G. Utterback, H.J. Volk, and H.A. Zook.** *Composition of comet Halley dust particles from Giotto observations.* Nature, 321, 336-337, **1986b**.

[77] **Kitamura, Y.**. *Axisymmetric dusty gas jet in the inner coma of a comet.* Icarus, 66, 241-257, **1986**.

[78] **Kitamura, Y.**. *Axisymmetric dusty gas jet in the inner coma of a comet. II - The case of isolated jets.* Icarus, 72, 555-567, **1987**

[79] **Kitamura, Y.**. *A numerical study of the interaction between two cometary jets - A possibility of shock formation in cometary atmospheres.* Icarus, 66, 241-257, **1990**.

[80] **Knollenberg, J.**. *Modellrechnung zur Staubverteilung in der inneren Koma von Kometen unter spezieller Bercksichtigung der HMC-Daten der GIOTTO-Mission.* Ph.D. Thesis, Georg-August-Universtit"at, G"ottingen, Germany, **1994**. (In German)

[81] **Kuiper, G.P.**. *On the origin of the Solar System.* In: Astrophysics, A Topical Symposium, Ed. J.A. Hynek, McGraw-Hill, New-York, 357-424, **1951**.

[82] **Lamy, P. L., E. Gruen, and J.M. Perrin.** *Comet P/Halley - Implications of the mass distribution function for the photopolarimetric properties of the dust coma.* Astron. Astrophys., 187, 767-773, **1987**.

[83] **Lamy, P.L., I. Toth, and H.A. Weaver**. *Hubble Space Telescope observations of the nucleus and inner coma of comet 19P/1904 Y2 (Borrelly).* Astron. Astrophys., 337, 945-954, **1998**.

[84] **Landau, L.D. and E.M. Lifshitz.** *Electrodynamic of Continous Media.* New York, Pergamon. **1960.**

[85] **Langevin, Y., J. Kissel, J.-L. Bertaux, and E. Chassefiere.** *First statistical analysis of 5000 mass spectra of cometary grains obtained by*

PUMA 1 (Vega 1) and PIA (Giotto) impact ionization mass spectrometers in the compressed modes. Astron. Astrophys., 187, 761-766, **1987**.

[86] **Li, A. and J.M. Greenberg.** *A unified model of interstellar dust.* Astron. Astrophys., 323, 566-584, **1997**.

[87] **Li, A. and J.M. Greenberg.** *The dust properties of a short period comet: comet P/Borrelly.* Astron. Astrophys., 338, 364-370, **1998**.

[88] **Maas, R.W., E.P. Ney and N.F. Woolf.** *The 10-MICRON Emission Peak of Comet ennett 1969i.* Astrophys. J., 160, L101, **1970**.

[89] **Macke, A..** *Scattering of light by polyhedral ice crystals.* Applied Optics, 32, 2780-2788, **1993**.

[90] **Marconi, M.L. and D.A. Mendis.** *The effects of the diffuse radiation fields due to multiple scattering and thermal reradiation by dust on the dynamics and thermodynamics of a dusty cometary atmosphere.* Astrophys. J., 287, 445-454, **1984**.

[91] **Marconi, M.L. and D.A. Mendis.** *Infrared heating of Comet Halleys atmosphere.* Earth, Moon, and Planets, 36, 249-256, **1986**.

[92] **McDonnell, J. A. M., G.S. Pankiewicz, P.N.W. Birchley, S.F. Green, and C.H. Perry.** *The comet nucleus - Ice and dust morphological balances in a production surface of Comet P/Halley.* Lunar and Planetary Science Conference, Proceedings, 373-378, **1990**.

[93] **McDonnell, J.A.M., P.L. Lamy and G.S. Pankiewicz.** *Physical properties of cometary dust.* Comets in Post-Halley Era. Eds. R.L. Newburn, Jr. *et al.*, Kluwer Academic Publisher, 2, 1043-1073, **1991**.

[94] **Mendis, D.A..** *Hydrodynamic models of the cometary atmosphere.* In: Highlights of astronomy, Volume 6., International Astronomical Union, Proceedings , Dordrecht, 709-712, **1983**.

[95] **Müller, M..** *A Model of the Inner Coma of Comets with Applications to the Comets P/Wirtanen and P/Wild 2.* PhD Thesis. Ruprecht-Karls Universität Heidelberg, Germany. **1999.**

[96] **Newburn, R.L. and H. Spinrad.** *Spectrophotometry of 25 Comets: Post-Halley updates for 17 comets plus new observations for eight additional comets.* Astron. J., 97, 552-569, **1989**.

[97] **Ney, E.P..** *Optical and infrared observations of bright comets in the range 0.5 micrometers to 20 micrometers.* In: Comets, Tucson, AZ, University of Arizona Press, 323-340, **1982**.

[98] **Reitsema, H. J., W.A. Delamere, A.R. Williams, D.C. Boice, W.F. Huebner, and F.L. Whipple.** *Dust distribution in the inner coma of Comet Halley - Comparison with models.* Icarus, 81, 31-40, **1989**.

[99] **Oberst, J., S. Mottola, M. di Martino, M. Hicks, B. Buratti, L. Soderblom, and N. Thomas**. *A Model for Rotation and Shape of Asteroid 9969 Braille from Ground-Based Observations and Images Obtained during the Deep Space 1 (DS1) Flyby.* Icarus, 153, 16-23, **2001**.

[100] **Oort, J.H..** *The structure of the cloud of comets surrounding the Solar System and a hypothesis concerning its origin.* Bull. Astron. Inst. Neth., 91-110, **1950**.

[101] **Pollack, J.B. and J.N. Cuzzi**.*Scattering by Nonspherical Particles of Size Comparable to a Wavelength: A New Semi-Empirical Theory and Its Applicaiont to Tropospheric Aerosols.* Journal of the Atmospheric Sciences, 37, 868-881, **1979**.

[102] **Probstein, R.F..** *The dusty gasdynamics of comet heads.* In: Problems of hydrodynamics and continuum mechanics, Ed. M. A. Lavrent'ev, Soc. Industr. Appl. Math.; Philadelphia, 568-583, **1969**.

[103] **Rouleau, F. and P.G. Martin.** *Shape and clustering effects on the optical properties of amorphous carbon.* Astrophys. J., 377, 526-540, **1991**.

[104] **Samarasinha, N.H. and B.E.A. Mueller.** *Spin Axis Direction of Comet 19p/Borrelly Based on Observations from 2000 and 2001.* Earth, Moon, and Planets, 90, 473-482, **2002**.

[105] **Schleicher, D.G., R.L. Millis, and P.V. Birch**. *Narrowband Photometry of Comet P/Halley: Variation with Heliocentric Distance, Season, and Solar Phase Angle.* Icarus, 132, 397-417, **1998**.

[106] **Schleicher, D.G., L.M. Woodney, and R.L. Millis**. *Comet 19P/Borrelly a multiple apparitions: seasonal variations in gas production and dust morphology.* Icarus, 162, 415-442, **2003**.

[107] **Sekanina, Z..** *Fan-shaped coma, orientation of rotation axis, and surface structure of a cometary nucleus. I. Test of a model on four comets.* Icarus, 37, 420-442, **1979**.

[108] **Soderblom, L. A., T.L. Becker, G. Bennett, D.C. Boice, D.T. Britt, R.H. Brown, B.J. Buratti, C. Isbell, B. Giese, T. Hare, M.D. Hicks, E. Howington-Kraus, R.L. Kirk, M. Lee, R.M. Nelson, J. Oberst, T.C. Owen, M.D. Rayman, B.R. Sandel, S.A. Stern, N. Thomas, and R.V. Yelle.** *Observations of Comet 19P/Borrelly by the Miniature Integrated Camera and Spectrometer Aboard Deep Space 1.* Science, 296, 1087-1091, **2002**.

[109] **Soderblom, L. A., D.C. Boice, D.T. Britt, R.H. Brown, B.J. Buratti, R.L. Kirk, M. Lee, R.M. Nelson, J. Oberst, B.R. Sandel, S.A. Stern, N. Thomas, and R.V. Yelle.** *Imaging Borrelly.* Icarus, 167, 4-15, **2004**.

[110] **Stern, S.A., H.A. Weaver, and J.Wm. Parker.** *HST/STIS Observations of Comet 19P/Borrelly during the DS1 encounter.* Astron. J., 126, 444-451, **2003**.

[111] **Stagg, C.R. and M.E. Bailey.** *Stochastic capture of short-period comets.* Royal Astronomical Society, Monthly Notices, 241, 507-541, **1989**.

[112] **Taff, L.G..** *Celestial Mechanics: A Computational Guide for the Practitioner.* Wiley-Interscience. **1985**.

[113] **Thomas, N., D.C. Boice, W.F. Huebner, and H.U. Keller.** *Intensity profiles of dust near extended sources on Comet Halley.* Nature, 332, 51-52, **1988**.

[114] **Thomas N. and H.U. Keller.** *Interpretation of the inner coma observations of comet P/Halley by the Halley Multicolour Camera.* Annales Geophysicae, 8, 147-166, **1990**.

[115] **Thomas, N. and H.U. Keller.** *Comet P/Halley's dust production rate at Giotto encounter derived from Halley Multicolour Camera observations.* Astron. Astrophys., 249, 258-268, **1991**.

[116] **Thomas, N., M.F. A'Hearn, D.C. Boice, D.T. Britt, K.J. Meech, B.R. Sandel, L.A. Soderblom, and R.V. Yelle.** *Jet morphology in the inner coma of Comet 19P/Borrelly observed by the Deep Space One MICAS imaging system.* Amer. Astron. Soc., DPS Meeting ♯33, ♯20.02, **2001**.

[117] **Toon, O.B. and T.P. Ackerman.** *Algorithms for the calculation of scattering by straified spheres.* Appl. Opt., 20, 3657-3660, **1981**.

[118] **Weaver, H. A., S.A. Stern, and J.Wm. Parker.** *Hubble Space Telescope STIS Observations of Comet 19P/Borrelly during the Deep Space 1 Encounter.* Astrophy. J., 125, 444-451, **2003**.

[119] **Weingartner, J.C. and B.T. Draine.** *Dust Grain-Size Distribution and Extinction in the Milky Way, Large Magellanic Cloud, and Small Magellanic Cloud.* Astrophys. J., 548, 296-309, **2001**.

[120] **Whipple, F.L..** *Comets, meteors and the interplanetary complex.* Astron. J., 179, **1949**.

[121] **Whipple, F.L..** *On tests of the icy conglomerate model for comets.* Astron. J., 83, **1950**.

[122] **Whipple, F.L..** *A Comet Model. II. Physical Relations for Comets and Meteors.* Astrophys. J., 113, 464, **1951**.

[123] **Woerkom van, A.J.J..** *On the Origin of Comets.* Bulletin of the Astronomical Institutes of the Netherlands, 10, 445472, **1948**.

[124] **Yeomans D.K..** *Comets, a chronological history of observation, science, myth, and folklore.* Wiley Science Edition, **1991**.

Danksagung

Als erstes möchte ich mich bei Prof. Dr. Nicolas Thomas für die Möglichkeit bedanken, die er mir gegeben, in einem so interessanten Forschungsgebiet zu arbeiten. Meine Arbeit hat viel von seiner wissenschaftlichen Erfahrung und seinen Ratschlägen profitiert.

Als nächstes möchte ich mich bei Herrn Prof. Dr. Klaus Jockers bedanken. Insbesondere dafür, daß er es mir ermöglicht hat, Erdbeobachtungsdaten von Borrelly zu erhalten und die schöne Landschaft Kaukasiens kennenzulernen.

Desweiteren möchte ich mich bei Prof. Dr. Tanyu Bonev für seine Geduld beim Beantworten meiner Emails und seine Hilfe bei den Pik Terskol Daten bedanken.

Dazu danke ich dem DS1 Team, Dr. Dan Boice, Dr. Lawrence A. Soderblom, Dr. Kris Becker etc., für die MICAS Daten und die Informationen.

Auch möchte ich mich bei Prof. Dr. Mike Combi und Valeriy Tenishev für Borrelly's Staubgeschwindigkeiten und die Bereitschaft, sich mit meinen Fragen auseinanderzusetzen, bedanken.

Herzlich bedanken möchte ich mich bei dem technischen Team am Pik Terskol.

Für die wissenschaftlichen Diskussionen und Ratschläge möchte ich mich beim "Planeten"- Team des Max-Planck-Instituts für Sonnensystemforschung, insbesondere Dr. H. U. Keller, Dr. Wojtek Markiewicz und Dr. Bjoern Grieger.

Danke an Bjoern Davidsson für DMILAY, in diesem Fall auch an O.B. Toon and T.P. Ackerman, W. Wiscombe.

Für die fachlichen Hinweise und das Korrekturlesen möchte ich mich bei Herrn Dr. Gehard Schwehm bedanken.

Ein weiteres Dankeschön geht an Prof. Dr. Y. Kitamura für die letzte? Ausgabe seiner Doktorarbeit.

Auch bei bei allen Freunden und Kollegen des MPI für Sonnensystemforschung

und des Physikalischen Instituts der Universität Bern bedanke ich mich für jegliche Hilfe, die mir während der Doktorarbeit zuteil wurde.

An Julia Nikolai einen herzlichen Dank für ihr einfühlsames Zuhören.

I would like to thank Ai Inada a lot, for her precious help in all cases and her kindness to host me including the nearly 7 hour shopping tour (my record!).

For helping me to edit my first paper and calling me for coffee break at 16 o'clock each day ... a big thanks to Nunu Raouafi.

Further I would like to thank Fabrice Portier-Fozzani for the helpful talks and his effort to bring me closer to the French culture.

A special big thanks goes to Ivano Bertini, my shelter when it rains, for all the help, support and care he generously gave to me.

Als letztes bedanke ich mich bei meinen Eltern und Brüdern dafür, daß sie immer für mich da sind und mich in allen Dingen unterstützt haben.

Bern, Dezember 2004.

Curriculum Vitae

Personal Data

Name	Tra Mi Ho
Date of birth	September 10, 1973
Place of birth	Hanoi, Vietnam

Education

1994	Abitur at the Graf-Zeppelin-Gymnasium in Friedrichshafen
1994 - 2000	Physics studies at the Ruprecht-Karls-Universität in Heidelberg
1996	Physics *Vordiplom*
1999 - 2000	Diploma thesis at the Max-Planck-Institut für Kernphysik in Heidelberg in the Group of "Interstellar and Interplanetary Dust"
	Supervisor: Professor E. Grün
	Topic of the thesis: "Measurements of fast and low charged particles with a new high sensitive dust detector"
2000	*Diplom* in Physics
2001	PhD studies in the Planetary Science Group at the Max-Planck-Institut für Aeronomie/Katlenburg-Lindau & Georg-Augustus Universität in Göttingen
	Supervisor: Dr. N. Thomas & Prof. Dr. K. Jockers
2003 - 2004	Completing the PhD thesis at the Physikalisches Institut of the University of Bern, Switzerland.
	Supervisor: Prof. N. Thomas